X-ray Induced Effects and Charge Collection Efficiency in Stabilized Amorphous Selenium Based X-ray Photoconductors

A Thesis

Submitted to the College of Graduate and Postdoctoral Studies

In Partial Fulfillment of the Requirements for the

Degree of Master of Science

In the Department of Electrical and Computer Engineering

University of Saskatchewan

Saskatoon

By

Blaine M. Simonson

Saskatoon, Saskatchewan

Permission to Use

In presenting this thesis/dissertation in partial fulfillment of the requirements for a Postgraduate degree from the University of Saskatchewan, I agree that the Libraries of this University may make it freely available for inspection. I further agree that permission for copying of this thesis/dissertation in any manner, in whole or in part, for scholarly purposes may be granted by the professor or professors who supervised my thesis/dissertation work or, in their absence, by the Head of the Department or the Dean of the College in which my thesis work was done. It is understood that any copying or publication or use of this thesis/dissertation or parts thereof for financial gain shall not be allowed without my written permission. It is also understood that due recognition shall be given to me and to the University of Saskatchewan in any scholarly use which may be made of any material in my thesis/dissertation.

Disclaimer

Reference in this thesis/dissertation to any specific commercial products, process, or service by trade name, trademark, manufacturer, or otherwise, does not constitute or imply its endorsement, recommendation, or favoring by the University of Saskatchewan. The views and opinions of the author expressed herein do not state or reflect those of the University of Saskatchewan, and shall not be used for advertising or product endorsement purposes.

Requests for permission to copy or to make other uses of materials in this thesis/dissertation in whole or part should be addressed to:

Head of the Department of Electrical and Computer Engineering
57 Campus Drive
University of Saskatchewan
Saskatoon, Saskatchewan S7N 5A9 Canada

OR

Dean
College of Graduate and Postdoctoral Studies
University of Saskatchewan
116 Thorvaldson Building, 110 Science Place
Saskatoon, Saskatchewan, S7N 5C9 Canada

Abstract

Stabilized amorphous selenium (a-Se) photoconductive layers are currently used in most modern flat panel digital x-ray image detectors for mammography. The performance of these detectors depends, in part, on the electronic transport properties of the a-Se photoconductive layer. The transport properties consist of the charge carrier drift mobility μ and deep trapping time (lifetime) τ, of both electrons and holes in the photoconductive layer, which determine the x-ray sensitivity of the x-ray image detector through the charge collection efficiency. The product of a carrier's drift mobility, lifetime, and the applied electric field $\mu\tau F$ is the carrier schubweg, which refers to the average distance a charge carrier can travel in the photoconductive layer before it becomes trapped. Trapped carriers are not collected and cause a decrease in the charge collection efficiency and the x-ray sensitivity. The time-of-flight (TOF) and the interrupted-field time-of-flight (IFTOF) experimental techniques are used to measure the transport properties of both holes and electrons in a-Se layers. The TOF transient photoconductivity technique measures the transient photocurrent response of photoinjected charge carriers as they travel through a highly resistive sample under the influence of an electric field. The time width of the TOF pulse is directly related to the drift mobility of the carrier. The IFTOF technique interrupts the drift of the charge carriers through the sample by temporarily removing the electric field, which allows carriers to interact with deep traps in the bulk. The number of free carriers in the bulk decreases over the interruption time. When the electric field is reapplied the remaining free carriers resume drifting through the sample. The ratio of the recovered charge carriers before and after the interruption is related to the charge carrier deep trapping time (lifetime).

The effects of high dose x-ray radiation of a-Se on the transport properties is examined. Stabilized amorphous selenium films, with a nominal composition of a-Se: 0.3% As + 10 ppm Cl, were fabricated through evaporation techniques. X-ray radiation was provided by an Al-filtered tungsten target x-ray tube. The absorbed dose rate was varied from 0.12 Gy/s – 2.5 Gy/s, the x-ray energy was varied from 50 kVp – 90 kVp (corresponding to a mean photon energy from 31.9 keV – 44.7 keV), and the applied electric field was varied from 0 V/μm – 10 V/μm. X-ray irradiation had no effect on the drift mobility of either holes or electrons. In the absence of an applied electric field it was found, for both electrons and holes, that reduction in the electron and

hole lifetimes depended only on the total or accumulated dose D, absorbed in a-Se, and not on the rate of dose delivery or on the x-ray energy over the ranges examined. This allows the reduction in the carrier lifetimes to be simply modeled by $\tau_o/\tau = 1 + AD$, where τ_o is the lifetime before x-ray exposure (equilibrium lifetime), τ is the lifetime after exposure, D is the total absorbed dose, and A is a constant, which is 0.203 (± 0.021) Gy^{-1} for hole lifetime and 0.0620 (± 0.0090) Gy^{-1} for electron lifetime. In the presence of an applied field, the reduction in the hole lifetime due to absorbed dose in a-Se depends on the total energy absorbed as well as the applied electric field during exposure, and not on the x-ray intensity or the x-ray photon energy. The x-ray induced drop in the hole lifetime is modeled with the empirical equation $\tau_{ho}/\tau_h = 1 + B(1 - \exp(-D/C))$, where τ_{ho} is the hole lifetime before x-ray irradiation, τ_h is the hole lifetime after irradiation, D is the total accumulated dose absorbed in the sample (Gy), B is a constant measured to be 4.21, and C is a parameter that depends on the applied field during irradiation, related to the applied field F empirically through a stretched exponential expression of the type $C = C_1\exp[-(F/C_2)^{\beta}] + C_3$ where the constants have been experimentally determined to be $C_1 \approx$ 19.9 Gy, $C_2 \approx 4.44$ V/ μm, $C_3 \approx 0.06$ Gy and $\beta \approx 2.49$. This equation reduces to $\tau_{ho}/\tau_h = 1 + BD/C = 1 + AD$ (where $A = B/C$, and is a constant) for sufficiently low doses, which is a linear approximation of the x-ray induced effects. The latter accurately maps the reduction in the hole lifetime in the case with no applied field. The implications of these findings can be seen through the calculation of the charge collection efficiency. The results show that the effects of x-ray irradiation on a-Se detectors in the absence of an electric field are small, but in the presence of an electric field are considerable. These effects are minimized when the operating field is high (corresponding to a high collection efficiency) and the a-Se is of high quality electronic grade material.

Acknowledgements

I would like to thank my supervisors Professors Safa Kasap and Robert Johanson for their encouragement and leadership in the course of this work. I would also like to thank George Belev, for fabricating the samples used in this work and for help in fixing the experimental system when it was needed. Also I would like to thank my lab-colleagues for many informative discussions. This thesis would not have been possible without the financial support from the University of Saskatchewan and Analogic Canada Corporation. Finally, I must thank my parents, Bradley and Barbara Simonson, and my siblings for their support, encouragement, and advice.

Table of Contents

List of Tables

List of Figures

List of Abbreviations

a-Se	amorphous selenium
a-Si:H	hydrogenated amorphous silicon
AMA	active matrix array
BJT	bipolar junction transistor
CCE	charge collection efficiency
CMOS	complementary metal oxide semiconductor
CMRR	common mode rejection ratio
EHP	electron hole pair
ESR	electron spin resonance
GPIB	general purpose instrumentation bus
GUI	graphical user interface
HEXFET	hexagonal shaped MOSFET
HV	high voltage
IFTOF	interrupted field time of flight
ITO	indium tin oxide
IVAP	intimate valance alteration pair
MOSFET	metal oxide field effect transistor
PC	personal computer
PCI	peripheral component interconnect
PPM	parts per million
SNR	signal to noise ratio
TFT	thin film transistor
TOF	time of flight
VAP	valence alteration pair

1. Introduction

1.1 Introduction

Radiography, the process of measuring ionizing radiation that has passed through an object to build a picture of the internal form of that object, is an important diagnostic tool for medical treatments. X-rays have become the most prevalent form of radiation used in medical diagnostics. Previously the most common form of radiography relied on film emulsion to store the optical response generated from x-ray photons interacting with a phosphor screen. This system was quite ineffective as the film and screen had to be removed for processing and then replaced for each successive image. This process has evolved into modern digital radiography techniques which have inherent advantages over the film/screen systems. The images generated using digital radiographic techniques are fully digital and as such can be easily stored and shared electronically without the risk of losing the images. Also, these techniques allow a higher patient throughput, increased efficiency, and a greater dynamic range which lower the necessary x-ray exposure to the patients [1]. Further, through the use of computer software, the image quality can be improved and computer-aided diagnosis can be used [2].

Digital radiography has been advanced using direct conversion flat-panel x-ray image detectors which are currently widely used in medical applications such as mammography, chest radiology, angiography, fluoroscopy, and computed tomography [3]. These detectors consist of an x-ray sensitive photoconductive layer coated onto a large array of pixels as part of an active-matrix-array (AMA). The x-ray photoconductor is used as the principal detecting element by converting x-ray photons into collectable electronic charge. The AMA collects this charge with storage capacitors in each pixel, and the charge can be readout through a thin-film-transistor (TFT) in each pixel. Stabilized amorphous selenium (a-Se) is currently the most commonly used photoconductive layer [1]. Other photoconductors have been investigated but suffer from either possessing high dark currents, low charge collection efficiencies, or technological problems in manufacturing a large uniform and homogenous layer [3]. Continued research into a-Se and its alloys is necessary in order to increase the overall performance of x-ray detectors.

Figure 1.1: An example of an amorphous selenium based flat-panel x-ray imager for mammography by Analogic Canada (AXS-2430) [3].

Two important properties of stabilized amorphous selenium photoconductive layers are the charge-carrier drift mobility and charge-carrier trapping time. These transport properties directly influence the x-ray detector performance through the charge collection efficiency and the x-ray sensitivity. To measure these properties the Time-of-Flight (TOF) and Interrupted-Field Time-of-Flight (IFTOF) transient photoconductivity techniques are used on stabilized a-Se layers. The TOF technique measures the transient response of photoinjected charge-carriers as they drift across a biased photoconductor. The pulse width of the generated response provides the transit time of the charge-carriers which is directly related to the charge-carrier drift mobility μ. In the IFTOF technique, the bias is temporarily removed from the photoconductor, and the fractional change in the magnitude of the transient response is related to the charge-carrier deep trapping time (lifetime) τ. The product of the charge-carrier drift mobility and lifetime determines the charge collection efficiency and the x-ray sensitivity of the x-ray detector [4].

The TOF and IFTOF experiments are used in this work to find the charge-carrier transport properties (drift mobility and lifetime) in various samples of stabilized a-Se. In addition, since a-Se is used as the photoconductive layer in x-ray detectors, the effect of x-ray irradiation on the transport properties is examined.

1.2 X-ray Imaging

Digital radiography is the process in which x-ray radiation is passed through an object and is measured and converted into a digital image in order to view the internal form of the

object. The attenuation of an x-ray photon through an object depends on the photon energy of the x-ray, the density of the material, and the thickness of the material [5]. Thus, the x-ray radiation that has passed through the object will have a spatial distribution in intensity that depends on the internal structure of the object. For example, when x-rays pass through a human, the bone tissue will absorb more x-ray radiation than the surrounding soft tissues, such as fat and muscle. The attenuated radiation is converted into an image, or radiograph, with an x-ray detector by converting the x-ray radiation into electrical charge, where the produced charge is proportional to the intensity of the x-ray radiation. The electrical charge is then converted into an image, where areas with low charge, corresponding to low x-ray intensity and thick or dense material (e.g. bone tissue), show up white on the image, and areas with a lot of charge show up dark.

Figure 1.2 shows a typical x-ray imaging system which consists of an x-ray tube, a collimator, the object to be examined, and an x-ray detector. The x-ray tube produces a spectrum of x-ray radiation through the collision of high energy electrons and a tungsten target. The x-ray radiation is passed through the collimator, which contains 2 or 3 perforated lead sheets, in order to produce a beam of partially parallel x-rays with uniform intensity. The x-ray radiation then passes through the object, creating a spatial distribution in intensity, and is captured by the x-ray detector.

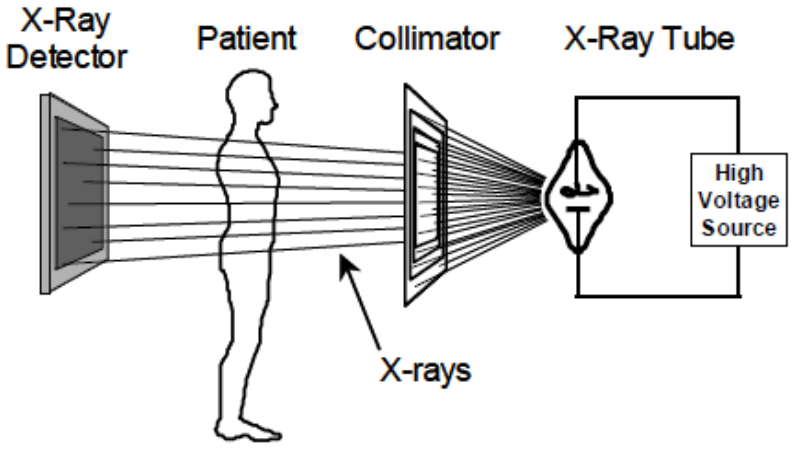

Figure 1.2: A typical projection radiography system. X-rays are passed in a collimated beam through an object, and recorded by the detector.

The requirements on the x-ray detector depend on the object being measured and what needs to appear in the image. The x-ray detector should always be slightly larger than the object

being measured as there is no practical method of focusing x-rays. In chest radiography, when the measured object creates large differences of intensity in the x-ray beam, from the difference in attenuation of bone and soft tissue, the detector must have a large dynamic range. In mammography however, the measured object creates small differences of intensity, from normal and cancerous cells, and the detector has far more stringent requirements such as high-resolution images [6].

1.2.1 Direct Conversion X-ray Detectors

In order for the x-ray detector to generate a digital image, the x-ray radiation must be converted into electrical charge, which must in turn be collected and digitized. The variation in intensity over the area of the detector provides the image information, and the digitized signal must be mapped to the physical location of its position on the detector. There have been two methods used to convert the x-ray radiation into electrical charge: indirect conversion and direct conversion.

Indirect conversion detectors generate the electrical charge by coupling a phosphor screen to a photodetector. The phosphor screen absorbs the x-rays and converts them into visible light, which is collected by a photosensitive element that generates an electrical charge. The electrical charge is proportional to the light emitted from the phosphor screen which is in turn proportional to the incident x-ray radiation [7]. Direct conversion detectors generate the electrical charge by using an x-ray sensitive photoconductive material to absorb the x-ray radiation. The material is placed under a bias potential, facilitated through metal electrodes on each side. Incoming x-ray photons produce electron-hole pairs through the photoelectric effect. Under the influence of the electric field the electrons and holes will separate and drift to the electrodes. The accumulated charge, which is proportional to the incident x-ray radiation, on the electrodes can then be measured electronically. [7]

There are several distinct advantages of direct conversion detectors over indirect conversion detectors. First is that direct conversion detectors have a higher inherent resolution due to the electric field across the detector being perpendicular to the imaging plane. The x-ray generated charge-carriers drift along the electric field lines and the lateral spread of the x-ray image is minimal. Thus the spatial charge image that is collected will be the same as the spatial radiation image that impinges on the detector. On the other hand, indirect conversion detectors

use a phosphorous layer to absorb the x-rays, which cause scatter of optical photons by the phosphor grains, lowering the resolution of the collected image [6]. A second advantage is the sensitivity of a direct conversion detector can be maximized with proper choice of the photoconductor material, the operating bias, and the thickness of the material [8]. Indirect conversion detectors, however, are limited by the x-ray sensitivity of the phosphor screen.

1.2.2 a-Se Based X-ray Detectors

Direct conversion digital flat-panel x-ray image detectors using a-Se as the photoconductive layer are currently widely used in digital radiography [3]. This technology is based on the amorphous silicon (a-Si:H) active-matrix-array (AMA) device used in large area display applications [3, 4]. In an AMA circuit, the imaging plane is divided up into a $M \times N$ array of discrete picture-producing elements or pixels, where M and N are the number of elements in each direction. Each pixel contains a charge collection capacitor and a thin-film-transistor (TFT) switch. The direct conversion digital flat-panel x-ray image detector is then fabricated by coating a thick layer (~ 1 mm) of a-Se on the surface of the AMA. Then, a metal top electrode is evaporated onto the a-Se layer to facilitate the application of a biasing voltage. A cross sectional view of the pixel elements is shown in Figure 1.3.

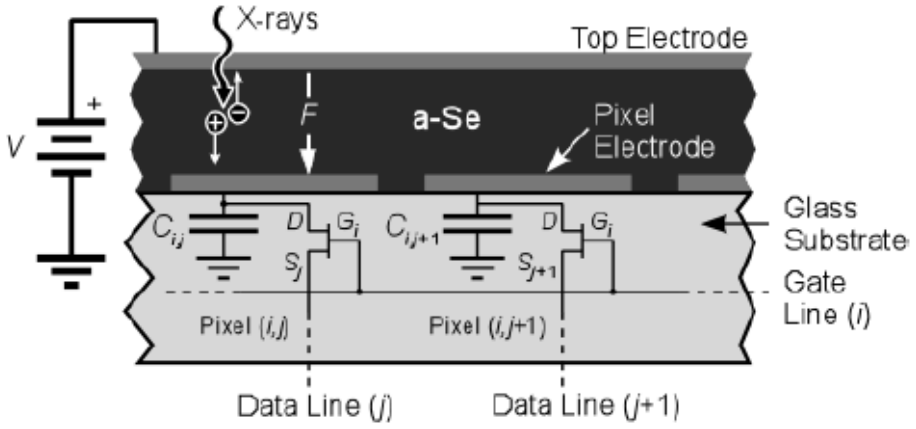

Figure 1.3: A cross-sectional view of an a-Se based flat-panel direct-conversion digital x-ray image detector. The image also shows some of the electronics connected to the individual pixels.

When an x-ray photon is incident on the a-Se photoconductive layer it generates electron-hole pairs (EHPs) through the photoelectric effect. The number of EHPs generated is directly proportional to the amount of exposure incident on the layer. The biasing voltage creates an

internal field F which separates the EHPs, drifting the electrons to the top contact to be collected by the voltage source and drifting the holes to the bottom electrode to be collected and stored in the pixel capacitor C_{ij}. The accumulated positive charge stored on the pixel capacitor Δq_{ij} is determined by the number of holes collected and is thus directly proportional to the exposure incident over the pixel area.

After x-ray exposure the pixel capacitors contain a spatial charge signal that represents the x-ray image that is incident on the photoconductive layer. The readout of the image involves coordinating the operation of the TFT switches in the AMA. A small section of an $M \times N$ flat panel AMA is shown in Figure 1.4. The gate terminals of each TFT in row i are connected to the control line i. Activation of control line i turns on each of the TFTs in the row and the charge signal on a pixel capacitor in column j can be readout through the data line j, which is connected to the source terminals on each of the TFTs in column j. The drain terminal of each TFT is connected to its corresponding pixel capacitor. This creates a parallel data stream corresponding to row i which is digitized, multiplexed, and transmitted to the computer. The charge readout process then proceeds to the next row and continues until all of the array rows have been readout.

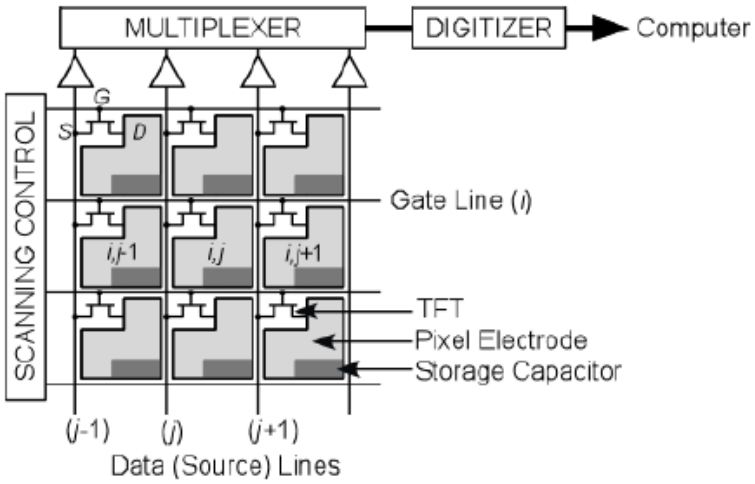

Figure 1.4: A small section of a thin-film-transistor active-matrix-array used in flat panel x-ray image detectors with self-scanning readout.

The direct conversion digital flat-panel x-ray image detector using an a-Se photoconductive layer on an AMA is a self-scanning and compact detector which is suitable for general radiographic imaging. A typical x-ray image taken using an a-Se flat-panel x-ray image

detector is shown in Figure 1.5. These flat-panel x-ray image detectors do not require complicated external scanning schemes nor any handling or adjustment as the image is readout with the internal electronics. This allows the flat-panel x-ray image detectors to be used in real time imaging applications such as fluoroscopy. The resolution of the x-ray image in the detectors is determined by the pixel size in the AMA. [9] Larger pixels result in a lower resolution so there has been a lot of research into smaller pixel AMA's [10, 11, 12].

Figure 1.5: A typical x-ray image obtained using the direct-conversion flat-panel x-ray image detector using a stabilized a-Se photoconductive layer [4].

1.3 X-ray Detector Performance

The performance of a direct conversion flat-panel x-ray image detector is determined by the quality of the semiconductor material used as the photoconductive layer. The x-ray sensitivity of the detector is determined by the amount of charge that can be collected per unit incident radiation on the detector. X-ray sensitivity of an x-ray detector depends on three properties of the photoconductive material: the linear attenuation coefficient, the electron-hole pair creation energy, and the charge transport properties of the material. This section will describe these properties as well as describe an ideal x-ray photoconductive material.

1.3.1 X-ray Linear Attenuation Coefficient

The linear attenuation coefficient α of a material determines the number of photons that are attenuated in that material. The attenuation involves both absorption and scattering. The fraction of incident x-ray photons that are attenuated by a photoconductor is given by:

$$A_Q(E) = [1 - \exp(-\alpha L)] \tag{1.1}$$

where L is the sample thickness and $\alpha = \alpha(E, Z, d)$ is the linear attenuation coefficient of the photoconductor material that depends on the incident photon energy E, the atomic number of the photoconductor material Z, and the density of the photoconductor material d. The attenuation coefficient typically decreases with increasing x-ray photon energy and increases with an increasing atomic number. In a-Se, the attenuation coefficient, above the K-edge, empirically follows $\alpha = (6.67 \times 10^5)E^{-2.7055}$ where E is in keV and 12.7 keV ≤ E ≤ 100 keV [13].

By insuring that most of the incident radiation on the photoconductive layer is attenuated by the layer, the amount of radiation passed through the patient can be minimized. To do this the thickness of the photoconductive layer should be made to be more than the attenuation depth δ. That is $\delta = 1/\alpha < L$. The attenuation depth refers to the thickness of material needed to absorb 63% of the incident x-ray radiation. As different applications use different mean energies of x-ray radiation, they will require differing thickness of the photoconductive layer. For example, in mammography, the mean x-ray photon energy is 20 keV. If we assume the minimum photoconductor thickness must be 2δ, then an a-Se film of at least 100 μm would be required. In practice, typically, 200 μm is used to ensure that high energy photons up to 30 keV are also attenuated. In the case of chest radiography the mean x-ray photon energy is 60 keV and the same thickness requirement leads to 2000 μm of a-Se to attenuate the incident x-ray radiation [13].

As a thicker photoconductive layer will collect more of the incident x-ray radiation, the ideal x-ray detector would utilize as thick of a layer as possible. The maximum thickness of the photoconductive layer, however, is limited by three factors. First, it is difficult and expensive to fabricate thick photoconductive layers onto the AMA while maintaining uniformity in their properties and remaining defect free [13]. Secondly, the probability that the x-ray generated charge will be lost due to trapping before it reaches the electrode increases as the thickness of the

photoconductive layer increases. This effect is called collection-limited sensitivity in which the carrier schubweg is shorter than the sample thickness. The schubweg is a measure of how far average charge-carriers will travel in a photoconductor before being trapped [6], that is $\mu\tau F$ where μ is the drift mobility, τ is the lifetime, and F is the applied field. The third limit on maximizing the thickness of the material is that the biasing voltage used to maintain an operating field must increase as the photoconductive layer thickness increases. A typical operating field of 10 V/μm would require a bias voltage of 10 kV on a photoconductive layer 1 mm thick. This high of bias voltages cause technical problems, such as dielectric breakdown in the panel, protecting the TFT switches in the AMA, and supplying the voltage itself. Further, higher bias voltages will increase the dark current, that is, the current that appears without x-ray exposure, which decreases the signal to noise ratio of the detector.

1.3.2 Electron-Hole Pair Creation Energy

When an x-ray photon is absorbed by the photoconductive layer, it generates a highly energetic photoelectron through the photoelectric effect. This photoelectron has enough energy to generate other electron-hole pairs through collisions with other atoms. As such it is possible for many electron-hole pairs to be generated by the absorption of one x-ray photon. The amount of generated charge ΔQ from the absorption of x-ray radiation energy ΔE is given by:

$$\Delta Q = \frac{e\Delta E}{W_{\pm}} \tag{1.2}$$

where $W_{\pm}$ is the electron-hole pair creation energy, also known as the ionization energy. The electron-hole pair creation energy for a material is the amount of radiation energy that must be absorbed to generate a single electron-hole pair. In order to maximize the sensitivity of the detector, this value should be as low as possible, maximizing the number of generated electron hole pairs.

In amorphous semiconductors it has been shown that the electron-hole pair creation energy is given by $2.2E_g + E_{\text{phonon}}$ where E_g is the bandgap of the material and the phonon energy term E_{phonon} represents the energy of the phonons involved with the ionization process and is expected to be small [14]. In a-Se, however, the electron-hole pair creation energy has a dependence on the applied electric field, decreasing as the electric field increases. This relationship at room temperature can be approximated by [8]:

$$W_{\pm} \approx W_{\pm}^{o} + \frac{B}{F} \tag{1.3}$$

where $W_{\pm}^{o}$ is the saturated electron-hole pair creation energy (at infinite applied field), B is a constant that depends on the x-ray photon energy, and F is the applied electric field across the photoconductor.

1.3.3 Charge Transport and Schubweg Limited Sensitivity

When a charge-carrier is generated in a photoconductive layer by an incident x-ray photon, it drifts under the influence of the applied electric field F with a velocity that is determined by the charge-carrier drift mobility μ and the magnitude of the applied electric field F. In order to fully contribute to the charge image, the charge-carrier must be collected by the pixel capacitor that corresponds to its point of generation. However, in a-Se photoconductive layers there is a significant concentration of electron and hole traps in the bulk of the sample. These traps are able to remove a charge-carrier from the conduction band of the material. This prevents the charge-carriers from drifting and thus prevents them from being collected, which in turn decreases the charge collection efficiency and thus the sensitivity of the detector. The probability that a charge-carrier gets trapped per unit time is determined by the reciprocal of the charge-carrier trapping time (lifetime) τ. In other words, the lifetime is the average amount of time a charge-carrier can exist in the conduction band of the photoconductor before being trapped.

The product of the drift mobility, lifetime, and applied electric field is called the charge-carrier schubweg $\mu\tau F$, which is a measure of the average distance a charge-carrier will travel in a photoconductor before becoming trapped. In an ideal x-ray detector, the photoconductive layer would be selected so that the layer thickness L is less than both the electron and hole schubwegs (i.e. $L < \mu\tau F$). This conflicts with the desire for a thick photoconductive layer when considering the absorption of the x-ray photons. Thus, the thickness of the photoconductive layer must be selected carefully with $\delta < L < \mu\tau F$. Note that this is easily solved by having a thick photoconductor layer and a high operating bias voltage, but it leads to the high-voltage problems discussed earlier.

1.3.4 Charge Collection Efficiency

The x-ray sensitivity of an x-ray detector is determined by the charge released and collected per unit area per unit exposure of radiation. The calculation of the x-ray sensitivity is very difficult, requiring the solution of the set of continuity, rate, and Poisson equations as well as the rate of defect generation [15, 16]. The charge collection efficiency (CCE) of the photoconductor is defined as the ratio of collected charge to generated charge and is calculated much easier. The calculation of the CCE can be performed using the continuity equation neglecting diffusion and taking the electric field, the charge-carrier mobilities, and the charge-carrier lifetimes as uniform [17]. It may also be derived by examining the propagation of the injected exponential distribution of hole and electron concentration profiles and using the Ramo theorem and the Hecht collection efficiency [8]. As the x-ray sensitivity of a detector is heavily determined by the CCE, calculation of the CCE is an effective tool. The following calculation of the CCE follows that described in Reference [8].

Consider a monoenergetic beam of x-ray radiation incident on an x-ray detector. The radiation passing through the photoconductive layer decreases exponentially as:

$$E'(x) = E[1 - \exp(-\alpha x)] \tag{1.4}$$

where E is the x-ray energy at $x = 0$ and α is the x-ray attenuation coefficient. If the energy absorbed in a small distance δx is δE, then the magnitude of charge of either polarity generated in δx is:

$$\delta q = \frac{e\delta E'}{W_{\pm}} \tag{1.5}$$

where $W_{\pm}$ is the electron-hole pair creation energy, and e is the elementary charge. The amount of energy absorbed in the small distance δx is given by:

$$\delta E' = \alpha_{en} E \exp(-\alpha x)\delta x \tag{1.6}$$

where α_{en} is the energy absorption coefficient. Integration over x gives the total generated or injected charge:

$$Q_i = \frac{eE}{W_{\pm}} \frac{\alpha_{en}}{\alpha} (1 - \exp(-\alpha L)) \tag{1.7}$$

where L is the thickness of the photoconductive layer.

Assuming a positive bias at the top electrode of the x-ray detector, a hole generated at x must travel a distance $L - x$. Drift of the hole through the photoconductor generates a photocurrent, which is determined using the Shockley-Ramo theorem (see Chapter 2), and integration of the photocurrent over time gives the charge collected from the hole:

$$q_h(x) = e\frac{L-x}{L} \tag{1.8}$$

Similarly, integration of a single electron's photocurrent over time gives the charge collected from the electron:

$$q_e(x) = e\frac{x}{L} \tag{1.9}$$

and the total charge collected from a single injected electron-hole pair is $q_h(x) + q_e(x) = e$. According to the Hecht relation [18], the charge collection efficiency η for a given carrier generated a distance l from the collection point in the presence of traps is:

$$\eta = \frac{\mu\tau F}{l}\left[1 - \exp\left(-\frac{l}{\mu\tau F}\right)\right] \tag{1.10}$$

where μ is the charge-carrier drift mobility, τ is the charge-carrier lifetime, and F is the applied field. This equation has three assumptions: first that the sample is under small signal conditions, explained in Chapter 2, second that the charge-carrier drift mobility and lifetime are uniform across the device, and third that the trap filling effects are negligible. Applying Equation 1.10 to electrons and holes generated at x results in the collected charge from charge generated at x as:

$$\delta q(x) = \frac{e\delta E'}{W_{\pm}}\frac{\mu_h\tau_h F}{L}\left[1 - \exp\left(-\frac{L-x}{\mu_h\tau_h F}\right)\right] + \frac{e\delta E'}{W_{\pm}}\frac{\mu_e\tau_e F}{L}\left[1 - \exp\left(-\frac{x}{\mu\tau F}\right)\right] \tag{1.11}$$

Substituting in Equation 1.6 and integrating over x results in the total collected charge:

$$Q = \frac{eE}{W_{\pm}}\frac{\alpha_{en}}{\alpha}\frac{\mu_h\tau_h F}{L}\left[(1 - e^{-\alpha L}) + \frac{\left(e^{-\frac{L}{\mu_h\tau_h F}} - e^{-\alpha L}\right)}{\left(\frac{1}{\alpha\mu_h\tau_h F}\right) - 1}\right] + \frac{eE}{W_{\pm}}\frac{\alpha_{en}}{\alpha}\frac{\mu_e\tau_e F}{L}\left[(1 - e^{-\alpha L}) - \frac{\left(e^{-\alpha L - \frac{L}{\mu_e\tau_e F}}\right)}{\left(\frac{1}{\alpha\mu_e\tau_e F}\right) + 1}\right] \tag{1.12}$$

Dividing by the total generated charge gives the charge collection efficiency:

$$\eta_c = \frac{\mu_h \tau_{ho} F}{L}\left(1 - \frac{\left[\exp\left(-\frac{L}{\mu_h \tau_{ho} F}\right) - \exp\left(-\frac{L}{\delta}\right)\right]}{\left[1-\exp\left(-\frac{L}{\delta}\right)\right]\left[1-\frac{\delta}{\mu_h \tau_{ho} F}\right]}\right) + \frac{\mu_e \tau_{eo} F}{L}\left(1 - \frac{\left[1-\exp\left(-\frac{L}{\delta}-\frac{L}{\mu_e \tau_{eo} F}\right)\right]}{\left[1-\exp\left(-\frac{L}{\delta}\right)\right]\left[1+\frac{\delta}{\mu_e \tau_{eo} F}\right]}\right) \quad (1.13)$$

1.3.5 The Ideal Photoconductor

The performance of any direct conversion x-ray detector depends on the proper selection of the photoconductive material. The ideal photoconductive layer can be described to have the following properties [4]:

1. High x-ray absorption. The high x-ray absorption of a material will ensure that most of the incident x-ray radiation will be absorbed by the layer. Any x-ray radiation not absorbed by the layer is not detected and is thus wasted. Higher x-ray absorption allows the x-ray radiation passed through a patient to be minimized.
2. High x-ray sensitivity. The photoconductive layer should be able to generate and collect as many electron hole pairs as possible per unit of incident radiation. This requires a low electron-hole pair creation energy ($W_{\pm}$), high x-ray absorption, and good carrier transport properties. Lower electron-hole pair creation energies cause each incident x-ray photon to generate greater amounts of charge. Good carrier transport properties result in a high charge collection efficiency.
3. Low dark current. Lower dark currents will maximize the signal-to-noise ratio of the detector. In order to lower the SNR, non-injecting contacts are used with materials with large bandgaps (E_g). Note that increasing the bandgap, while lowering the dark current, will also increase the electron-hole pair creation energy.
4. No recombination of electron-hole pairs in the bulk of the photoconductive layer should occur. Electron-hole pairs that recombine cannot be collected, resulting in a lowered sensitivity of the photoconductive layer. The rate of recombination is directly proportional to the concentration of charge-carriers and can be minimized by lowering the x-ray exposure.
5. Negligible deep trapping of charge carriers. Deep trapped carriers also cannot be collected and therefore lower the sensitivity of the photoconductor. The charge-carrier schubwegs should be much greater than the thickness of the photoconductive layer $\mu\tau F \gg L$.

6. The longest charge-carrier transit time must be shorter than the access time for the pixel. This will ensure that all of the charge-carriers are collected before any pixel is readout.
7. The properties of the photoconductor should not deteriorate with time or repeated x-ray exposure.
8. The photoconductive layer should be able to be coated on the large area AMA without damaging any of the electronics. For example, if the photoconductor must be annealed at temperatures above 300°C it can damage the a-Si:H TFTs in the AMA. Large area detectors are necessary as there is no practical way to focus x-ray radiation.

Amorphous selenium alloys are a good selection for the x-ray photoconductive layers on direct-conversion large-area flat-panel x-ray image detectors. a-Se photoconductive layers have acceptable x-ray absorption, good electron and hole transport properties, and a low dark current. Furthermore, a-Se can be easily coated on the AMA panel using conventional vacuum deposition techniques. The substrate temperature during evaporation is kept at ~ 60 - 70°C, well within the threshold stated earlier. As a result, a-Se alloys in flat-panel x-ray image detectors are well suited for applications such as radiography and mammography and the electronic and physical properties of a-Se have been studied extensively and reported in the literature.

1.4 Research Objectives

This research focuses on the effects of x-ray radiation on the charge-carrier transport properties of a-Se layers in the absence and presence of an applied electric field. The charge-carrier drift mobility μ and the charge-carrier lifetime τ are important properties of the photoconductive layer. The product of these two properties determines the charge-carrier schubweg of the material, which in turn determines the charge collection efficiency and hence the x-ray sensitivity of the x-ray detector. The charge-carrier transport properties must be measured in an accurate manner in order to ensure the validity of the results.

The charge-carrier transport properties of a-Se samples will be measured using the Time-of-Flight (TOF) and the Interrupted-Field Time-of-Flight (IFTOF) transient photoconductivity techniques. The TOF experiment is used to measure the drift mobility of charge-carriers by measuring the transient current generated by the drift of photoinjected carriers through a sample. A short pulse of light is used to generate a thin sheet of charge-carriers which drifts across the sample under the influence of an electric field, inducing an external photocurrent that can be

easily measured. The transit time of the charge-carriers can be measured from the photocurrent signal and is used to calculate the drift mobility. The IFTOF experiment is used to measure the deep trapping time (lifetime) of charge-carriers by interrupting the drift of the charge-carriers. This is done by removing the electric field for a short duration, allowing charge-carriers to interact with the deep traps in the sample, and comparing the magnitude of the photocurrent before and after the interruption. By examining the ratio of the recovered photocurrent against the interruption time, the charge-carrier lifetime can be determined. In order to measure the transport properties of the a-Se samples, an experimental apparatus that is capable of performing both the TOF and IFTOF measurements is needed. The system that will be used for this work was originally designed by R. E. Johanson in this department.

Previous work has shown that x-ray irradiation creates defects in amorphous selenium samples which causes a reduction in the charge-carrier lifetimes. The dependence of this reduction in the charge-carrier lifetimes on the dose rate as well as the sample temperature have been examined. The x-ray induced effects had no dependence on the absorbed dose rate, but the effects were found to have a large dependence on the temperature [19, 20, 21]. This research will examine the dependence of the x-ray induced effects on the transport properties of a-Se samples on the x-ray photon energy, as well as the applied electric field during exposure. These dependences are important because different applications of x-ray imaging use different x-ray photon energies, for example in chest radiography the average photon energy is 60 keV and in mammography the average photon energy is 20 keV. Also, when an x-ray detector is exposed to x-ray radiation it is placed under an applied field, and the x-ray induced effects under an applied field should be examined.

1.5 Thesis Outline

This chapter has provided an introduction to digital radiography as well as its use of a-Se based direct-conversion flat-panel x-ray image detectors. These large-area detectors are fabricated using an x-ray sensitive photoconductive layer, such as stabilized amorphous selenium, coated onto an active-matrix-array (AMA). Incident x-ray radiation is converted to electrical charge by the photoconductor, which is collected by the pixel electrodes in the AMA and is readout using thin film transistors in the AMA. These detectors are compact, self-scanning, and produce high quality digital x-ray images. a-Se is currently the best

photoconductive material in use due to its good x-ray absorption, small dark currents, good charge-carrier transport properties, and its ability to be coated onto large-area AMAs safely.

The second chapter outlines the principles of the Time-of-Flight (TOF) and the Interrupted-Field Time-of-Flight (IFTOF) transient photoconductive techniques. Also, the derivations of the expressions for the TOF transient photocurrent under several trapping conditions are presented. Chapter 3 describes the experimental apparatus used to capture the TOF and IFTOF photocurrent signals in detail, as well as the process used to fabricate quality electronic grade stabilized a-Se samples. In Chapter 4, the results and discussion from the measurements of the x-ray induced effects on the transport properties in a-Se samples in the absence of an applied field is presented. In Chapter 5, the results and discussion from the measurements of the x-ray induced effects on the transport properties in a-Se samples in the presence of an applied field is presented. The conclusions from the experimental results are presented in Chapter 6 along with suggestions for future work.

2. Principles of Time-of-Flight Transient Photoconductivity

2.1 Introduction

As explained in Chapter 1, amorphous semiconductors, in particular amorphous selenium, are widely used as the photoconductive layer in flat panel x-ray image detectors. The performance of the detectors is heavily dependent on the charge-carrier transport properties of the photoconductive layer. Due to the disordered nature of amorphous materials, theoretical determination of these properties is extremely difficult and characterization of these properties rely on experimental research. The time-of-flight (TOF) and interrupted-field time-of-flight (IFTOF) transient photoconductivity experiments provide a means to directly measure the charge-carrier drift mobility and lifetime in highly resistive materials. These experiments measure the transient current response from the photoinjection and drift of free charge-carriers through a sample. This chapter will present the principles of the TOF and IFTOF transient photoconductivity techniques, as well as the theory needed to properly interpret the photocurrent signals over different types of transport and trapping conditions.

2.2 Time-of-Flight Transient Photoconductivity Technique

The Time-of-Flight (TOF) transient photoconductivity technique measures the transient response of photoinjected charge-carriers drifting across a highly resistive material. A simplified schematic of the TOF technique is shown in Figure 2.1. A highly resistive sample of thickness L is prepared and sandwiched between two non-injecting metal electrodes (A and B). The top electrode (A) is semi-transparent to allow light to pass through and is positively charged (in this example) by the voltage V_o. The bottom electrode (B) is grounded through a sampling resistor R. The sampling resistor R is sufficiently small so that the RC time constant (where C is the sample capacitance) is much smaller than the time domain of the transient photocurrent. If the RC time constant is much larger than the time domain of the photocurrent, the photocurrent becomes integrated.

Electron-hole pairs (EHPs) are generated at the surface of the sample by a pulse of strongly absorbed light through photogeneration. In the example of Figure 2.1, electrons will be immediately collected by the positively charged top contact (A) and holes form a thin charge sheet that will drift across the sample (from A to B) under the influence of the applied electric

field. This induces an external photocurrent $i_{ph}(t)$ through the sampling resistor which can be easily measured. To measure the transient response of electrons through the sample, the polarity of the voltage source is simply reversed.

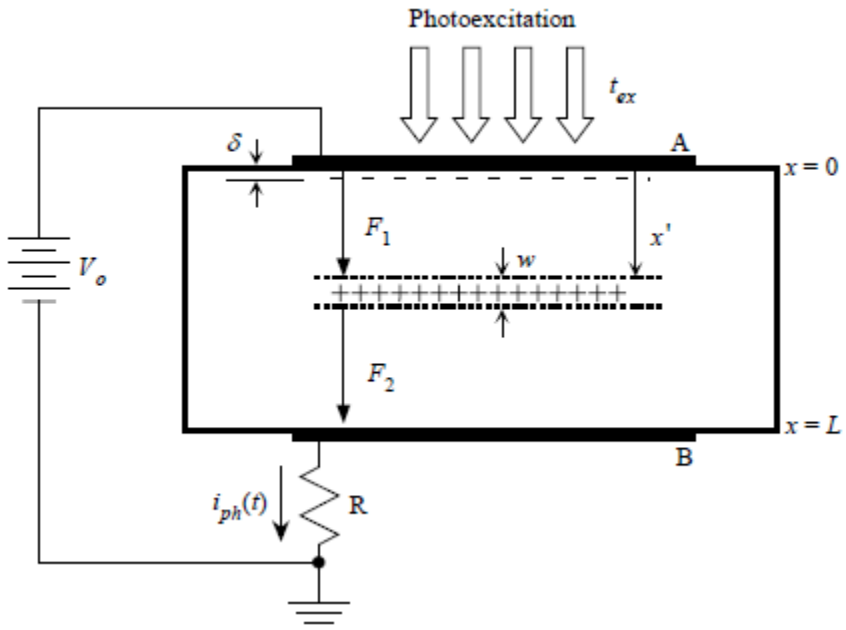

Figure 2.1: Simplified schematic of the TOF measurement technique.

Several limitations are placed on the light source used for photoexcitation. The light source must be chosen with a wavelength such that the absorption depth of the light (δ) is much less than the sample thickness L. This results in the photogenerated electrons to be immediately collected by the top contact and therefore not interfere with the experiment. This also ensures the photogenerated holes will effectively drift across the entire length of the sample. If the absorption depth is too small however, the photogenerated holes will be captured by surface defects in the sample. The light source must also provide a pulse of light that is much shorter than the time it takes for the holes to drift across the sample. This ensures that the injected holes travel through the sample in a narrow sheet of charge with a width w that is much less than the sample thickness L. Finally, the intensity of the light pulse must be sufficiently low to prevent the charge sheet from perturbing the internal electric field in the sample. This ensures the experiment is performed under small signal conditions, which helps simplify the analysis of the experiment results and is further explained below.

As the narrow sheet of charge drifts through the sample it induces an external photocurrent as stated above. By considering the effect the charge sheet has on the internal electric field in the sample the photocurrent can be understood. When the charge sheet is at position x' as in Figure 2.1, the electric fields above and below the charge sheet are constant [22].

$$F_1 = F_o + \frac{ep_o w}{\varepsilon}\left(\frac{x\prime}{L} - 1\right) \tag{2.1}$$

and

$$F_2 = F_o + \frac{ep_o w}{\varepsilon}\frac{x\prime}{L} \tag{2.2}$$

where F_o is the applied (or nominal) electric field ($F_o = V_o/L$), p_o is the concentration of holes in the charge sheet, ε is the dielectric permittivity of the material, w is the width of the injected charge sheet, and L is the sample thickness. These equations indicate that the applied electric field is perturbed by the presence of the sheet of charge. The electric field behind the charge sheet is reduced and the electric field in front of the charge sheet is increased. This change in the electric field with carrier drift induces the external photocurrent to flow through the sampling resistor.

In order to determine the drift mobility of the charge sheet from the TOF experiment, it is important that the internal electric field be constant across the sample. Thus, the perturbation term in Equations 2.1 and 2.2 must be negligible compared to the applied electric field. In order to achieve this, the small signal conditions mentioned earlier must be satisfied. This condition is realized when the total injected charge in the charge sheet Q_o is much less than the charge on the electrodes $C_S V_o$, where C_S is the sample capacitance. Under the small signal condition, the internal field can be approximated as constant and the drift velocity of the charge sheet will be constant as a result [23]. If the small signal condition is not met, then the analysis must include the effects of space charge perturbation and it becomes much more complex [24].

The magnitude of the external photocurrent produced due to the drift of the charge sheet can be determined using Ramo's theorem [25]. Consider the schematic in Figure 2.2. A positive charge q is at a position l in a sample of highly resistive material drifting at a constant velocity v_d under the influence of the applied electric field F_o. The velocity of the charge in relation to the applied field is $v_d = \mu F_o$ where μ is the drift mobility of the carrier in the material. The

charge will drift across the sample, inducing a current in the external circuit, until it reaches the electrode and is collected by the battery. The time it takes for the charge to drift across the sample is defined as the transit time $t_T = l/v_d$.

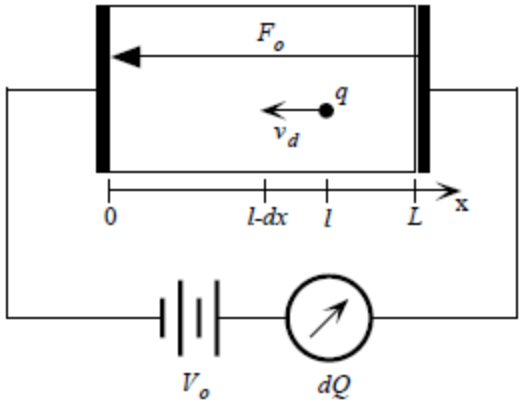

Figure 2.2: The motion of a charge, *q*, through a distance *dx* in a sample induces a charge *dQ* to flow in the external circuit.

In order to determine the magnitude of the induced current in the external circuit, the work done on the charge must be considered. Moving the charge a distance of dx requires an amount of work $dW = qF_o dx$. This work is performed by the external battery. The work done by the battery moving the charge a distance of dx in the time dt is $dW = qF_o dx = V_o i_{ph}(t)dt$. Since $F_o = V_o/L$ and $v_d = dx/dt$ it can be shown the magnitude of the induced external current is:

$$i_{ph}(t) = \begin{cases} \frac{qv_d(t)}{L} & 0 < t < t_T \\ 0 & t > t_T \end{cases} \tag{2.3}$$

If the small signal requirement in the TOF experiment in Figure 2.1 is met, then Equation 2.3 can be applied. The total photoinjected charge in the TOF experiment is:

$$Q_o = ep_o wA \tag{2.4}$$

where p_o is the injected hole concentration, w is the width of the charge sheet, and A is the area of the charge sheet. If the constraints on the light source mentioned above are met, then the width of the charge sheet is much less than the thickness of the sample, and the charge sheet will

essentially drift across the entire length of the sample. Under the small signal conditions, the drift velocity will remain constant $v_d = \mu F_o$ and the transit time of the charge sheet can be found as:

$$t_T = \frac{L}{v_d} = \frac{L^2}{\mu V_0} \tag{2.5}$$

The induced photocurrent in the external sampling resistor will then be:

$$i_{ph}(t) = \begin{cases} \frac{ep_o wAv_d}{L} = \frac{ep_o wA}{t_T} & 0 < t < t_T \\ 0 & t > t_T \end{cases} \tag{2.6}$$

The transient voltage response generated across the sampling resistor will be affected by the characteristics of the external circuit. The small signal equivalent circuit for the TOF experiment is shown in Figure 2.3.

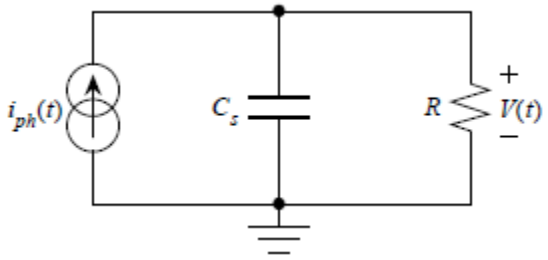

Figure 2.3: A simplified small signal AC equivalent circuit for the TOF experiment. C_S is the combination of the sample capacitance and any stray capacitances in the external circuitry.

From the small signal equivalent circuit it is seen that the induced photocurrent in the TOF experiment produces a voltage signal across an impedance, determined by the parallel combination of the sampling resistor R and the sample capacitance combined with stray capacitances from the external circuitry C_s. By performing a Laplace transform of the voltage $V(s)$ and current $I_{ph}(s)$ signals, it can be shown the relationship between the signals is:

$$V(s) = \frac{R}{sRC_s+1} I_{ph}(s) \tag{2.7}$$

Performing the inverse Laplace transform on Equation 2.7 provides an expression for the transient voltage signal $v(t)$. If the bandwidth of the photocurrent signal is arbitrarily defined as the reciprocal of the transit time, there are two solutions of the inverse Laplace transform of

Equation 2.7 that depend on the product of the sampling resistor and the capacitance C_s. If $RC_s \ll t_T$ then the inverse Laplace transform of Equation 2.7 leads to:

$$v(t) \approx \begin{cases} Ri_{ph}(t) & 0 < t < t_T \\ 0 & t > t_T \end{cases} \tag{2.8}$$

This is known as the I-mode signal because the magnitude of the transient voltage signal is directly proportional to the magnitude of the induced photocurrent signal. An ideal I-mode signal is shown in Figure 2.4 (a). The signal rises abruptly upon photoexcitation of the sample, remains constant as the photogenerated charge-carriers drift across the sample, and drops to zero when the charge-carriers reach and are collected by the bottom electrode. One inherent advantage of the I-mode signal comes from the abrupt changes in the signal magnitude that occur from charge-carrier generation and collection, which provides easy determination of the transit time of the charge sheet.

If $RC_s \gg t_T$ then the inverse Laplace transform of Equation 2.7 leads to:

$$v(t) = \frac{1}{C_s}\int_0^t i_{ph}(t')dt' \tag{2.9}$$

which simplifies to

$$v(t) \approx \begin{cases} \frac{1}{C_s}\frac{ep_owA}{t_T}t & 0 < t < t_T \\ \frac{1}{C_s}ep_owA & t > t_T \end{cases} \tag{2.10}$$

This is known as the V-mode signal, and it is the integral of the photocurrent signal. An ideal V-mode signal is shown in Figure 2.4 (b). The signal starts at zero and begins to increase linearly as the charge-carriers are generated and drift through the sample. Once the charge-carriers are collected by the bottom electrode, the signal remains constant at a value that is proportional to the total injected charge. The main advantage of the V-mode signal is that the saturation level is inversely proportional to the sample capacitance, which can be kept small to increase the signal. Further, signal integration also reduces noise. The V-mode signal has a higher magnitude and less noise than the I-mode signal.

This discussion has assumed that the sample has been free of charge-carrier traps which is generally not the case in amorphous semiconductors. The disordered nature of amorphous

semiconductors generates localized energy states within the mobility gap which form shallow and deep traps. These traps can trap charge-carriers as they travel through the sample and effectively remove them from the conduction band. As a result, the induced photocurrent will decay as the charge sheet travels across the sample as the number of charge-carriers in the charge sheet decreases.

If a set of traps located at a discrete energy level in the mobility gap with a mean trapping time of τ_c is added, there will be a large change in the observed transient voltage signal. Assuming that the release time from the traps is much longer than the transit time of the charge sheet, any charges that are trapped will not be released in the time scale of the TOF experiment. This will be the case if the traps are deep traps, that is, the traps are located at an energy level far below the conduction band. Charge-carriers in these traps have to be thermally excited over a large potential barrier to re-enter the conduction band. In this case it can be shown that the number of charge-carriers in the charge sheet will decay exponentially as they travel through the sample. Equation 2.6 can be modified to include the discrete set of deep traps:

$$i_{ph}(t) = \frac{ep_o wA}{t_T} \exp(-\frac{t}{\tau_c}) \tag{2.11}$$

Substituting Equation 2.11 into Equation 2.8 results in a modified I-mode signal equation:

$$v(t) = \begin{cases} R\frac{ep_o wA}{t_T} \exp(-\frac{t}{\tau_c}) & 0 < t < t_T \\ 0 & t > t_T \end{cases} \tag{2.12}$$

The modified V-mode signal equation is found by integrating Equation 2.11

$$v(t) \approx \begin{cases} \frac{ep_o wA\tau_c}{C_s t_T}\left(1 - \exp\left(-\frac{t}{\tau_c}\right)\right) & 0 < t < t_T \\ \frac{ep_o wA\tau_c}{C_s t_T}\left(1 - \exp\left(-\frac{t_T}{\tau_c}\right)\right) & t > t_T \end{cases} \tag{2.13}$$

This expression is known as the Hecht relationship and has been used to estimate the trapping time of charge carriers from TOF photocurrent signals [18]. The modified I-mode and V-mode signals in a sample with deep traps are shown in Figure 2.4 in comparison with the ideal I-mode and V-mode signals in a trap free sample.

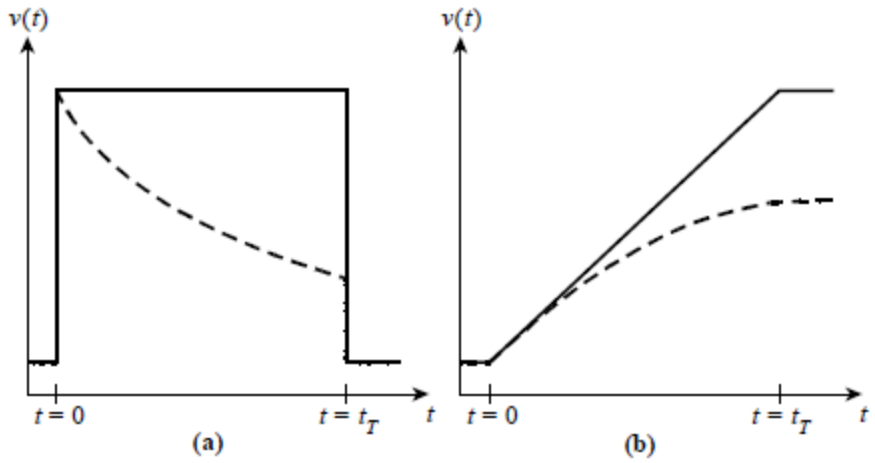

Figure 2.4: TOF transient voltage signals for the I-mode signal (a) and the V-mode signal (b). The solid lines represent the ideal case with no trapping, and the dashed lines represent the case with deep traps.

2.3 The Interrupted-Field Time-of-Flight Technique

The interrupted-field time-of-flight (IFTOF) transient photoconductivity technique is a method used to determine the deep trapping lifetime in high resistivity materials. It measures the transient response of photoinjected charge-carriers drifting across a highly resistive material with an interruption in the drift of the charge-carriers. The IFTOF technique is based on the TOF technique. A highly resistive sample of thickness L is prepared and sandwiched between two non-injecting metal electrodes. The top electrode is semi-transparent to allow light to pass through and is positively or negatively charged by the voltage V_o. The bottom electrode is grounded through a sampling resistor R. The sampling resistor R is sufficiently small so that the RC time constant (where C is the sample capacitance) is much smaller than the time domain of the transient photocurrent. The measurements are done in the I-mode.

Charge-carriers are generated at the surface of the sample by a pulse of strongly absorbed light creating electron-hole pairs through the photoelectric effect. As in the TOF experiment one charge-carrier type will be immediately collected by the top electrode. The other charge-carrier type will form a narrow charge sheet which will drift across the sample under the influence of the applied electric field. This induces an external photocurrent $i_{ph}(t)$ through the sampling resistor which can be easily measured. Assuming the small signal condition is maintained, the charge sheet will drift across the sample at a constant velocity $v_d = \mu F_o$ because the internal

electric field is uniform throughout the sample. μ is the drift mobility of the charge-carriers in the charge sheet.

The IFTOF experiment measures the deep trapping lifetime of the charge-carriers in the charge sheet by interrupting the drift of the charge sheet and allowing the charge-carriers to interact with the deep traps in the sample. At some time t_1 while the charge sheet is drifting across the sample, before it reaches the collecting electrode, the bias voltage which provides the electric field is removed. This causes the charge sheet to stop drifting through the sample and the external induced photocurrent drops to zero. The charge sheet will remain at this position $l \approx t_1 L/t_T$ until the voltage bias is reapplied to the sample at time t_2. The charge sheet will then resume drifting across the sample, inducing a post-interruption photocurrent through the sampling resistor, until the charge-carriers are collected by the bottom electrode. During the interruption time $t_i = t_2 - t_1$ the charge-carriers are able to interact with the deep traps in the sample. Some of these carriers will be removed from the conduction band by the localized states deep within the mobility gap.

In Equation 2.11 the induced photocurrent from the drift of charge-carriers through a sample with a discrete set of deep traps in the mobility gap that have a mean trapping time τ_c is shown. This equation shows that the induced photocurrent is directly proportional to the number of charge-carriers in the charge sheet.

When the bias voltage is reapplied to the sample, the post-interruption photocurrent will be smaller than the pre-interruption photocurrent because some of the charge-carriers will be trapped in the deep traps. If the traps are characterized with the capture time τ_c, the ratio of the concentration of the charge-carriers in the charge sheet after the field interruption $p(t_2)$ to the concentration before the field interruption $p(t_1)$ can be found by:

$$\frac{p(t_2)}{p(t_1)} = \exp\left(-\frac{t_i}{\tau_c}\right) \tag{2.14}$$

As the induced photocurrent is proportional to the number of charge-carriers in the charge sheet, the relation of the magnitude of the post-interruption photocurrent to the magnitude of the pre-interruption photocurrent can be inferred:

$$\frac{i(t_2)}{i(t_1)} = \exp\left(-\frac{t_i}{\tau_c}\right) \tag{2.15}$$

Equation 2.15 shows that the amount of trapping within the sample during the interruption time is represented in the change in the magnitude of the induced photocurrent from before to after the interruption of the field. Typical TOF and IFTOF waveforms for a sample with a well-defined trapping time that is larger than the transit time are shown in Figure 2.5. To get the mean carrier lifetime, several IFTOF experiments are performed with differing interruption times. The mean carrier lifetime is then found from the slope of a semi-logarithmic plot of $i(t_2)/i(t_1)$ versus t_i.

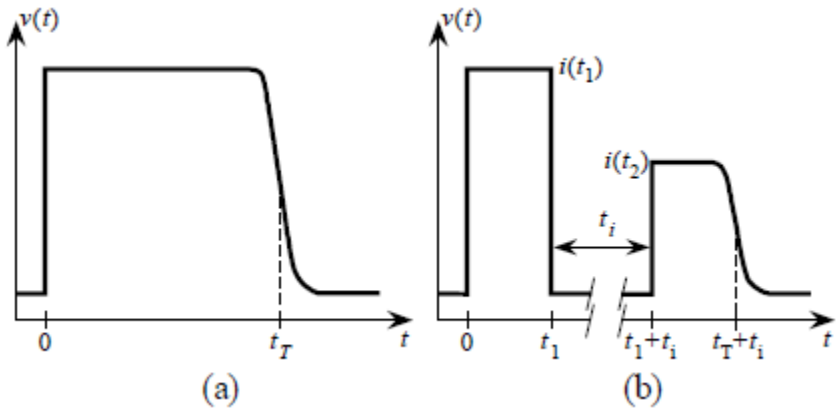

Figure 2.5: A typical TOF waveform (a) and a typical IFTOF waveform (b) in a sample with a well-defined trapping time that is greater than the transit time.

2.4 Trap-Controlled Charge Transport

The previous two sections detailed the principles of the Time-of-Flight and the Interrupted-Field Time-of-Flight transient photoconductivity techniques. The expressions for the I-mode and V-mode transient responses due to the injection and drift of charge-carriers across a highly resistive sample were developed. However, these two expressions do not match the transient responses from the actual measurements performed on amorphous semiconductors. These materials are characterized by large concentrations of localized states in the mobility gap. These states act as shallow and deep traps that can capture a charge-carrier as it drifts through a sample and have a large effect on the transport properties. In this section a trap controlled transient photocurrent theory is developed to explain the transient response that is obtained in semiconductors for three cases: monoenergetic trap distribution, binary trap distribution, and continuous extended trap distribution.

2.4.1 Monoenergetic Trap Distribution

In the monoenergetic trap distribution case, a model is made with a set of localized states at a single, well-defined energy level within the mobility gap of an amorphous semiconductor. These localized states are able to trap drifting charge-carriers, temporarily removing them from the transport band. Taking a small slice dx, of a known semiconductor, as shown in Figure 2.6, the flow of excess charge-carriers (holes in Figure 2.6) is considered. The number of free holes in the thin slice changes due to the net current flowing into the slice and the net thermal release of trapped holes within the slice. It is assumed that there is only one charge-carrier type in the sample and thus recombination can be ignored. The rate of change in the number of free holes in the slice can be expressed using the continuity equation as:

$$\frac{\partial p(x,t)}{\partial t} = -\frac{1}{e}\frac{\partial J(x,t)}{\partial x} - \frac{\partial p_t(x,t)}{\partial t} \tag{2.16}$$

where $p(x,t)$ is the concentration of free holes, $J(x,t)$ is the net current density, and $p_t(x,t)$ is the concentration of trapped holes.

The net current density flowing into the small slice of semiconductor is composed of the conduction current and the diffusion current. The conduction current is due to the drift of holes under the influence of the electric field:

$$J_C(x,t) = e\mu_o p(x,t)F(x,t) \tag{2.17}$$

where μ_o is the charge-carrier conduction mobility and $F(x,t)$ is the applied electric field. The diffusion current is due to the spatial variation in the concentration of charge carriers:

$$J_D(x,t) = -eD\frac{\partial p(x,t)}{\partial x} \tag{2.18}$$

where D is the diffusion coefficient.

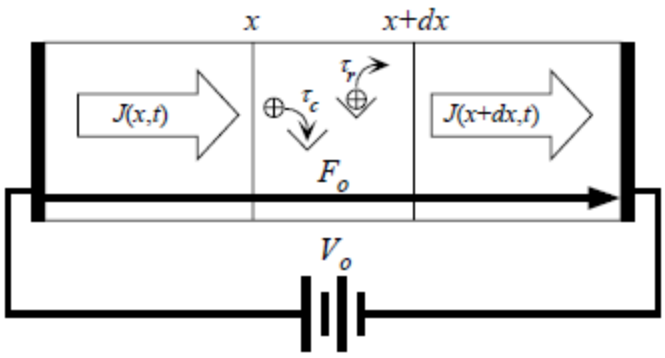

Figure 2.6: Drift of holes through a small slice *dx* of a semiconductor involving trapping and release of holes.

The total net current density is the sum of the two current components so the rate of change in the number of free holes in the thin slice can be rewritten as:

$$\frac{\partial p(x,t)}{\partial t} = -\mu_o F(x,t)\frac{\partial p(x,t)}{\partial x} - \mu_o p(x,t)\frac{\partial F(x,t)}{\partial x} + D\frac{\partial^2 p(x,t)}{\partial x^2} - \frac{\partial p_t(x,t)}{\partial t} \tag{2.19}$$

Equation 2.19 is known as the one-dimensional continuity equation for holes. The one-dimensional continuity equation for electrons is found using similar arguments:

$$\frac{\partial n(x,t)}{\partial t} = -\mu_o F(x,t)\frac{\partial n(x,t)}{\partial x} - \mu_o n(x,t)\frac{\partial F(x,t)}{\partial x} + D\frac{\partial^2 n(x,t)}{\partial x^2} - \frac{\partial n_t(x,t)}{\partial t} \tag{2.20}$$

where $n(x,t)$ is the concentration of free electrons, and $n_t(x,t)$ is the concentration of trapped electrons.

The rate of change in the number trapped holes and electrons, $\partial p_t(x,t)/\partial t$ and $\partial n_t(x,t)/\partial t$ respectively, are known as the rate equations and they represent the difference in instantaneous trapping and release rates of the charge-carriers. These rate equations can be expressed as:

$$\frac{\partial p_t(x,t)}{\partial t} = \frac{p(x,t)}{\tau_c} - \frac{p_t(x,t)}{\tau_r} \tag{2.21}$$

and

$$\frac{\partial n_t(x,t)}{\partial t} = \frac{n(x,t)}{\tau_c} - \frac{n_t(x,t)}{\tau_r} \tag{2.22}$$

where τ_c and τ_r are the mean capture time and mean release time of the traps respectively.

By simultaneously solving the rate equation and the continuity equation for a single charge-carrier type, an expression for the time dependence of the charge-carrier density in the charge sheet can be derived. To make this easier, several assumptions can be made. First is that the small signal condition is met, which causes the electric field to be uniform throughout the sample, and $\partial F(x,t)/\partial x = 0$. Second, the diffusion current portion of the net current density can be assumed to be negligible compared with the conduction current and therefore can be ignored.

Boundary conditions for the expressions in Equations 2.19 and 2.21 can be determined by considering the TOF experiment. At time $t = 0$ the photoexcitation pulse generates a thin charge sheet of holes at position $x = 0$. The distribution of the generated holes $p(x,t)$ can be approximated as a delta function if the absorption depth of the light source is small compared to the length of the sample.

$$p(x,0) = N_{oh}\delta(x,0) \tag{2.23}$$

where $N_{oh} = p_o wA$ is the number of photogenerated holes. As the holes have not traveled across the sample, it can be assumed the hole traps are all unoccupied. Thus:

$$p_t(x,0) = 0 \text{ for } x > 0 \tag{2.24}$$

Once the charge sheet has drifted across the sample, the charge carriers are collected by the bottom electrode. Thus:

$$p(x,t) = 0 \text{ for } x > L \tag{2.25}$$

There also cannot be any traps outside of the sample, thus:

$$p_t(x,t) = 0 \text{ for } x > L \tag{2.26}$$

Equations 2.19 and 2.21 can be solved using these boundary conditions and Laplace transform techniques as shown in References [26, 27]. The resulting expression for the free hole density as the hole sheet travels through a sample is:

$$p(x,t) = \frac{N_{oh}}{\mu_o F}\exp\left(-\frac{z}{\tau_c}\right)\delta(t-z) + \frac{N_{oh}}{\mu_o F}\exp\left(-\frac{z}{\tau_c}-\frac{t-z}{\tau_r}\right)\frac{\xi}{2}\frac{I_1(\xi)}{(t-z)}U(t-z) \tag{2.27}$$

where $z = x/\mu_o F$, $I_1(\xi)$ is the first order hyperbolic Bessel function, $U(x)$ is the unit step function, and $\xi = \left(2\sqrt{\tau_c z(t-z)/\tau_r}\right)/\tau_c$. The first term containing the delta function $\delta(x)$, represents the number of holes remaining in the charge sheet as it drifts across the sample. These charge-carriers are not delayed by trapping and release as they travel through the sample, but decreases exponentially as $\exp(-z/\tau_c)$. The second term containing the first order hyperbolic Bessel function represents holes that have been trapped and are removed from the delta charge sheet. At some time t these carriers are released back into the transport band and lag behind the delta charge sheet. The delta charge sheet exits the sample at the collecting electrode at the transit time t_T and the lagging charge-carriers continue inducing a photocurrent for times longer than the transit time. The charge-carriers in the second term may suffer more than one trapping and release events. A similar expression for the free electron density can be found using similar arguments.

The time dependence of the number of free holes in the charge sheet can be found by integrating Equation 2.27 over the entire length of the sample. The resulting expression can be used to obtain an expression for the I-mode transient photocurrent response. However this expression is extremely complex to work with. The transient current response can be simplified by evaluating in two limiting cases: low field drift and high field drift. These cases do not impose serious restrictions on predicting the transient current response in TOF experiments because they can be easily met by the appropriate choices of sample thickness, bias voltage, and temperature.

2.4.1.1 Low Fields: Shallow Trap Controlled Transport

In the case of low field drift, it is assumed that the transit time of the charge-carriers is much longer than the charge-carrier capture time and is comparable to the release time ($\tau_r \approx t_T = L/\mu_o F \gg \tau_c$). Free charge-carriers in the charge sheet are captured by a set of localized traps that are close to the conduction band edge. Once the charge-carriers are released they continue to drift towards the collecting electrode. As the release time and the transit time are comparable, the time derivatives of the free charge-carrier densities in Equations 2.19 and 2.20 vanish over a long period of time [28]. That is, the number of free charge-carriers will enter a steady state. Using the principle of charge conservation and the rate equation for holes, it can be shown that the number of free holes N_h in steady state can be related to the total injected charge by:

$$N_h = N_{oh}\frac{\tau_c}{\tau_c+\tau_r} \tag{2.28}$$

where $N_{oh} = p_o wA$ is the total number of photoinjected holes. The I-mode signal can be found by substituting Equation 2.28 into Equation 2.6.

$$i_{ph} = \frac{eN_{oh}\mu_o F}{L}\frac{\tau_c}{\tau_c+\tau_r} = \frac{eN_{oh}\mu F}{L} \tag{2.29}$$

This resembles the equation for the trap free I-mode photocurrent signal with the drift mobility μ_o reduced to μ by:

$$\mu = \frac{\tau_c}{\tau_c+\tau_r}\mu_o = \theta\mu_o \tag{2.30}$$

where $\theta = \tau_c/(\tau_c + \tau_r)$. The I-mode signal is found by substituting Equation 2.29 into Equation 2.8. A comparison of the I-mode signals of the trap free case and the low field case of the monoenergetic trap distribution case is shown in Figure 2.7. The effective charge-carrier drift mobility is reduced due to the trapping and releasing events that occur as the charge sheet travels through the sample. This transport mechanism is called shallow trap-controlled transport, and the scalar θ is referred to as the shallow trap-controlled transport factor.

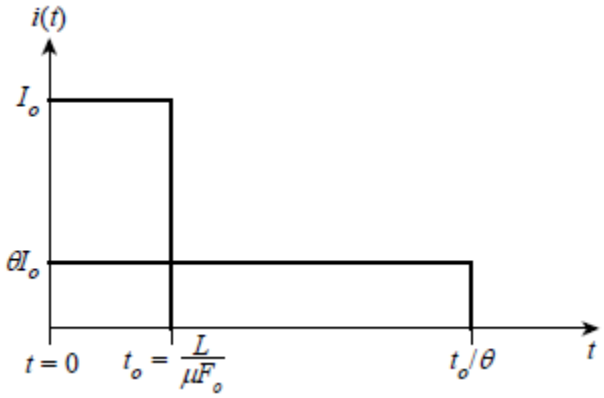

Figure 2.7: Comparison of the I-mode signals for the trap free drift mobility and the shallow trap controlled transport models.

2.4.1.2 High Fields

In the case of high field drift, the transit time of the injected charge-carriers is shorter than the carrier capture time ($t_T = L/\mu_o F < \tau_c$) allowing some of the charge-carriers to travel

the entire length of the sample without trapping. The expressions for the TOF transient signal were developed in two different time ranges in Reference [29]. The first expression is:

$$i_{ph}(t) = \frac{eN_{oh}}{t_T}\left(\frac{\tau_c}{\tau_c+\tau_r} + \frac{\tau_r}{\tau_c+\tau_r}\exp\left(-\frac{\tau_c+\tau_r}{\tau_c\tau_r}t\right)\right) \text{ for } 0 < t < L/\mu_o F \tag{2.31}$$

where $N_{oh} = p_o wA$ is the total number of injected holes. If the carrier release time is neglected by allowing $\tau_r \to \infty$ then Equation 2.31 reduces to the case of deep trapping in Equation 2.11.

The second expression is for those charge-carriers that are trapped and released. Once released back into the transport band, most of these carriers will be collected at the bottom electrode without further trapping. The transient response due to the released charge-carriers is shown to be:

$$i_{ph}(t) = \frac{eN_{oh}}{2}\frac{\tau_r}{\tau_c\tau_r}\exp\left(-\frac{t}{\tau_r}\right) \text{ for } t > L/\mu_o F \tag{2.32}$$

These equations show that the transient photocurrent response will initially decay exponentially as the injected charge sheet drifts through the sample. Then at $t = L/\mu_o F$ a step down in the magnitude will occur and another exponential decay back to zero as the trapped charge-carriers are released and collected. This photocurrent response is shown in Figure 2.8.

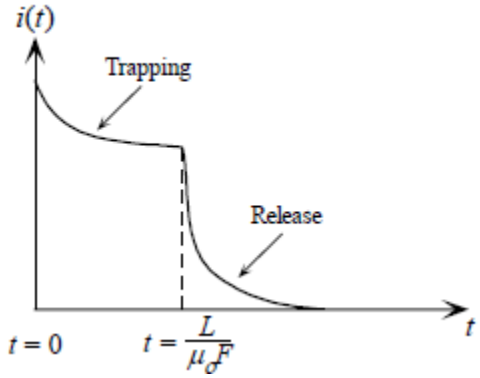

Figure 2.8: TOF transient photocurrent response from the high field model of the monoenergetic trap distribution.

2.4.2 Binary Trap Distribution

In the binary trap distribution case, a model is made with two sets of localized states at well-defined energy levels within the mobility gap of an amorphous semiconductor. These

localized states are characterized by two separate capture times, τ_{c1} and τ_{c2}, and two release times, τ_{r1} and τ_{r2}. An expression for the transient photocurrent response will be more complicated than the monoenergetic distribution with only one set of discrete traps. To simplify the analysis, it is assumed that the concentration of the injected charge-carriers is much less than the concentration of traps at both energy levels. This allows the effect of trap filling to be ignored. It is also assumed that the number of charge-carriers at a trap level may only increase by trapping a free charge-carrier in the transport band, and not from the release of carriers from traps at a lower energy level in the mobility gap. The hole rate equations for this trap distribution are:

$$\frac{\partial p_{t1}(x,t)}{\partial t} = \frac{p(x,t)}{\tau_{c1}} - \frac{p_{t1}(x,t)}{\tau_{r1}} \tag{2.33}$$

and

$$\frac{\partial p_{t2}(x,t)}{\partial t} = \frac{p(x,t)}{\tau_{c2}} - \frac{p_{t2}(x,t)}{\tau_{r2}} \tag{2.34}$$

By simultaneously solving Equation 2.33, Equation 2.34, and the hole continuity equation in Equation 2.19, an expression for the time dependence of the concentration of holes in the charge sheet can be found. The total trap concentration is the combination of the trapped holes at the two energy levels $p_t(x,t) = p_{t1}(x,t) + p_{t2}(x,t)$. The following expression for the transient photocurrent response is developed in Reference [30].

$$j(t) = A\exp(-\alpha t) + B\exp(-\beta t) + j_\infty \tag{2.35}$$

where

$$\alpha + \beta = \frac{1+\theta_1}{\tau_{c1}} + \frac{1+\theta_2}{\tau_{c2}} \tag{2.36}$$

$$\alpha\beta = \frac{[\theta_1+\theta_2(1+\theta_1)]}{\tau_{c1}\tau_{c2}} \tag{2.37}$$

$$\alpha A + \beta B = \frac{j_o}{\tau_{c1}} + \frac{j_o}{\tau_{c2}} \tag{2.38}$$

$$\alpha + \beta + j_\infty = j_o \tag{2.39}$$

and

$$j_\infty = \frac{j_o\theta_1\theta_2}{[\theta_1+\theta_2(1+\theta_1)]} \tag{2.40}$$

where $\theta_1 = \tau_{c1}/\tau_{r1}$ and $\theta_2 = \tau_{c2}/\tau_{r2}$. The term j_∞ represents the steady state current that flows after the injected charges have come to equilibrium with the traps.

The case where one set of traps is located deep enough in the mobility band that the release time of the captured charge-carriers is long compared to the transit time ($\tau_{r2} \to \infty$) should be noted. In this case $\theta_2 = 0$, and Equation 2.35 reduces to:

$$j(t) = A\exp\left(-\frac{t}{\tau_{c1}}\right) + B\exp\left(-\frac{t}{\tau_{c2}}\right) \tag{2.41}$$

This transport mechanism is called shallow-trap controlled transport with deep trapping, and is often used to describe transport in amorphous selenium [31, 32]. The first term represents an initial spike that decays exponentially until the carriers reach equilibrium with the shallower traps. This is followed by a slower exponential decay with a characteristic decay rate of τ_{c2}/θ_1.

It should be noted that the measured lifetime in the IFTOF experiment is actually θ/τ_{c2}. τ_{c2} is the trapping time into the set of traps from which there is no release and it depends on the total concentration of deep traps.

$$\frac{1}{\tau_{c2}} = \sigma u N_T \tag{2.42}$$

where σ is the capture cross section, u is the mean speed of the charge-carriers (usually taken as the thermal velocity 10^7 m/s), and N_T is the total trap concentration found by integration of the density of localized energy states $N_T(E)$ over the energies in which there are deep traps.

$$N_T = \int_{E_1}^{E_2} N_T(E)dE \tag{2.43}$$

where E_1 and E_2 define the energy range where the localized energy states are deep.

The TOF/IFTOF experiments provide an effective lifetime τ which is τ_{c2}/θ. Thus:

$$\frac{1}{\tau} = \frac{\theta}{\tau_{c2}} = \theta\sigma u N_T \tag{2.44}$$

The calculation of N_T from the measurement of the effective lifetime requires knowing θ, σ, and u. θ can be found from μ/μ_o and σ can be taken as a typical capture cross section for the particular capture process that is assumed to exist (trapping by neutral or charged traps). Note the product $\mu\tau$, which determines the charge collection efficiency, does not depend on θ.

$$\mu\tau = \mu_o\tau_{c2} = \frac{\mu_o}{\sigma u N_T} \tag{2.45}$$

2.4.3 Extended Trap Distribution

The derivation for the trap limited response in the case of an extended distribution of traps becomes more complex than the previous cases. One approach would be to divide the continuum of traps into a finite number of discrete isoenergetic levels [33]. The solution for the time dependence of the concentration of charge-carriers is derived using similar arguments to those in the previous cases. This is beyond the scope of this investigation but may be found in References [34, 35, 36]. For a narrow distribution of traps that cause charge-carriers to become trapped and released several times while drifting through a sample, it can be shown that the dispersion of charge-carriers in the drifting charge sheet can be approximated using a Gaussian function. The photocurrent response will then have a tail that will follow the approximate normal probability function with a variance given by:

$$\Delta t = \frac{2\tau_t^2 L}{\tau_c \mu_o F} \tag{2.46}$$

This spread is greater that what is expected from charge-carrier dispersion and is observed in a number of materials such as a-Se: 0.3% As [38] which is used in the current investigation.

2.5 Summary

In this chapter, the principles behind the time-of-flight and the interrupted-field time-of-flight experiments were first introduced. The TOF experiment measures the external transient response caused by the drift of photogenerated charge-carriers through a sample of highly resistive material and is used to determine the charge-carrier drift mobility. The IFTOF experiment also measures the transient response caused by the drift of photogenerated charge-carriers, but interrupts the drift of the charge-carriers to allow them to interact with the deep traps in the sample. This experiment is used to determine the charge-carrier lifetime. As the mobility-lifetime product has a large effect on the device performance, accurate measurements of the charge-carrier drift mobilities and lifetimes are important.

Secondly, the transient photocurrent signal responses for several trap distributions which are encountered in amorphous semiconductors were developed. Shallow traps were found to cause multiple trapping and releasing events which caused the transit time to increase. This is due to the finite amount of time each trapped charge-carrier spent in each trap. Deep traps were

found to cause the photocurrent signal to decrease exponentially, with a decay rate that corresponds to the trapping time τ_c. The TOF and IFTOF techniques are able to measure the drift mobility and lifetime of the charge-carriers with good accuracy, and can therefore be used to investigate the distribution of energy states in the mobility gap in amorphous semiconductors. Both the TOF and IFTOF techniques are therefore very important tools that can be used to study the fundamental charge transport properties in amorphous semiconductors.

3. Experimental Procedure

3.1 Introduction

The experimental procedure used to study the charge-carrier transport properties in stabilized amorphous selenium (a-Se) photoconductive layers is described in this chapter. The fabrication of the samples on which the experiments are performed is first described. Second, an overview of the time-of-flight (TOF) and interrupted-field time-of-flight (IFTOF) methods are presented. The calculations to determine the electrical properties from the experimental data and difficulties in implementing the experiments are included. Third, the experimental setup used is described in detail. Fourth, the x-ray system used in this investigation is detailed along with the calculation of x-ray dose absorbed by a sample. Finally, the experimental procedure for doing accumulated dose measurements is described.

3.2 Sample Preparation

The amorphous selenium samples used in this investigation were prepared using conventional vacuum evaporation deposition. Vitreous selenium pellets, alloyed with a small amount of arsenic and doped with chlorine, are placed into a NRC 3117 stainless steel vacuum coater system which is shown in Figure 3.1. Pure a-Se is normally alloyed with small amounts of As because pure a-Se layers are not thermally stable and crystallize over time. Adding a small amount of As slows this crystallization process, but in turn causes the hole lifetime to decrease. To counter this side effect and keep the hole lifetime long, the a-Se sample is doped with Cl in the pmm range. The resulting thermally stable film is called stabilized a-Se and is denoted, for example the samples used in this investigation, as a-Se: 0.3% As + 10 ppm Cl. Stabilized a-Se will hereafter be simply referred to as a-Se. The source material was supplied by Analogic Canada Corporation. The actual As content in two representative films was measured using an Energy Dispersive X-ray Fluorescence Spectrometer S2 PUMA, Bruker Corporation equipped with a SMART-QUANT FP module for standard less analysis. The average As concentration across the samples was 0.29 ± 0.02% and 0.33 ± 0.02% in the two films, which is close to the As concentration in the bulk source material. The exact Cl content at the ppm level is difficult to measure but is known to be much less than in the starting bulk material.

Two different substrates were used for the samples. The first set are cleaned corning glass covered with a layer of oxidized aluminum. The aluminum layer on these substrates is thin but of sufficient conductance to serve as the bottom electrode. The oxide layer on the Al provides an amorphous base for the a-Se film to be grown. The second set of substrates use a thin layer of ITO as the bottom electrode which also serves as an amorphous base to grow the a-Se film.

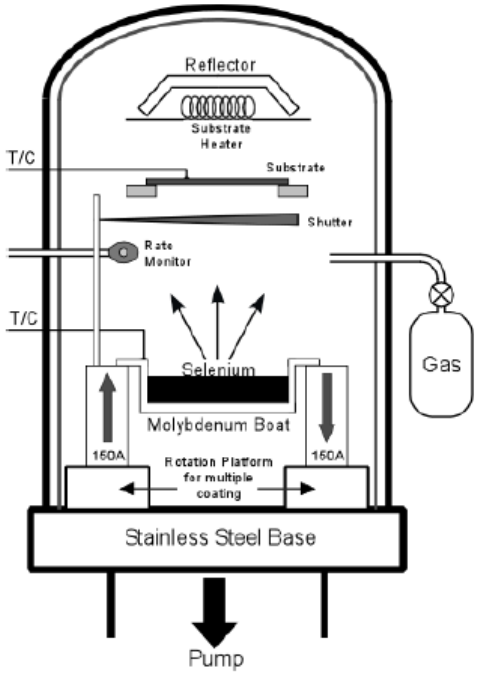

Figure 3.1: Schematic diagram of the NRC 3117 vacuum deposition system.

Vacuum deposition of the samples begins by placing the substrate and the source material into the system and evacuating the chamber to a base pressure of ~ 10^{-6} Torr. The stabilized selenium pellets are placed in a molybdenum boat, which is heated to a temperature of ~ 250 °C by passing a large ac current (100-150 A) through it. This causes the selenium to begin to evaporate. A substrate heater is used to keep the glass substrate at ~ 60°C, which is just above the glass transition temperature of a-Se, in order to allow the Se atoms to arrange themselves into a structurally relaxed amorphous state as they condense on the substrate. Both the substrate and the boat temperatures are carefully monitored using thermocouples and a digital quartz crystal rate monitor is used to monitor the evaporation rate of the a-Se. The temperature of the boat determines the rate of the evaporation and the substrate temperature has a large effect on the

sample condition. A mechanical shutter covers the substrate until a steady state of evaporation is reached, at which time the shutter is opened and the a-Se begins to condense onto the substrate. After the desired film thickness is reached, the shutter is closed to stop further condensation onto the sample. When the evaporation rate of the Se becomes small, the current passed through the boat is turned off. The samples are kept in the evacuated chamber for 24 hours to allow the substrate and boat to cool down to room temperature while the chamber is still evacuated. The sample is then removed and placed in a dark location for 2-3 days to allow its physical properties to stabilize [38].

The final step in the sample preparation is placing an electrical contact on the top of the a-Se film. A conducting semitransparent thin film of gold is used as the top electrode and is sputtered onto the sample using a Hummer VI sputtering system which is shown in Figure 3.2. The a-Se sample is covered with an aluminum mask with a circular hole with an area of 0.5 cm^2 exposing the sample. The sample is then placed into the vacuum chamber of the sputtering system, which is pumped down to a pressure of 100 mTorr and is flooded with argon gas. The application of a high voltage between the anode and cathode of the system ionizes the argon gas molecules in the chamber. The positively charged ions then begin to collide with the negatively charged gold target, dislodging gold particles. These gold particles then drift and coat the exposed a-Se with a uniform coating. The sputtered gold films are sufficiently thin to be transparent and have an edge-to-edge resistance of around 50 Ω.

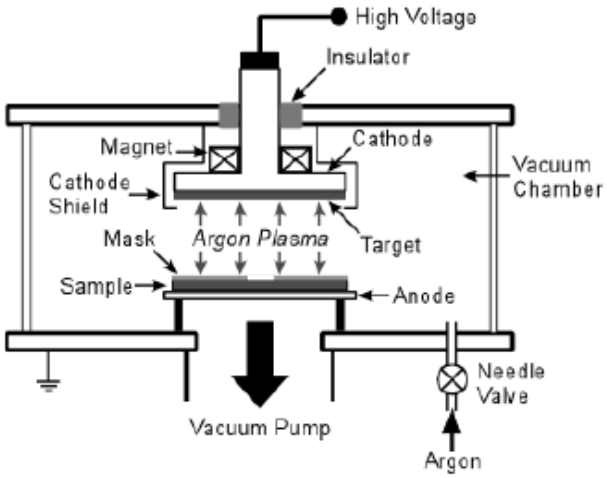

Figure 3.2: Schematic diagram of the Hummer VI sputtering system.

Once the semitransparent gold contact is applied to the a-Se sample, it is ready to be placed into the sample holder of the TOF/IFTOF apparatus. Contact is made to the sample through stainless steel needles with a small piece of indium to help with conduction and to protect against puncturing the thin Au film. The sample is covered using a black paper mask with a circular hole slightly smaller than the top contact in order to keep photogeneration out of the fringe fields. Typical samples with aluminum and ITO substrates are shown in Figure 3.3.

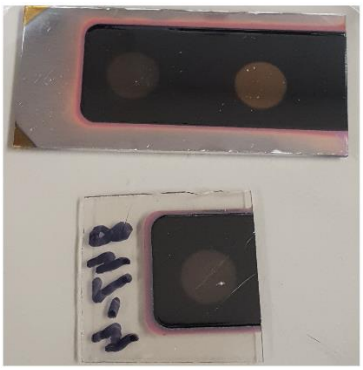

Figure 3.3: Typical 72 μm thick a-Se: 0.3% As + 10 ppm Cl samples. The top sample has an aluminum substrate and the bottom sample has an ITO substrate.

3.3 Time-of-Flight and Interrupted-Field Time-of-Flight Experimental Overview

The charge-carrier transport properties, lifetime and drift mobility, in a-Se photoconductive layers were investigated using conventional Time-of-Flight (TOF) and Interrupted-Field-Time-of-Flight (IFTOF) transient photoconductivity measurements. These experiments measure the transient response resulting from the drift of charge carriers across a semiconductor or insulator. A simplified schematic of a system capable of performing these measurements is shown in Figure 3.4. In this schematic, the voltage source can be constant for the TOF measurement or pulsed for the IFTOF measurement. When the light source is pulsed, electron-hole pairs will be generated near the surface under the semi-transparent top contact. The light source chosen must have a wavelength that closely matches the bandgap of the sample as well as a short pulse length in order to ensure strong absorption at the surface and that the generated sheet of charges is narrow. Some of the light sources which have been used in literature for photoexcitation near the surface of a-Se include nitrogen lasers, Xenon flash lamps,

and pulsed electron beams [19, 38, 39]. Depending on the polarity of the applied bias voltage, one charge-carrier type will be immediately collected by the top electrode (electrons in the case of positive bias in Figure 3.4). The other charge carrier type creates a thin charge sheet, which drifts through the sample. The drift of the carriers through the sample gives rise to an external photocurrent $i(t)$, which is passed through a sampling resistor converting the photocurrent signal into a voltage signal $V(t) = Ri(t)$. The voltage $V(t)$ generated across the sampling resistor is amplified and recorded by the oscilloscope. The oscilloscope is synchronized with the light source to capture the transient photocurrent signal.

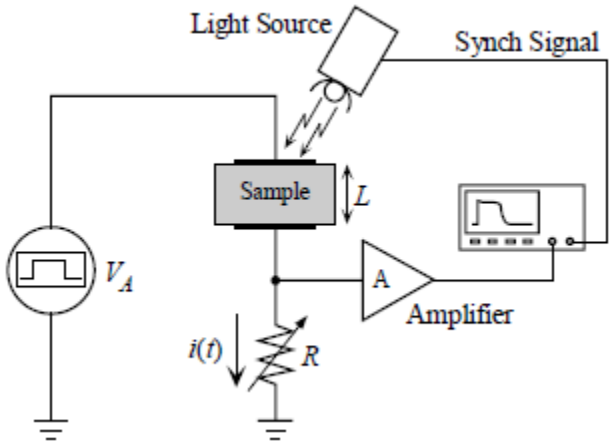

Figure 3.4: A simplified schematic of a system capable of performing TOF and IFTOF measurements. In the schematic, electrons will be collected by the top electrode and holes will drift across the sample. The voltage source V_A may be constant for the TOF experiment or pulsed for the IFTOF experiment. The oscilloscope is synched with the light source to ensure the capture of the transient signal.

As the captured signal is directly proportional to the value of the sampling resistor, the magnitude of the signal can be increased by simply increasing the resistance of the sampling resistor. This however will increase the RC time constant of the system, where C is the sample capacitance combined with the stray capacitances of the cables and the electronics. If the RC constant is too large, the bandwidth of the system becomes limited and the signal captured by the oscilloscope will be distorted. For proper I-mode (current mode) TOF detection, R should be selected such that $RC << t_T$, where t_T is the TOF transit time.

The TOF transient photoconductivity technique captures the transient response of photo-injected carriers as they travel through a sample of a highly resistive material. This experiment is used to find the charge-carrier drift mobility in the sample. The technique was first introduced by Spear [40], Kepler [41], LeBlanc [42], and Brown [43], and several modifications, such as different light sources, high voltage schemes, and advanced photoexcitation techniques to study bulk space charge buildup effects [44] have appeared over time. The timing of the bias voltage and a typical hole photocurrent signal in the TOF experiment are shown in Figure 3.5 (a).

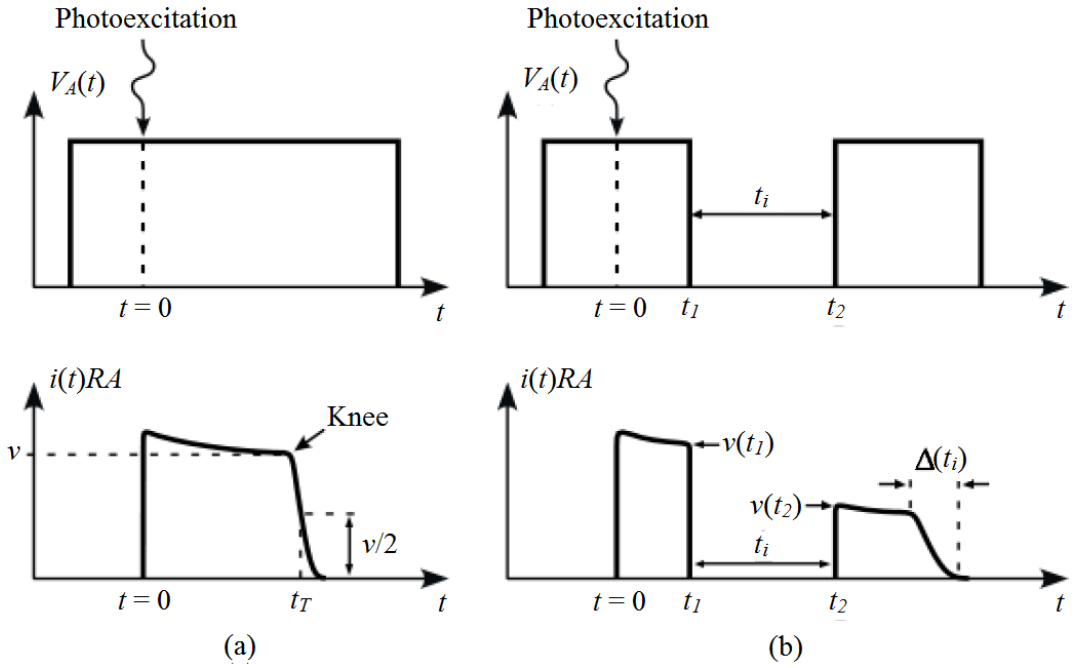

Figure 3.5: The transient I-mode photocurrent signal for the (a) TOF and (b) IFTOF experiments. The diagram also shows how the bias voltage is applied and interrupted. The drift mobility is found by measuring the width of the TOF pulse, that is, the transit time t_T. The lifetime is found by measuring the ratio of the recovered photocurrent to the initial photocurrent in the IFTOF pulse.

In the TOF experiment a bias voltage is placed across the a-Se sample before $t = 0$. The delay between turning on the bias voltage and triggering the light source allows the high voltage switching transients to settle. The light source is triggered at $t = 0$ and photons are absorbed just below the top contact resulting in the generation of electron-hole pairs. Depending on the polarity of the bias voltage, either holes or electrons will create a charge sheet and drift across the sample, inducing an external transient photocurrent which is converted to a voltage by the

sampling resistor and is amplified and captured by the oscilloscope. The external photocurrent drops to zero once all the charge-carriers reach and are collected by the bottom electrode. The ideal transit time, in the absence of spreading of the injected charge sheet, is defined as the time width of the TOF transient I-mode photocurrent signal, which is the time it takes from the photogeneration of the charge carriers to the collection of the charge carriers. However, the falling edge of the transient photocurrent is typically spread out and this spread is referred to as a photocurrent tail. This photocurrent tail is due to the dispersion of charge carriers, mutual Coulombic repulsion between the charge carriers (which is tantamount to the perturbation of the applied field), and multiple trappings in the shallow traps as the charge-carriers travel through the sample. The transit time of the charge-carriers is typically found at the time when the current at the "knee' of the photocurrent falls down to half magnitude as shown in Figure 3.5 (a). This corresponds to the point where approximately half of the charge-carriers have been collected.

The transit time of the captured signal is related to the charge-carrier drift mobility as shown in Equation 3.1 with a couple simplifying assumptions. First it is assumed that the charge-carriers travel across the entire length of the sample as the electron-hole pairs are generated very near the surface. Second it is assumed that the internal electric field is constant and the charge-carriers have a constant drift velocity, put differently a constant drift mobility. These assumptions are met if the sample is under small signal conditions, described in Chapter 2. With these assumptions the drift mobility is:

$$\mu_{h,e} = \frac{L^2}{V t_T} \tag{3.1}$$

where $\mu_{h,e}$ is either the hole or electron drift mobility, L is the thickness of the sample measured in cm, V is the bias voltage applied to the sample, and t_T is the transit time of the charge-carriers. A typical example of a transient I-mode photocurrent signal during a TOF experiment is shown in Figure 3.6.

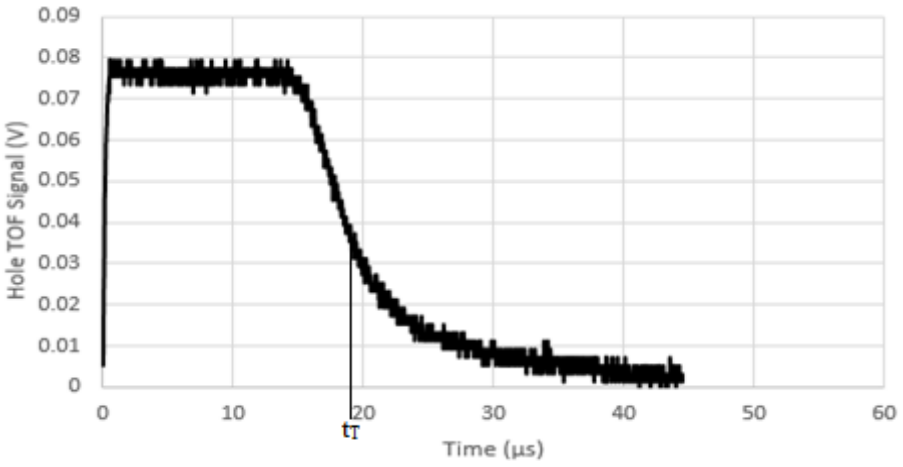

Figure 3.6: A typical TOF signal for holes. The transit time is defined as the point where the photocurrent signal drops to half of the knee point value.

The IFTOF transient photoconductive experiment captures the transient response of photo-injected carriers as they travel through a sample of highly resistive material with an interruption in the drift of the charge-carriers. This experiment is used to find the carrier deep trapping time, or the carrier lifetime, in the sample. The timing and a typical hole IFTOF signal are shown in Figure 3.5 (b). In the IFTOF experiment a bias voltage is placed across the sample before $t = 0$ and the light source is triggered at $t = 0$ just as in the TOF experiment. Depending on the polarity of the bias voltage, either holes or electrons will drift across the sample giving rise to an external photocurrent which is converted to a voltage by the sampling resistor and is captured by the oscilloscope. At time $t = t_1$ the bias voltage is removed and the charge carriers stop drifting through the sample resulting in a drop of the induced photocurrent to zero. Then at time $t = t_2$ the bias voltage is reapplied allowing the charge carriers to continue drifting through the sample causing the induced photocurrent to increase. During the interruption time, defined as $t_i = t_2 - t_1$, the charge-carriers are able to interact with the deep traps in the sample. Some of these carriers will become trapped in the deep traps, becoming effectively removed from the charge sheet. There is therefore a resulting drop in the magnitude of the induced photocurrent before and after the interruption. This change in the induced photocurrent is related to the lifetime of the charge carriers as follows [45]:

$$\tau_{h,e} = \frac{t_i}{\ln[i(t_2)/i(t_1)]} \tag{3.2}$$

where $\tau_{h,e}$ is the carrier deep trapping time (lifetime) of holes or electrons, t_i is the interruption time, $i(t_2)$ is the magnitude of the photocurrent signal just after the interruption, and $i(t_1)$ is the magnitude of the photocurrent signal just before the interruption. A typical example of the transient photocurrent during an IFTOF experiment is shown in Figure 3.7.

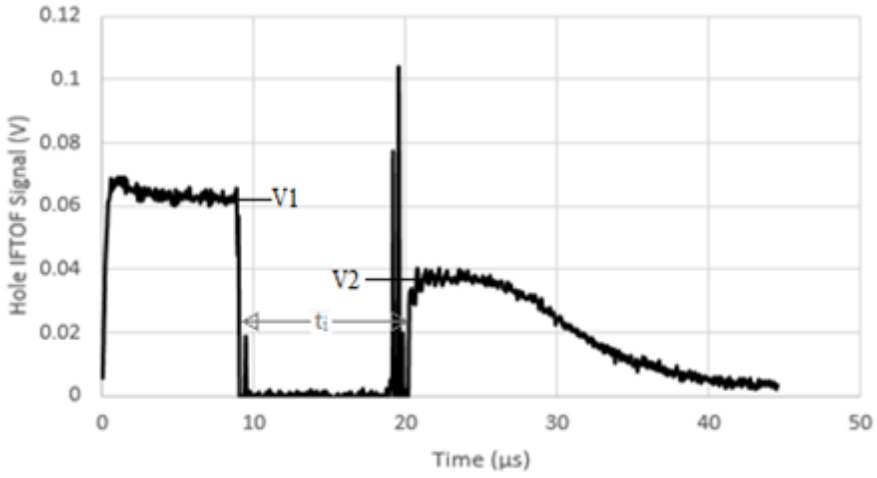

Figure 3.7: A typical IFTOF signal for holes, free of the high displacement currents.

To get a more accurate measurement of the charge-carrier lifetime, several IFTOF measurements can be done with different interruption times. Then, by plotting the ratio of the photocurrent signal after the interruption to that before the interruption against the interruption time on a semi-logarithmic plot, the carrier lifetime can be found from the reciprocal of the slope. A typical example of the semi-log plot used to obtain the charge-carrier lifetime is shown in Figure 3.8.

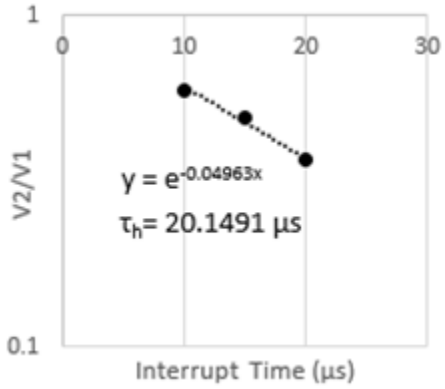

Figure 3.8: A typical semi-log plot of the ratio of the photocurrent signal drop against the interruption time.

During the interruption of the bias voltage, the charge-carrier sheet does not move, however it does spread out due to diffusion and Coulombic repulsion (internal field due to the photogenerated carriers). Because of this, the interruption time should not be too long nor should the interruption occur when the carrier sheet is near one of the contacts. In either case charge-carriers may end up being collected by one of the electrodes, causing an additional drop in the external photocurrent once the bias voltage is reapplied. This drop in the photocurrent will add to the drop in the photocurrent due to the trapping of charge-carriers, and the IFTOF measurement will be inaccurate. If the width of the photocurrent tail of the recovered pulse does not reach the length of interruption time, it can be assumed that charge carriers were not collected by the electrodes during interruption.

The IFTOF experiment has some extra difficulties in its implementation. When switching the bias voltage on and off during the IFTOF experiment, there are large high voltage switching transient currents that are introduced. The a-Se sample is essentially a parallel-plate capacitor which is combined in series with the sampling resistor. This creates an *RC* time constant which introduces high displacement currents from switching the high voltage. These displacement currents can completely dwarf the transient photocurrent signal which is being measured as well as cause damage to the circuitry. This is not a problem in the TOF experiment as the bias voltage is applied with sufficient time before the photoexcitation, and protection may be achieved with a simple relay. This relay opens when the high voltage is applied and closes after a time delay allowing the displacement currents to settle. A simple relay doesn't work in the IFTOF experiment however as the switching time of typical relays is several orders of magnitude larger than the transit time of the charge-carriers.

Several techniques to eliminate the displacement currents have been published in literature [32, 46, 47]. In this investigation, in order to minimize the displacement currents, a grounded bridge network is used with a differential amplifier which picks out the IFTOF signal. A schematic of a grounded bridge network is shown in Figure 3.9. The variable capacitor C_N is adjusted to match the sample capacitance. With the matched branches of the bridge, the displacement currents will be equal in both branches of the grounded bridge network and the differential amplifier can measure the photocurrent from the sample. These high displacement currents also place hard restrictions on the amplifier, such that it would need a large CMRR

(~ 100 dB) over a large bandwidth without saturating. To reduce the constraints on the amplifier, six fast diodes are placed across each of the bridge resistors. In the schematic shown in Figure 3.9 each diode shown (i.e. $D_1 - D_4$) contains three diodes in series. This limits the displacement current signal to ~ 1.8 V. Limiting the displacement currents prevents the amplifier from saturating and an amplifier with ~ 60 dB CMRR can be used for the setup, as long as the resistors are closely matched. During the photocurrent measurement, the signal across the sampling resistor R is much less than 0.6 V and the diodes have a high dynamic resistance and do not affect the measurement.

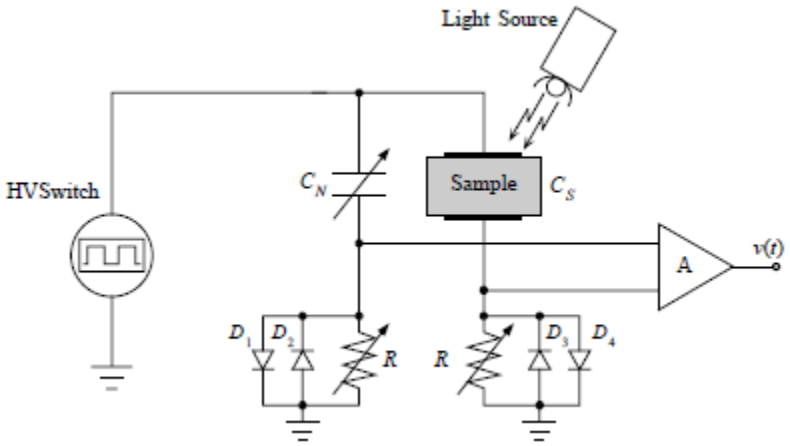

Figure 3.9: A grounded bridge network to eliminate the large displacement currents introduced from high voltage switching in the IFTOF system. Each of the diodes D_1, D_2, D_3, and D_4 contains three fast diodes in series.

3.4 Laser Time-of-Flight and Interrupted-Field Time-of-Flight Experimental System Overview

The laser TOF/IFTOF experimental system contains a laser, a trigger system, a high voltage supply and switch, an amplifier system, and a control and data acquisition system. A nitrogen gas laser is used to generate a very short light pulse that is absorbed near the surface of a sample, generating electron-hole pairs. An EG&G Ortec high voltage power supply is used to supply the bias voltage to the samples through the high voltage switch, which is used to perform the interruption in the IFTOF measurements using fast switching HV HEXFET switches. The amplifier system is used to amplify the induced photocurrent signal from the drift of charge-carriers through the sample as the transient photocurrent is very small. The trigger system sends

signals to the following: (a) the high voltage switch to apply and remove the bias voltage, (b) the amplifier system to turn on and off the protection circuitry, (c) the laser to fire, and (d) the oscilloscope to synchronize the oscilloscope with the laser. This trigger system is controlled using a PCI-CTR05 counter board which is installed in the PCI bus of a Lenovo computer (PC) running Windows XP. The operator of the system is able to control the timing of the experiment using LabView, a custom graphical user interface (GUI) on the PC. A Tektronix TDS210 digital oscilloscope captures the transient waveforms and, through a GPIB interface, uploads the digitized signal to the LabView program on the PC for analysis and storage.

A schematic of the entire system used is shown in Figure 3.10. The original design and construction of the system was done by R. E. Johanson and various changes were made by previous graduate students within the group (e.g. [19, 20]). The system is based on a grounded bridge network to eliminate the displacement current signal in the IFTOF measurements. A high voltage open-air variable capacitor C_N can be adjusted to match the capacitance of the sample being measured. Once this is done the displacement currents will be equal in both branches of the grounded bridge network. These displacement currents are limited by placing six ultra-fast switching diodes (MUR120) across each of the bridge resistors. In the schematic shown in Figure 3.10 each diode shown (i.e. $D_1 - D_4$) contains three fast switching diodes in series. A differential amplifier is used to detect the photocurrent signal from the sample as that will be the only voltage difference between the branches of the grounded bridge network. A protection circuit is placed before the amplifier circuit which shorts the amplifier inputs during switching to protect the amplifier. This protection circuit causes a delay when the bias voltage is turned on, so that the oscilloscope measures a signal at time $t_2 + \Delta t$. The grounded bridge network does not completely eliminate the displacement currents as the dark current in the a-Se samples increases sharply with the applied field and typically decays with time. Because of this the sample is equivalent to a time and field dependant resistor in parallel with the sample capacitance, and it becomes extremely difficult to completely match the grounded bridge network branches. Therefore the bridge is adjusted to get the displacement currents down to the order of the photocurrent. Then to collect the true displacement current free photocurrent signal, two measurements are taken, the first with no excitation from the laser and the second with laser excitation. Then the PC performs digital subtraction on the two signals producing the net displacement current free photocurrent signal. The digital subtraction method has been used

before to successfully capture displacement free IFTOF photocurrent signals [19, 38, 45]. Photos of the system used are shown in Figure 3.11 and Figure 3.12.

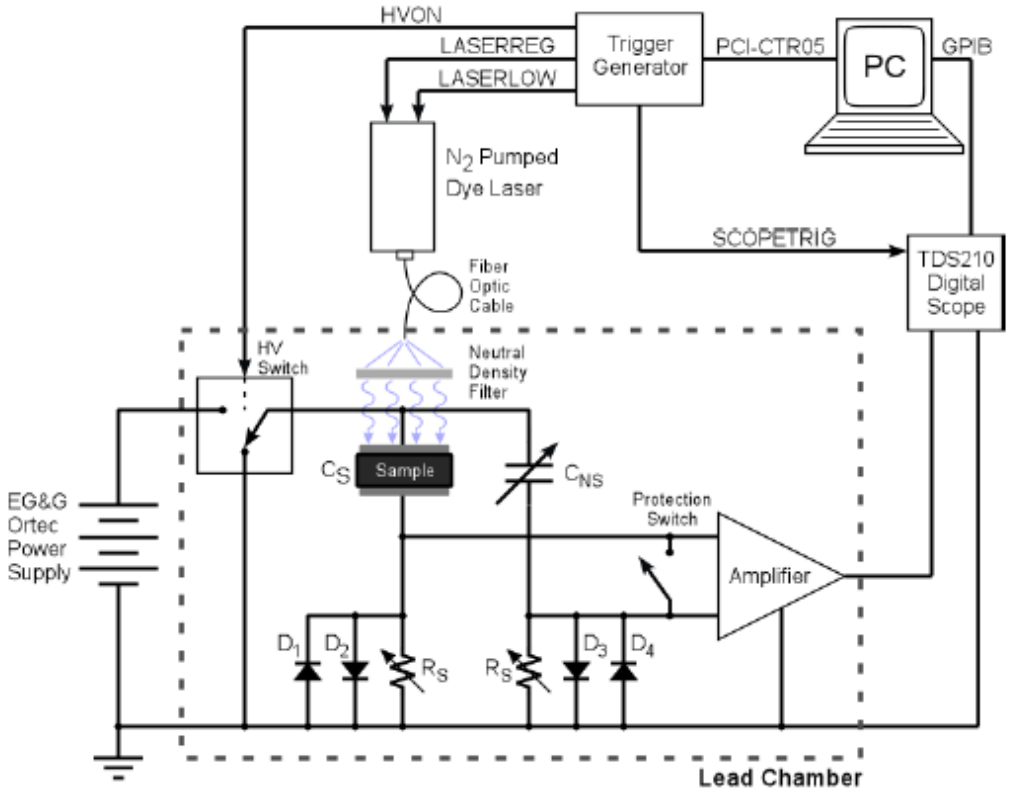

Figure 3.10: TOF/IFTOF system schematic diagram. The amplifier, high voltage switch and trigger system are shown as functional blocks. Each of the diodes D_1, D_2, D_3, and D_4 contains three fast diodes in series.

An x-ray source is required in order to measure the effects of x-ray exposure on the charge-carrier transport properties of the samples. Thus the sample holder is placed underneath the x-ray source inside a lead-lined thick-steel cabinet to protect the operator from x-ray radiation. This steel cabinet also benefits the experiments by providing a dark environment for the TOF and IFTOF experiments. A fiber optic pigtail cable is used to guide the laser excitation into the lead chamber. The HV switch, bridge network, and amplifier were also placed within the steel cabinet so that they would be physically close to the sample holder and reduce the stray capacitances between the functional blocks. The HV switch, bridge network, amplifier, and trigger generator are all placed in individual aluminum boxes with the trigger generator placed

outside the lead cabinet next to the PC. Coaxial cables are used throughout the system to guide the trigger signals, the HV bias, and the photocurrent signal.

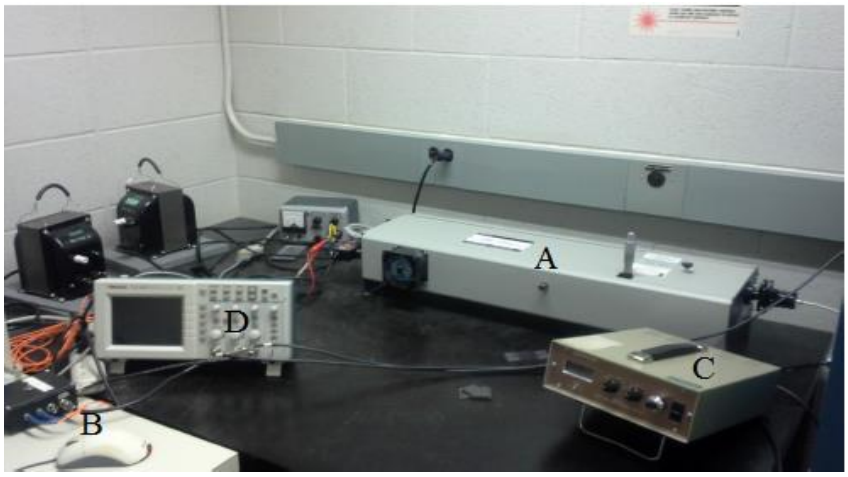

Figure 3.11: Partial experimental setup for the TOF/IFTOF system. A LN103C nitrogen UV laser (A), a 5V supplied triggering system (B), an EG&G high voltage supply (C), and a Tektronix TDS210 digital oscilloscope (D) are shown in the figure. The computer is to the left of the image.

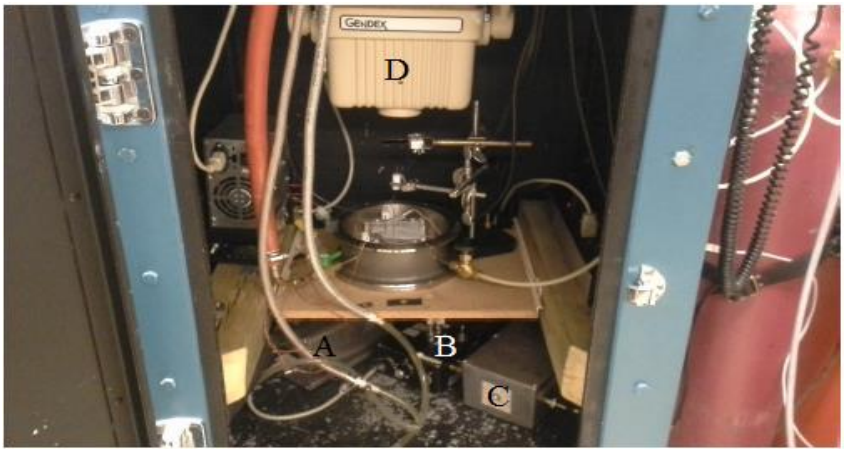

Figure 3.12: Partial Experimental setup for the TOF/IFTOF system. A high voltage switch (A), grounded bridge network (B), amplifier system (C), and the Gendex GX-1000 x-ray tube (D) are shown in the figure.

3.4.1 N_2 Laser

The excitation source used for the TOF/IFTOF experiments is a Laser Photonics LN103C nitrogen pumped dye laser, which is selected for its narrow spectrum and short pulse length. The

laser produces an output pulse with a 300 ps pulse length with a ± 2 ns jitter. The peak power of the laser is rated at 250 kW and the output pulse has a peak energy wavelength of 337.1 nm with a 0.1 nm spectral width.

The laser is triggered by two TTL level signals applied through two BNC inputs on the rear panel of the laser. A plot of the required timing sequence of these two signals is shown in Figure 3.13. First a +5 V pulse of at least 100 ns is applied to the REG input. This pulse charges the laser. Between 30 and 50 µs later a second +5 V pulse of at least 100 ns must be applied to LOW to discharge and fire the laser. If the second pulse is not applied to the LOW input, the laser will self-fire after 50 µs. As the firing of the laser utilizes a high voltage discharge through a spark gap circuit, large switching transients are produced. In order to prevent these switching transients from leaking back into the IFTOF system, the laser trigger signals are optically coupled to the laser control inputs.

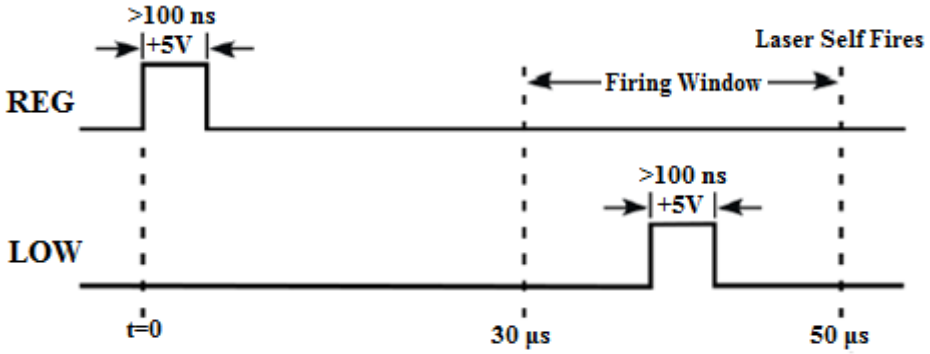

Figure 3.13: Trigger timing requirements for the LN103C nitrogen laser.

The output of the laser is fit with a Newport Optical Fiber adapter (model MM-2A) and the output light pulse is coupled to a fiber optic pigtail cable. The optical cable is then fed into the lead cabinet which contains the sample holder. In order to prevent photogeneration from occurring near the edges of the top contact on the sample, a black mask with a circular aperture is placed on top of the sample. If the output of the laser is to intense, neutral density filters may be placed between the optical cable end and the sample to ensure that the small signal conditions are satisfied.

3.4.2 High Voltage Switch

The high voltage switch utilizes two fast switching n-channel IRFBG30 HEXFETS in a totem pole configuration. A schematic of the high voltage switch is shown in Figure 3.14. The switch has a maximum switching capacity of 1 kV in order to provide the samples with a large bias voltage while performing transient photoconductivity measurements. As the transit times for holes is in the microseconds range, the switch has to have a rise and fall time on the order of 0.1 μs.

The maximum rated gate to source voltage on the HEXFET transistors is ±20 V. This voltage is provided to the gate by two HCPL3120 optocouplers, which also provide isolation of the control circuitry from the high voltage at the output. The top optocoupler is supplied by a floating +18 V power supply connected between A and B. The bottom optocoupler is supplied by a grounded +18 V power supply. The optocouplers in the system work very well at sourcing the gate voltage for the HEXFETs, but are not able to sink the voltage as quickly. Therefore the bipolar junction transistors (BJTs) (Q_1–Q_4) are placed in the system to help turn off the HEXFETS. As either HEXFET begins to shut off, current is passed through the base of the BJTs, which provide a short between the gate and the source of the HEXFETs.

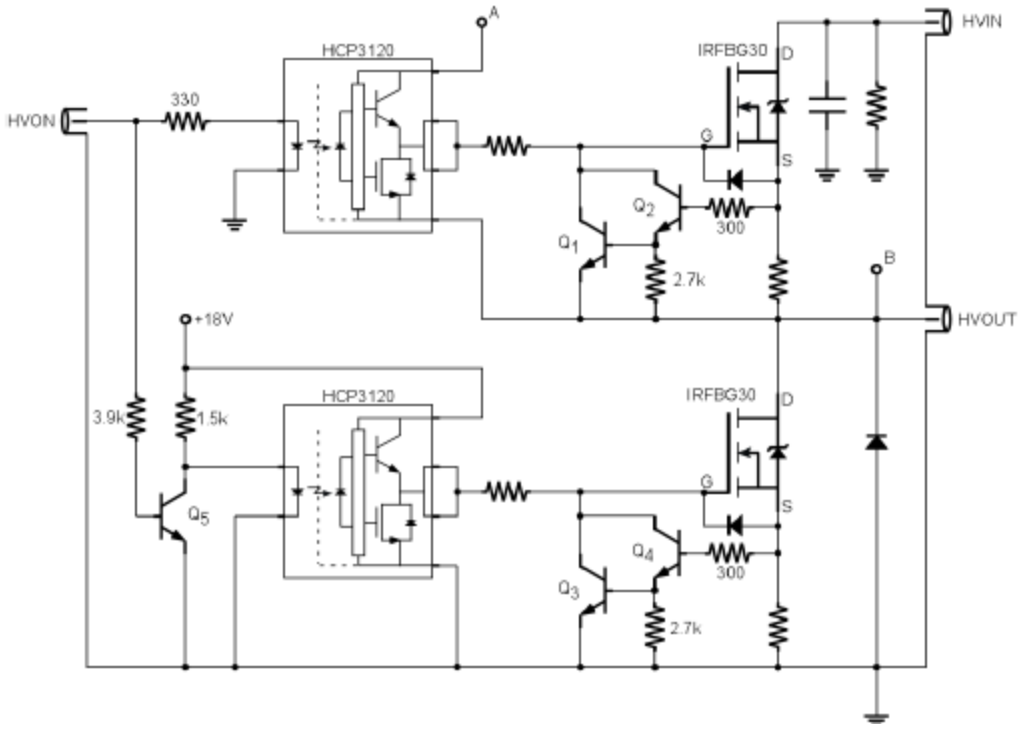

Figure 3.14: A 1kV fast switching high voltage HEXFET switch.

The bias voltage is provided by an EG&G Ortec 556 high voltage power supply, which is connected to the HVIN input of the HV switch. The output of the HV switch (HVOUT) is connected to the top contact of a sample. When there is no signal to the trigger input, HVON, Q_5 is turned off and the grounded +18 V power supply is passed through the bottom optocoupler to the bottom HEXFET, providing a path from HVOUT to ground and isolating HVIN. When there is a +5 V signal at the trigger input, HVON, Q_5 will turn on and short the grounded +18 V power supply. This in turn shuts off the bottom optocoupler as well as the bottom HEXFET. At the same time, the top optocoupler is turned on, passing the floating +18V power supply to the gate of the top HEXFET. This turns on the top HEXFET providing a direct connection between HVOUT and HVIN for the duration of the pulse at HVON. This HV switch functions as a single-pole double-throw switch with the output normally connected to ground. Only a positive voltage at the HV input will work with this switch. Therefore, in order to get a negative polarity over the sample, the output must be connected to the substrate of the sample and the top of the sample must be connected to the sampling resistor.

3.4.3 Amplifier System

The amplifier system used to amplify the photocurrent signal that is induced across the sampling resistor is a 2-stage, wide bandwidth differential amplifier. A schematic of the amplifier is shown in Figure 3.15. The first stage of the amplifier system consists of a wide bandwidth, high CMRR video amplifier (AD830) configured to have unity gain. The unity gain bandwidth of this amplifier is 85 MHz and the CMRR is 60 dB at 4 MHz. The second stage of the amplifier system uses a high speed amplifier (AD827) in a non-inverting configuration with a gain of 16 dB. This high speed amplifier serves to raise the photocurrent signal above the noise floor of the oscilloscope and drive the large capacitances that arise from the coaxial cable connecting the output of the amplifier system to the oscilloscope.

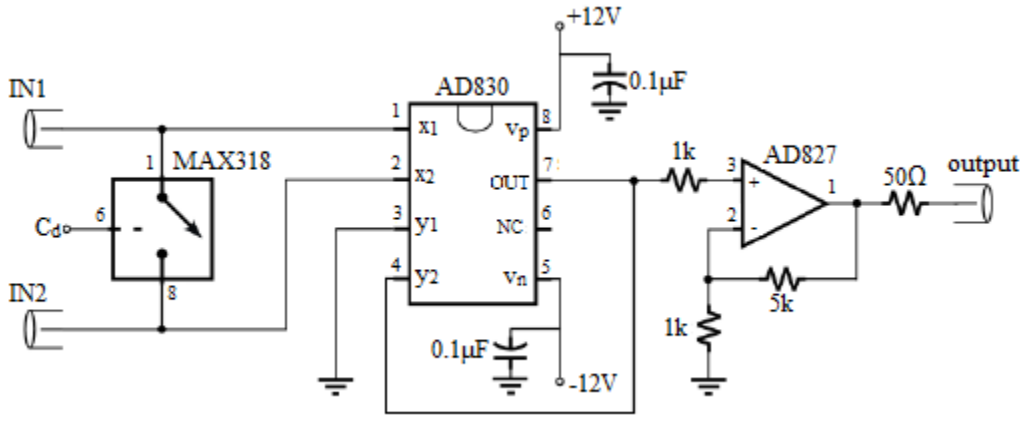

Figure 3.15: A two-stage wide bandwidth difference amplifier with 16 dB gain.

In order to protect the amplifier system from the high voltage switching transients, a precision, normally open, CMOS analog single-pole single-throw switch (MAX318) is placed across the inputs of the differential amplifier. The MAX318 is controlled by a trigger pulse generated by a monostable multivibrator (LS123) and a positive-edge-clocked D flip-flop. The schematic for the MAX318 control circuitry is shown in Figure 3.16 (a). The timing of the signals when the input signal (HVON) is changed is shown in Figure 3.16 (b).

When the signal at HVON goes low, the signal to the MAX318 goes high, shorting the input terminals to the amplifier system. When the signal at HVON goes high, there is a time delay t_s before the signal to the MAX318 goes low and allows the amplifier system to pass the

photocurrent signal. The time delay can be adjusted by changing the resistance in the resistor-capacitor network connected to the monostable multivibrator.

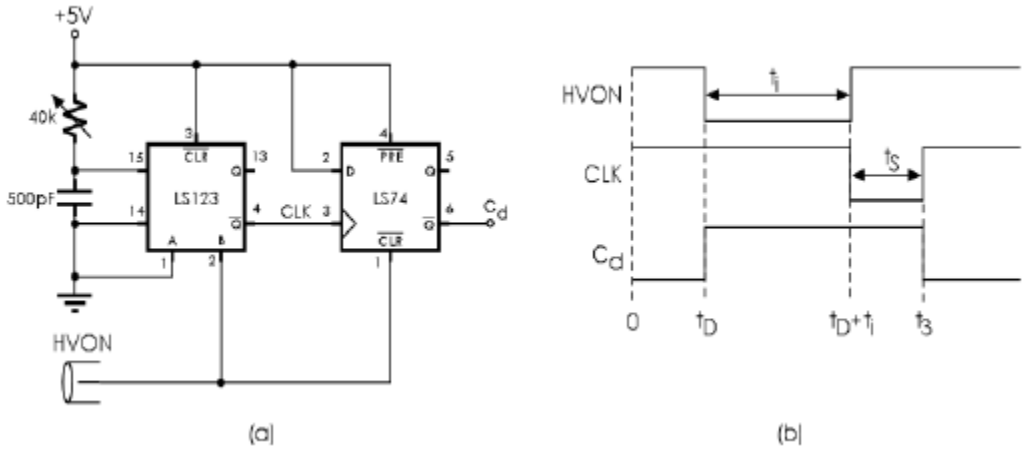

Figure 3.16: The schematic of the system used to send the trigger signal to the MAX318 (a). The timing diagram for the signals (b).

The small signal bandwidth of the amplifier system can be estimated by placing a square pulse at the input and measuring the rise time at the output. This was performed by Fogal [19] and it was found this system has a small signal bandwidth of around 12 MHz. As the transit times of any transient photoconductive experiment performed is expected to be much longer than 1 μs, this amplifier system is suitable for carrying out the TOF and IFTOF measurements on the a-Se samples.

3.4.4 Trigger System

The trigger system generates the signals to fire the light source, to switch the HV switch, to activate the protection in the amplifier system, and to trigger the oscilloscope. The signals are generated using a PCI-CTR05 counter board installed in the PCI bus of a PC. The board uses an AMD9513 counter/timer chip that contains 16 bit up/down counters. At a high level the board is controlled by the Computer Boards Universal Library of programming functions. The trigger generator code is written in C++ and a LabView GUI is used to call the C++ functions. Figure 3.17 shows the circuit used to interface the output of the counter board with the laser TOF/IFTOF system.

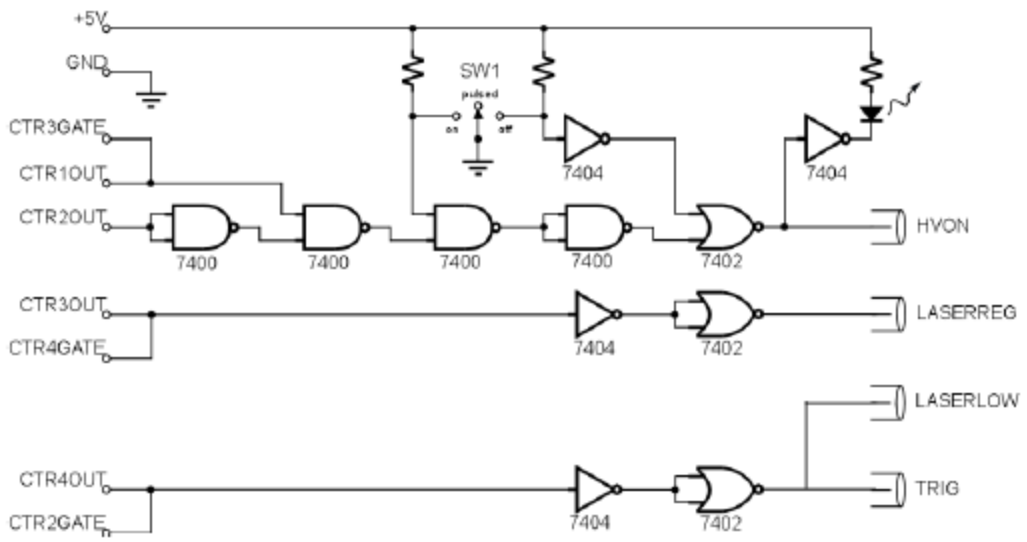

Figure 3.17: The PCI-CTR05 interface circuit for generating the trigger signals for the laser TOF/IFTOF system.

The interface circuit is contained in an aluminum case outside of the lead chamber. The control signals are sent from the output of the counter board to the input of the interface circuit through a ribbon cable and a 39-pin D-sub connector. The power bus from the PC powers the logic gates in the interface circuit. The state of the HV switch can be manually controlled using a switch on top of the aluminum case containing the trigger generator circuit, to select one of three settings; on, pulsed, and off. The on position applies the bias voltage to the sample, the off position removes the bias voltage to the sample, and the pulsed position allows the counter board to control the HV switch. Under normal operation the switch is set to the pulsed position. A LED on top of the trigger generator box provides visual feedback on the state of the HV switch.

The timing of the counter board output and the resulting outputs of the interface circuit for the laser TOF/IFTOF system is shown in Figure 3.18. The HVON output is connected to the HV switch and the amplifier circuit to pass the bias voltage to the sample and to activate the protection circuitry. This signal is controlled by the input signals CTR1OUT and CTR2OUT. When a signal is applied to CTR1OUT, HVON goes high, the HV switch is turned on and the bias voltage is applied to the sample. This signal is applied during the entire TOF or IFTOF experiment. Application of a signal to CTR2OUT turns the HVON signal to low, turning off the HV switch and is used to apply the interruption in the IFTOF experiment. The delay of t_{HV1} is

present to allow the high voltage switching transients to settle before firing the laser. The delay times t_D and t_i are controlled by the operator on the LabView GUI during the IFTOF experiment. The delay of t_D determines the amount of time until the bias voltage is interrupted. The delay of t_i determines the amount of time the bias voltage is interrupted. The 100 ns pulse on LASERREG starts the charging of the laser and is controlled by the input at CTR3OUT. The 100 ns pulse on LASERLOW, controlled by the input at CTR4OUT, fires the laser signaling the beginning of the IFTOF experiment. The SCOPETRIG signal, also controlled by the input at CTR4OUT, triggers the oscilloscope to capture the resulting photocurrent pulse through the sample.

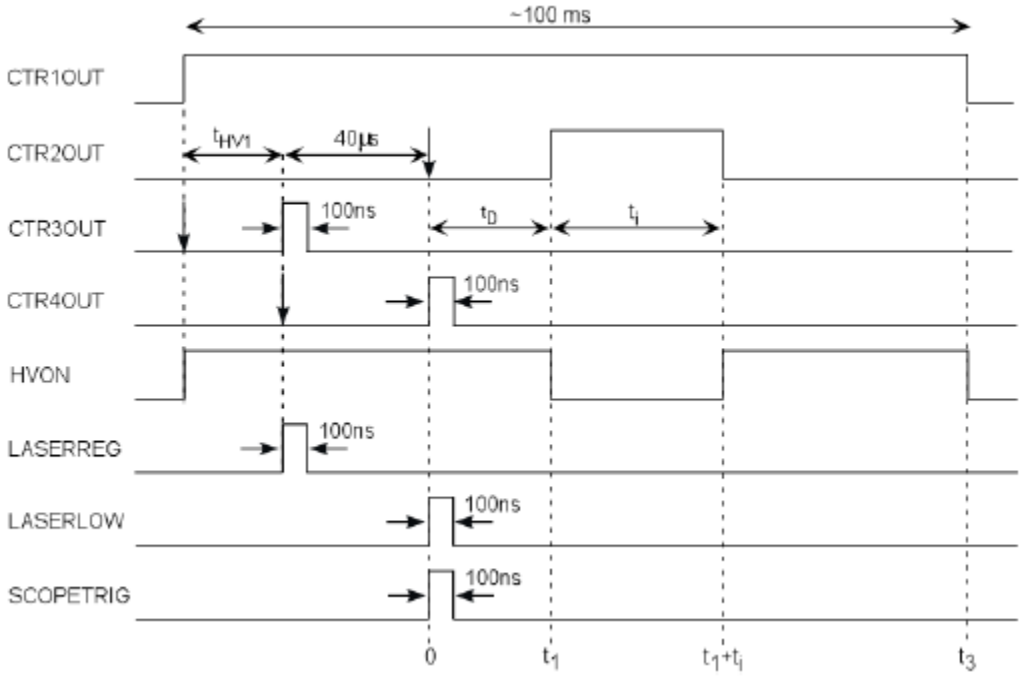

Figure 3.18: The timing signals from the PCI-CTR05 counter board and the interface circuit in the laser TOF/IFTOF system. The variables t_D and t_i are set by the operator.

3.4.5 Control and Data Acquisition System

The photocurrent generated during a TOF or IFTOF experiment is captured using an 8-bit Tektronix TDS210 digital oscilloscope with a sampling rate of 1 Gb/s. The output of the amplifier circuit is connected to channel 1 of the oscilloscope. The EXT TRIG input to the oscilloscope is connected to the SCOPETRIG output of the trigger generator circuit. The trigger of the oscilloscope is set to EXT and the level was set at 3 V. The vertical and horizontal settings on the oscilloscope are adjusted for each experiment to capture a full photocurrent signal. To

limit the amount of noise in the captured signal it is possible to limit the bandwidth of the oscilloscope to 20 MHz, otherwise the bandwidth is 60 MHz. The oscilloscope is interfaced with the PC through a GPIB connection. A GUI realized through LabView was created on the PC to control the timing signals of the experiments, communicate with the oscilloscope, and display the captured signal on the PC to the operator. Under the oscilloscope tab the settings of the oscilloscope can be controlled. Under the Experiment tab, the operator can select to perform a TOF or an IFTOF experiment. The Laser Trigger Delay is set to synchronize the oscilloscope with the firing of the laser. The Delay Time and the Interruption Time can be set by the operator to determine when the interruption of the bias voltage occurs and for how long the interruption occurs respectively, in the IFTOF experiment. The TRIGGER button is used to perform a TOF/IFTOF experiment and capture it on the oscilloscope. Under Sampling Conditioning, the light source will be pulsed the specified amount of times without turning on the bias voltage. The READ button under Read Waveform reads the waveform displayed on the oscilloscope and displays it under Waveform Graph. The CAPTURE button under Capture Waveform performs a TOF/IFTOF experiment, reads the captured photocurrent pulse on the oscilloscope and displays the captured photocurrent pulse under Waveform Graph. If Baseline Subtract is set to ON the experiment will be performed and recorded to the PC twice, once with no excitation from the light source and once with photoexcitation. The two recorded photocurrents will then be digitally subtracted from one another and the resulting photocurrent is displayed under Waveform Graph. Under Save Current Waveform the operator can save the photocurrent that is displayed in Waveform Graph in text.txt form to the PC. Finally under Mobility and Lifetime Calculators the carrier drift mobility or carrier lifetime can be calculated when the cursors are placed in the appropriate places. In a TOF experiment, the first cursor should be placed at the leading edge of the TOF photocurrent pulse and the second cursor at the halfway point on the back edge of the TOF photocurrent pulse. In an IFTOF experiment, the first cursor should be placed at the height of the photocurrent signal just before the interruption and the second cursor at the height of the photocurrent signal after the interruption.

3.5 X-ray System

The x-ray source used in this investigation is a Gendex GX-1000 dental x-ray system. This system consists of an x-ray tube head and a separate control unit. The tube head is installed

inside of the steel cabinet, to protect the operator from the x-ray radiation, directly above the sample holder of the laser TOF/IFTOF system and the control unit is mounted on the side of the steel cabinet. The tube head and the control unit are shown in Figure 3.12 and Figure 3.19 respectively. The lead lined steel cabinet (A9002-16) was manufactured by X-ray Product Corp of Pico Rivera, California and is shown in Figure 3.19.

Figure 3.19: Gendex GX-1000 x-ray system and lead lined steel cabinet

The interior of the lead lined steel cabinet is accessed through a door on the front. The door is fitted with a magnetic disable switch to prevent the x-ray tube from being triggered with an open door. A red light above the door provides a visual warning when the x-ray system is turned on. A specially designed maze located in the top of the cabinet provides a route for electrical and optical cables to be pulled into the cabinet.

The tube head contains a tungsten anode and a hot filament cathode to release electrons. The filament current can be set to either 10 mA or 15 mA. The electrons are accelerated by a large electric field and impact the anode target at high velocity to produce a wide spectrum of x-

ray radiation and also heat. The tube voltage can be varied from 50-100 kVp. The tube head is encased in an oil-filled enclosure to help dissipate the heat from the target. The tube head contains an inherent 2.5 mm aluminum filter. Due to the half-wave rectifying nature of the tube head, and the 60 Hz power supply, the x-ray beam consists of a series of pulses that are $1/60^{th}$ of a second long. The total duration of the beam can be varied by the operator to produce an impulse train of 3 to 300 impulses (3/60 seconds to 5 seconds long). As the target of the tube head heats up while the tube produces x-rays, there is a limit of how much the tube can be used before damaging the tube head. The maximum working cycle of the x-ray tube within a 5 minute interval is shown in Table 3.1.

Table 3.1: Working cycle of the x-ray tube [48]

kVp	**Exposure-seconds in a 5 minute interval (s)**	
	10 mA	**15 mA**
50-70	30	20
80	26	17.5
90	23	15.5
100	21	N/A

The x-rays produced from the impact of high velocity electrons on the anode target are in the form of Bremsstrahlung radiation and characteristic radiation. Bremsstrahlung radiation is produced when the high velocity electrons are deflected by an atom. The electron undergoes deceleration and must follow the law of conservation of energy. Thus the electron releases energy in the form of x-ray radiation which can have a photon energy from the kinetic energy of the electron, determined by the tube voltage, to the lowest end of the x-ray spectrum. The characteristic radiation is produced when displaced electrons (those knocked out from an inner shell to an empty higher energy level or the conduction band) in atoms in the anode target are replaced with electrons from higher energy levels. The displacement of the low level electron occurs from the collision of an accelerated electron. This radiation produces x-rays that are determined by the energy levels of the target material. A typical x-ray spectrum of a medical x-ray tube is shown in Figure 3.20. The continuous spectrum is due to (a) the nature of Bremsstrahlung radiation as each electron will be decelerated by different amounts depending on

how near the atoms of the target they impinge, (b) the continuously changing tube voltage due to the ac power source providing differing kinetic energies to the electrons, and (c) the depth of generation in the target [5].

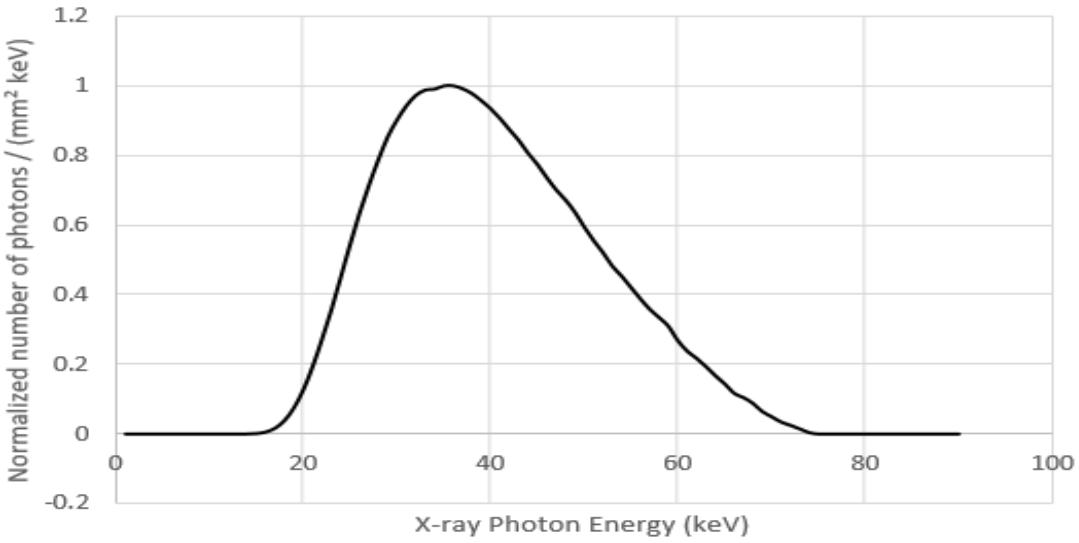

Figure 3.20: A typical x-ray spectrum at 75 kVp coming from a tungsten x-ray tube. The spectrum was obtained using SPEKTR 3.1 [49]

When an x-ray photon is incident on matter, it interacts with the matter at the individual atom level by one of the following mechanisms: elastic (Rayleigh) scattering, inelastic (Compton) scattering, the photoelectric effect, pair production attenuation, and triplet attenuation. In elastic scattering, the x-ray is simply scattered by an atom and leaves no energy within the material. Inelastic scattering occurs when part of the energy is absorbed when the x-ray is scattered by an atom. The photoelectric effect occurs when an x-ray photon knocks an electron out of the inner shell of an atom, passing all the x-ray energy to the photoejected electron and producing an electron-hole pair. Pair production attenuation occurs when the x-ray interacts with the electric field of a nucleus producing a positron and a neutron. Triplet attenuation occurs when an x-ray interacts with the electric field surrounding an orbital electron producing an ejected electron and an electron/positron pair. As a-Se has a high atomic number the main mechanism that occurs is the photoelectric effect [5, 50].

3.5.1 Dose Calculation

The effects of x-ray exposure in a-Se films are measured as a function of the absorbed dose in the sample, which has a unit of Grays (Gy). Dose is defined as the energy per unit mass absorbed by a sample and is measured in joules per kilogram (J/kg). In order to calculate the absorbed dose in an a-Se sample, the energy deposited into the sample must first be calculated. The total deposited energy follows mass attenuation as well as energy attenuation. In other words, the x-ray photon energy deposited into the sample depends on both the distance into the sample as well as the photon energy. The following dose calculation used in this work follows that described by Walornyj [20].

Looking first at linear mass attenuation, the infinitesimal loss in intensity of x-ray radiation crossing a small section of matter of width dx is given by:

$$dI(x) = -I(x)\rho\mu_m dx \tag{3.3}$$

where x is the distance into the sample measured from the irradiated surface, $dI(x)$ is the infinitesimal change in the intensity at x, $I(x)$ is the intensity at x, ρ is the density of the medium, μ_m is the mass attenuation coefficient (defined as the attenuation coefficient divided by the density), and dx is the infinitesimal change in x.

By integrating from the surface, the x-ray intensity at x is:

$$I(x) = I_o \exp(-\rho\mu_m x) \tag{3.4}$$

where I_o is the incident x-ray intensity.

Next we look at the energy attenuation. The available energy for energy attenuation from a photon energy E_p at position x is given by:

$$E(E_p, x) = E_p \frac{I(x)}{I_o} A\Phi(E_p) \tag{3.5}$$

where $\Phi(E_p)$ is the photon fluence (number of photons with an energy E_p per unit area) with a dependence on the photon energy E_p as shown in Figure 3.20, A is the surface area, and $I(x)/I_o$ is the fraction of non-mass attenuated photons at x which are available for energy attenuation.

Energy attenuation is also linear and is given by:

$$dE = E(E_p, x)\rho\mu_e dx \tag{3.6}$$

where μ_e is the mass energy absorption coefficient.

By combining Equations 3.4, 3.5, and 3.6, the total amount of deposited energy in a sample can be found. In order to determine the energy deposited into an a-Se sample, the photon fluence at the surface of the sample must first be found. This is done by placing an ion chamber at the exact location of the selenium sample with respect to the x-ray source. Then the total deposited energy in the ion chamber must be found. This value is then used to scale the simulated photon fluence to what is actually incident on the selenium samples. With the photon fluence known at the surface of the selenium sample, the total deposited energy in the sample can be found as well as the energy deposited at specific locations within the samples.

The energy deposited into the ion chamber is given by:

$$E_{\text{deposited (Ion Chamber)}} = K \int_0^D \int_0^{kVp} \rho_{\text{air}}\mu_{e\text{air}} E_p A \Phi_{\text{ideal}}(E_p) \exp(-\mu_{m\text{air}}\rho_{\text{air}} x) dE_p dx \tag{3.7}$$

where $E_{\text{deposited (Ion Chamber)}}$ is the energy deposited into the ion chamber, E_p is the photon energy, $\mu_{m\text{air}}$ is the mass attenuation coefficient of air, $\mu_{e\text{air}}$ is the mass energy absorption coefficient of air, ρ_{air} is the density of air, D is the width of the active region of the ion chamber, A is the area of the active region of the ion chamber, $\Phi_{\text{ideal}}(E_p)$ is the simulated photon fluence incident on the ion chamber, kVp is the maximum energy in the energy spectrum and K is a scaling factor. The mass attenuation coefficient of air and the mass energy absorption coefficient of air are dependent on the photon energy and are shown in Figure 3.21.

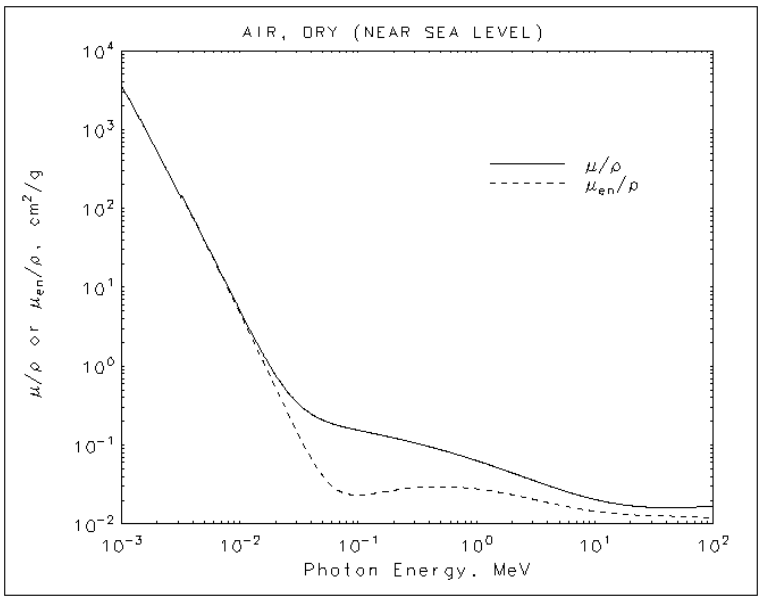

Figure 3.21: Mass attenuation coefficient and mass energy absorption coefficient of air against x-ray photon energy. Taken from the NIST website [51]

The dose that is absorbed by the ion chamber is then calculated by dividing the deposited energy by the mass of air within the ion chamber. This is given by:

$$D_{\text{absorbed (Ion Chamber)}} = \frac{E_{\text{deposited (Ion Chamber)}}}{AD\rho_{\text{air}}} \tag{3.8}$$

By measuring the absorbed dose in the ion chamber and setting Equation 3.8 to that value, the scaling factor, K, can be found. This scaling factor is used to find the actual photon fluence incident on the a-Se sample, and is found by:

$$\Phi_{\text{measured}}(E_p) = K\Phi_{\text{ideal}}(E_p) \tag{3.9}$$

Knowing the photon fluence at the surface of an a-Se sample, the energy deposited, as well as the absorbed dose, within the whole sample or within a small section of interest can be found. This is given by:

$$E_{\text{deposited (Se Sample)}} = \int_{x_1}^{x_2}\int_{0}^{kVp} \rho_{\text{Se}}\mu_{e\text{Se}}E_p A_{\text{Se}}\Phi_{\text{measured}}(E_p)\exp(-\mu_{m\text{Se}}\rho_{\text{Se}}x)dE_p dx \tag{3.10}$$

Where $\mu_{m\text{Se}}$ is the mass attenuation coefficient of selenium, $\mu_{e\text{Se}}$ is the mass energy absorption coefficient of selenium, ρ_{Se} is the density of selenium, $x_2 - x_1$ is the width of interest within the a-Se sample, and A_{Se} is the area of the a-Se sample. The mass attenuation coefficient

of selenium and the mass energy absorption coefficient of selenium are dependent on the photon energy and are shown in Figure 3.22.

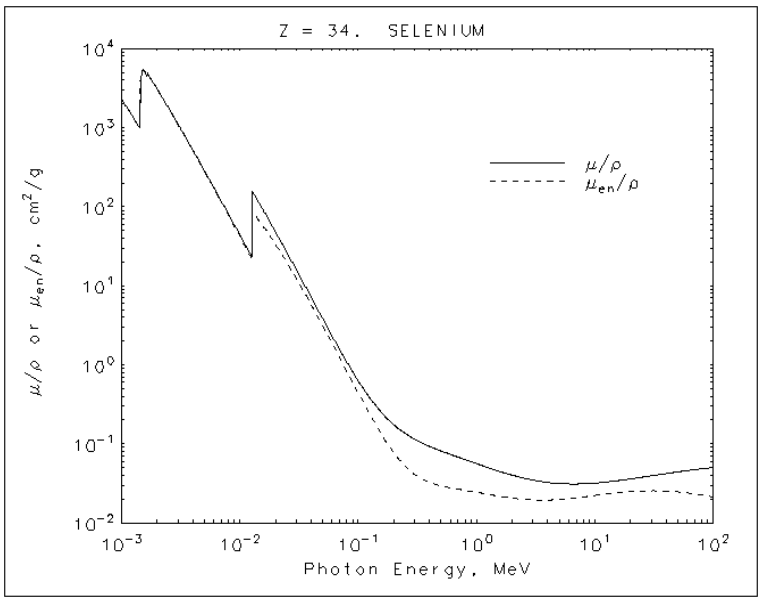

Figure 3.22: Mass attenuation coefficient and mass energy absorption coefficient of selenium against x-ray photon energy. Taken from the NIST website [51]

The absorbed dose in the a-Se sample then is then given by:

$$D_{\text{absorbed (Se Sample)}} = \frac{E_{\text{deposited (Se Sample)}}}{A_{\text{Se}}(x_2 - x_1)\rho_{\text{Se}}} \tag{3.11}$$

To get the dose that is absorbed across the whole sample thickness, x_1 should be set to zero and x_2 should be set to the width of the sample. In order to obtain the absorbed dose at a specific depth within the sample, x_1 should be set an infinitesimal amount below the desired depth and x_2 should be set an infinitesimal amount above. That is, to find the absorbed dose at location x, set $x_1 = x - dx < x < x + dx = x_2$ where $dx \ll x$.

A Keithley 35050 Ion Chamber along with a Keithley 35050 Dosimeter measures the actual x-ray exposure, in the units of Rontgens (R), which quantifies exposure to ionizing radiation such that 1 R of x-ray exposure produces ions resulting in a charge of 0.000258 C/Kg in air under standard conditions. The ion chamber is 1.22 cm thick and the volume is 15 cm^3. The total measured x-ray exposure depends on the filament current mA and tube head voltage kVp settings of the control unit, the distance from the x-ray tube head, the amount of filtration,

and the duration of the x-ray beam. By attaching a digital voltmeter to the dosimeter, the x-ray exposure in Rontgens is measured (1V = 1R). The relation of the x-ray exposure to the absorbed dose in the ion chamber is 1R = 0.00877 Gy. A custom excel sheet was created to calculate the amount of absorbed dose in a specific region of the sample following the method shown above. The user must give the readout of the x-ray exposure into the ion chamber, the kVp of the x-ray beam, and depth at which the absorbed dose is required. A snapshot of the excel sheet is shown in the Appendix.

3.6 X-ray Induced Carrier-Trapping Lifetime Change Experimental Procedure

The accumulated dose measurements investigate the changes in the carrier-trapping times due to x-ray exposure. The sample is placed on the sample holder underneath the x-ray tube head and connected to the laser TOF/IFTOF system. Before the experiment begins, the unexposed (resting) lifetime is measured. This is the lifetime in a sample that has been rested in the dark for a sufficiently long duration so that the lifetime is the equilibrium lifetime at the given temperature. Then at time $t = 0$, when the sample is under the desired applied electric field, the sample is irradiated from the x-ray tube for the desired time in order to reach a desired amount of absorbed dose in a specified region of the sample. Note that in the no field case, the bias voltage is set to 0 V. After 15 seconds, the electric field is removed from the sample. After another 15 seconds an IFTOF measurement is performed and the charge-carrier lifetime is recorded. 15 seconds later the electric field is reapplied and at time $t = 1$ min the process is repeated. The entire process is repeated every minute until the desired total accumulated dose absorbed in the sample is reached. A diagram of the experimental schedule is shown in Figure 3.23.

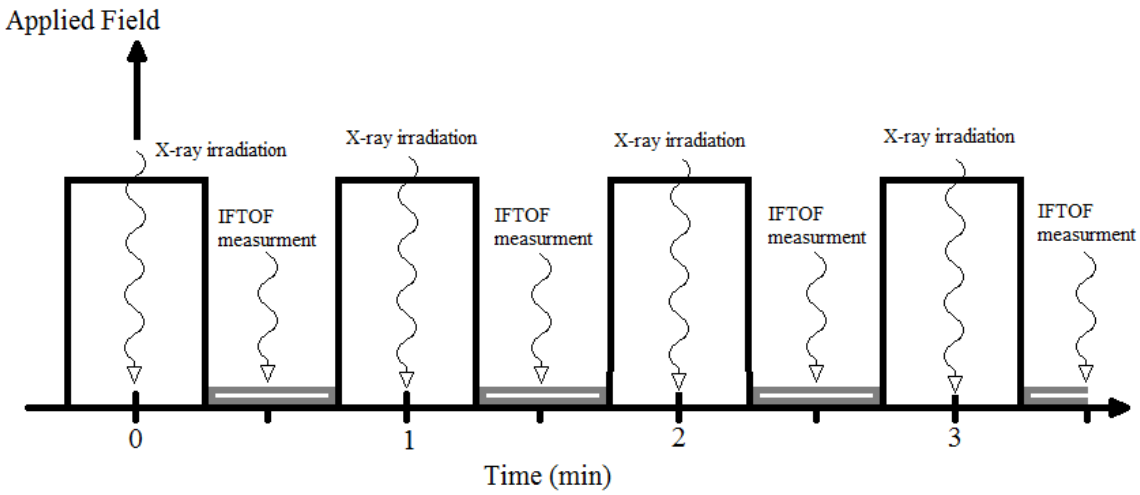

Figure 3.23: Procedure for the accumulated dose under applied field measurements. During x-ray exposure the sample is placed under an electric field. Then the electric field is removed from the sample to perform an IFTOF measurement.

Due to the nature of defects generated by x-ray radiation in a-Se, the charge-carrier lifetime may recover a little during the time interval (one minute) between the x-ray exposures. However as discovered by Yang [21], the changes in the carrier-trapping lifetime due to the relaxation process at room temperature over 1 minute is negligible compared to the x-ray induced changes. Therefore the total accumulated dose is simply the sum of the absorbed dose during each exposure.

3.7 Summary

In this chapter the experimental procedures that were used in this investigation were described. The amorphous selenium samples, alloyed with arsenic and doped with chlorine, where prepared using conventional vacuum deposition techniques on an aluminum or ITO substrates. A semitransparent gold contact was placed on top of the samples by DC sputtering. The TOF experiment produces a charge sheet, which drifts across the sample and induces an external photocurrent signal. This photocurrent is recorded and the drift mobility of the sample is found by examining the transient waveform. In the IFTOF experiment the drift of the charge-carriers is interrupted for a time allowing charges to interact with deep traps in the sample. The carrier deep trapping lifetime is then measured by examining the ratio of the magnitude of the photocurrent signal before and after the interruption. Interruption is performed by removing and

reapplying the bias voltage on the sample, which gives rise to large displacement currents, which can dwarf the IFTOF signal. To eliminate the displacement current signal a grounded bridge network is used, and high-speed diodes are used to limit the magnitude of this signal. A differential amplifier is used to extract the photocurrent signal. A detailed description of the TOF/IFTOF systems used in these experiments was given along with experimental procedures. The x-ray source used to irradiate samples was presented along with a detailed explanation of the calculation to find the dose absorbed in a sample. Finally the experimental procedure for measuring the x-ray induced effects in a-Se is given.

4. X-Ray Induced Effects in Stabilized a-Se in the Absence of an Applied Field

In-Part Manuscript Version of Journal of Applied Physics, 127, 084502, 2020

4.1 Introduction

The goal of the research in this chapter is to examine the x-ray induced effects on the charge-carrier transport properties in stabilized amorphous selenium in the absence of an applied electric field. The results in this section were measured using the TOF and IFTOF experiments described in previous chapters. The TOF technique is used to measure the charge-carrier drift mobility, and the IFTOF technique is used to find the charge-carrier lifetime. All measurements performed in this section were done in the absence of an applied field. Samples were allowed to rest and TOF and IFTOF measurements were taken to get the drift mobility and lifetime of both electrons and holes in a sample that has rested and returned to equilibrium. Then the sample is exposed to x-ray radiation under no applied electric field and the charge-carrier drift mobility and lifetime are measured again. The effects of x-ray radiation is measured as a function of absorbed dose in the a-Se samples. This is repeated for multiple samples which have differing resting lifetimes, at different dose rates and at different x-ray photon energies. To evaluate the effect of x-ray induced changes in the transport properties, the effect on the charge collection efficiency and thus the x-ray sensitivity is examined. This work has recently been published in the Journal of Applied Physics [52]. The results and discussion of this chapter are extracted from the relevant parts of this paper, that is, the work performed in the course of this investigation that were included in this paper. The additional work in the paper, measurements under low and high temperatures, as well as recovery measurements were performed by the other authors and will not be included.

4.2. Results

Previous work has shown that x-ray irradiation does not have any effect on the electron or the hole drift mobility [20, 21]. In this work, there are also no observed measurable changes in the hole transit time after the cessation of x-ray irradiation. Thus, the hole drift mobility remains unaffected. There is therefore no measurable effect on the concentration of shallow traps that

control the transport of photoinjected holes and electrons. However, there are major changes in the carrier lifetimes.

Figure 4.1 shows a typical result in which the normalized hole lifetime τ_h after exposure, normalized to the hole lifetime before exposure τ_{ho}, that is τ_h/τ_{ho}, plotted against the accumulated absorbed dose D in a-Se at an absorbed dose rate of 1.75 Gy/s. The reciprocal normalized lifetime τ_{ho}/τ_h is also plotted. Similarly, Figure 4.1 also shows the plots for the electron lifetime against the absorbed dose, that is, τ_e/τ_{eo} and τ_{eo}/τ_e vs. absorbed dose. The solid lines on the reciprocal lifetime vs. dose data are the best curve fits based on representing the absorbed dose dependence of the hole lifetime by:

$$\frac{\tau_{ho}}{\tau_h} = 1 + A_h D \tag{4.1}$$

where A_h is a constant. There will be a similar expression for the normalized reciprocal electron lifetime, $\tau_{eo}/\tau_e = 1 + A_e D$. As apparent from Figure 4.1, Equation 4.1 can describe both the hole and the electron lifetime dependence on the absorbed dose. Do A_h and A_e depend on the dose rate $\dot{D}$, photon energy E_{ph} and the lifetimes τ_{ho} and τ_{eo}? The next set of experimental results needs a short discussion on the physics involved in the lifetime reduction.

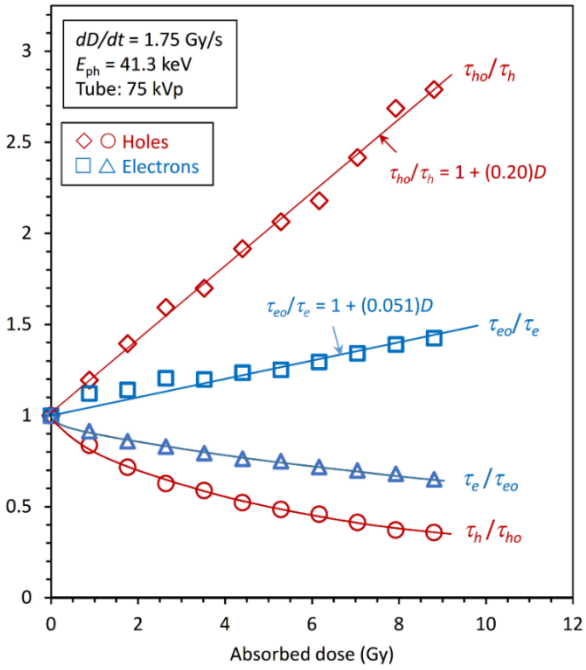

Figure 4.1: The normalized hole lifetime τ_h/τ_{ho} and its reciprocal τ_{ho}/τ_h plotted against the accumulated absorbed dose D at a dose rate of 1.75 Gy/s. Similarly, the normalized electron lifetime τ_e/τ_{eo} and its reciprocal τ_{eo}/τ_e plotted against D at the same dose rate of 1.75 Gy/s. The normalization is with respect to the lifetime before any x-ray irradiation. The solid lines are best fits of Equation 4.1 with A = 0.204 Gy^{-1} for holes (Adjusted R^2 = 0.9996) and A = 0.0504 Gy^{-1} for electrons (Adjusted R^2 = 0.9989) (Best curve fits obtained on Origin.)

Consider the reduction in the hole lifetime with dose. The probability of trapping per unit time after irradiation can be described by the capture of holes into intrinsic deep traps already present in the sample, capture by trapped electrons (effective recombination), capture into x-ray generated defects, etc., that is

$$\frac{1}{\tau_h} = \theta_h C_{th} N_{th} + C_r n_t + \theta_h C_{xh} N_{xh} \tag{4.2}$$

where it is assumed that the hole drift is controlled by shallow traps, θ_h is the hole mobility reduction factor (= effective drift mobility / band mobility), $\theta_h C_{th} N_{th}$ is the reciprocal intrinsic hole lifetime ($1/\tau_{ho}$), i.e. the mean capture probability per unit time into intrinsic deep traps with a concentration N_{th} and a capture coefficient C_{th}, C_r is the recombination coefficient of drifting holes with trapped electrons whose concentration is n_t, and N_{xh} is the concentrations of one

particular species of defects (hole traps) that has been generated (there may be more species) whose capture coefficient is C_{xh}. n_t in Equation 4.2 would be due to the trapping of x-ray generated electrons, and is discussed in Section 4.3.1. Normalizing Equation 4.2 and setting it equal to Equation 4.1 for comparison, we have,

$$\frac{\tau_{ho}}{\tau_h} = 1 + \frac{C_r n_t}{\theta_h C_{th} N_{th}} + \frac{C_{xh} N_{xh}}{C_{th} N_{th}} = 1 + A_h D \tag{4.3}$$

This equation is further developed in Section 4.3.1 to delineate the full physics involved. Equation 4.3 would be valid if we assume that n_t and N_{xh} are proportional to the absorbed dose D, which will always be the case for sufficiently small dose. The A-coefficient, according to Equation 4.3 should depend on the material properties.

The next critical issue is whether the constant A_h in this equation depends on the dose rate and the x-ray photon energy or the total dose. If A_h is independent of the dose rate and the x-ray photon energy, then Equation 4.1 becomes a very useful model for describing the effect of x-ray absorption on the lifetime for both types of carriers, albeit with an A-coefficient that may depend on the material properties. Figure 4.2 shows τ_h/τ_{ho} as a function of accumulated absorbed dose D (Gy) at four different absorbed dose rates from 0.15 to 1.75 Gy/s at one photon energy for one particular sample. It can be immediately seen that, within experimental errors, we can easily draw a single curve of the type in Equation 4.1 through nearly all the points. Figure 4.3 shows A_h at different dose rates and different mean x-ray photon energies for different samples, all of electronic quality a-Se. It should be apparent from Figure 4.3 that A_h is essentially independent of the dose rate from about 0.15 to 2.5 Gy/s, more than an order of magnitude, and mean x-ray photon energies from 31.9 keV to 44.7 keV (corresponding to 50 kVp to 90 kVp tube voltage).

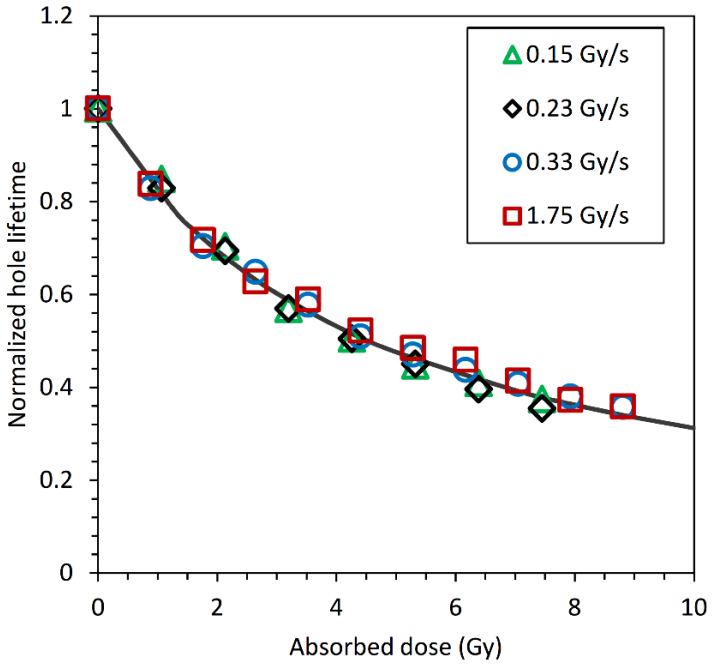

Figure 4.2: The hole lifetime after exposure that has been normalized to the lifetime before exposure as a function of accumulated absorbed dose *D* (Gy) at absorbed dose rates from 0.15 to 1.75 Gy/s for one particular sample, with $\tau_{ho} \approx 60$ μs and $\tau_{eo} \approx 462$ μs. The photon energies have a 75 keVp or a mean photon energy of 40.3 keV. The size of the experimental points represent the extent of errors.

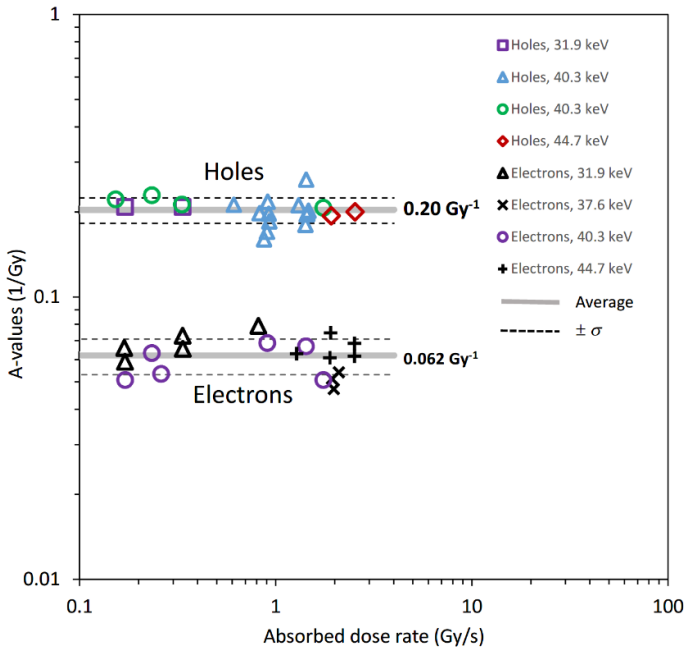

Figure 4.3: The dependence of A in Equation 4.1 on the absorbed dose rate for hole and electron lifetime reduction at room temperature (23.5 °C). The mean photon energy for A values were 31.9−44.7 keV as shown in the legend. The applied field during exposure is $F = 0$ V/μm.

Figure 4.4 is a three-dimensional scatter plot of all A_h-values against hole and electron lifetimes. It can be seen that A_h seems to be independent of both lifetimes. (Notice the χ^2-values in the caption.) One of the most important conclusions from Figure 4.3 and Figure 4.4 is that A_h seems to be independent of τ_{ho}, which is surprising since A_h in Equation 4.3 has a term $1/C_{th}N_{th}$ and hence A_h should depend on τ_{ho}. We saw no such dependence within experimental errors. In addition, we might expect n_t in Equation 4.3 should be proportional to N_{te} and hence A_h should depend on $1/\tau_{eo}$. Neither was there any dependence on τ_{eo}. Section 4.3.1 provides an interpretation and explanation of the physical origin of these results.

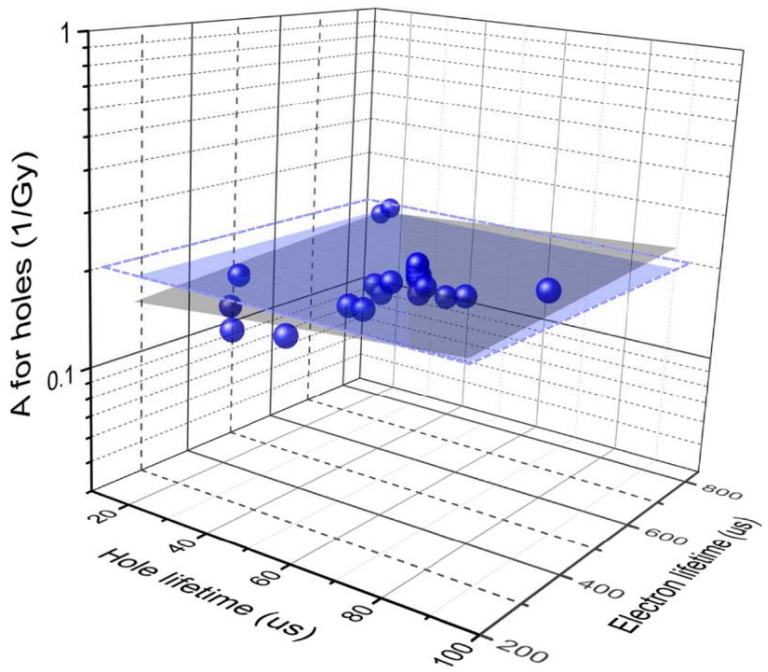

Figure 4.4: A_h for hole lifetime vs pre-exposure hole and electron lifetimes τ_{ho} and τ_{eo} (in microseconds) in a 3D scatter plot. The flat plane corresponds to $A_h = 0.205 \pm 0.0042$ 1/Gy with a reduced χ^2 value of 4.13×10^{-4}. The slightly tilted plane (gray) is the best fit plane to the data, given by $A_h = 0.151 + 0.000526\tau_{ho} + 0.000051\tau_{eo}$ and has an adjusted R^2 value of 0.381, and a reduced χ^2 value of 2.56×10^{-4}.

Figure 4.3 also shows the A_e values for the electron lifetime. There is more scatter in the A_e values for the electron lifetime than that for the hole lifetime but nonetheless the collection of data point to A_e values that are relatively independent of the dose rate. Further, over mean x-ray photon energies from 31.9 keV to 44.7 keV (corresponding to 50 kVp to 90 kVp tube voltage), the A_e values are also independent of the mean photon energy. The experimental evidence attributes the reduction in the hole and electron lifetimes to the total energy absorbed by a-Se rather than the rate at which this energy is absorbed, at least over the dose rates examined. Further, it is the total energy deposited rather than the individual photon energy that determines the reduction in the lifetimes. Table 4.1 provides a summary of *A*-values for both electrons and holes measured in this work at room temperature, along with the uncertainties.

As in the case of hole lifetime, we have also examined whether A_e exhibits any dependence of the electron and hole lifetimes in a three-dimensional plot as shown in Figure 4.5.

Given the scatter in the A_e measurements, we see no dependence on pre-exposure lifetimes – the experimental points are scattered around a flat plane. Section 4.3.1 provides an interpretation of these results. A_e is therefore independent of τ_{eo} and τ_{ho}, which means that we can model the effect of pre-exposure to x-rays on both hole and electron transport conveniently by using single value for A_h and A_e.

Table 4.1: Room temperature A values observed in this work. $\overline{\boldsymbol{A}}$ is the statistical average of all values in which the mean standard deviation is σ (uncertainty).

	$\bar{A}$ ($\pm\sigma$) (Gy^{-1})	Uncertainty (Gy^{-1})	Comment
Holes	0.203	0.021	At 23.5 °C. Dose rate = 0.15 – 2.5 Gy/s, mean x-ray energy = 31.9 keV – 44.7 keV. Does not depend on τ_{ho} and τ_{eo}
Electrons	0.0620	0.0090	At 23.5 °C. Dose rate = 0.17 – 2.5 Gy/s, mean x-ray energy = 31.9 keV – 44.7 keV. Does not depend on τ_{eo} and τ_{ho}

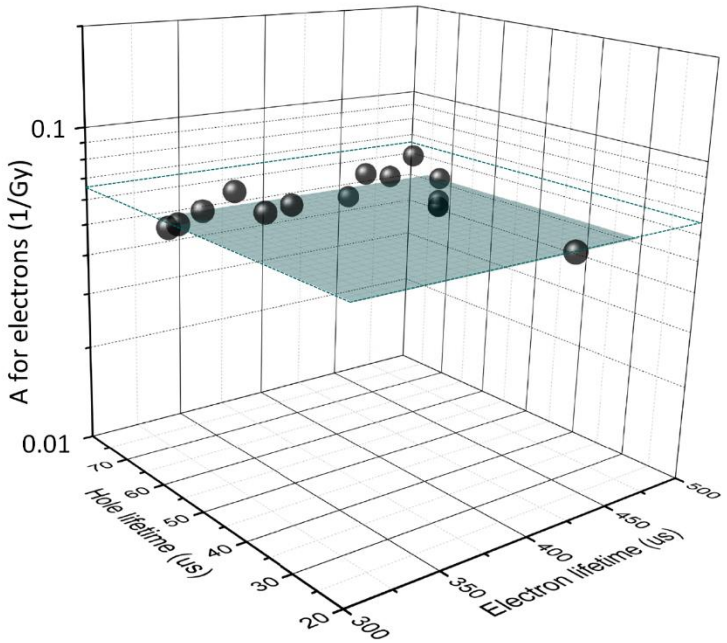

Figure 4.5: A_e for electron lifetime vs pre-exposure electron and hole lifetimes τ_{eo} and τ_{ho} (in microseconds) in a 3D scatter plot. The flat plane corresponds to A_e = 0.0630 ± 0.0019 1/Gy with a reduced χ^2 value of 5.30×10^{-5}. (Fit obtained on Origin)

In a previous study, the hole lifetime and hence $\tau_h^{-1} - \tau_{ho}^{-1}$ was examined as a function of position x_1 across an x-ray irradiated a-Se film at different x-ray energies. It was shown that the spatial variation of $\tau_h^{-1} - \tau_{ho}^{-1}$ matched the absorbed x-ray photon profile as defined by the linear attenuation coefficient corresponding to the photon energy used, i.e. $\tau_h^{-1} - \tau_{ho}^{-1}$ was found to be proportional to $\exp(-\alpha x)$, where α is the linear attenuation coefficient. Thus, the results in this work are in general agreement with the latter finding. Further, the drop in hole and electron lifetimes with absorbed dose at different temperatures were reported previously and large changes with temperature were noted [20, 21, 53].

4.3 Discussion

4.3.1 Defect Generation

One of the most interesting findings in this work is the fact that for both holes and electrons, the *A*-values for all dose rates and energies are relatively constant and, surprisingly, also independent of the carrier lifetimes; i.e. it is approximately the same for many samples examined in this work.

Consider Equation 4.3. The trapped electron concentration n_t depends on three factors: how many electrons have been photogenerated, which depends on the absorbed dose *D*, how many traps are available to trap these electrons, which depends on the intrinsic trap concentration N_{te} and the capture coefficient C_{te}. Thus, $n_t = B_1"\theta_e C_{te} N_{te} D$ where θ_e is the shallow trap mobility reduction factor for electrons (electron transport is shallow trap controlled) and $B_1"$ is a constant. Further, we can expect N_{xh} to initially increase linearly with the absorbed dose *D* with a proportionality constant $B_2"$. Thus,

$$\frac{\tau_{ho}}{\tau_h} = 1 + \frac{C_r \theta_e C_{te} N_{te} B_1"}{\theta_h C_{th} N_{th}} D + \frac{C_{xh} B_2'}{C_{th} N_{th}} D \tag{4.4}$$

and since $\tau_{eo} = (\theta_e C_{te} N_{te})^{-1}$, we have

$$\frac{\tau_{ho}}{\tau_h} - 1 = \frac{\tau_{ho}}{\tau_{eo}} B_1' D + \tau_{ho} \theta_h C_{xh} B_2' D \tag{4.5}$$

where B_1' is a new constant. Comparison of Equation (4.5) with Equation (4.1) shows that

$$A_h = \left(\frac{\tau_{ho}}{\tau_{eo}}\right) B_1' + \tau_{ho} \theta_h C_{xh} B_2' \tag{4.6}$$

Figure 4.4 shows a 3-D plot of A_h vs. τ_{ho} and τ_{eo}. Contrary to expectation, we see that A_h is independent of both τ_{ho} and τ_{eo}, which is an important discovery in this work. This can only be so if the concentrations n_t and N_x depend on N_{th} in Equation 4.3.

We first consider the newly generated defects so that the mean trapping rate becomes

$$\frac{1}{\tau_h} = \theta_h C_{th} N_{th} + \theta_h C_{xh} N_{xh} \tag{4.7}$$

To make the model work, we need to assume that the intrinsic deep traps are neutral with a small capture coefficient C_{th}. Suppose that irradiation converts a small fraction of these neutral traps into negatively charged centers, which would have a much larger capture coefficient, i.e. $C_{xh} > C_{th}$. The rate of conversion dN_{xh}/dt would be proportional to N_{th} and the dose rate dD/dt, which upon integration gives $N_{xh} = B_{xh}N_{th}D$, where B_{xh} is a constant, so that

$$\frac{1}{\tau_h} = \theta_h C_{th} N_{th} + B_{xh}\theta_h C_{xh} N_{th} D = \theta_h C_{th} N_{th}\left(1 + \frac{B_{xh}C_{xh}}{C_{th}} D\right) = \frac{1}{\tau_{ho}}\left(1 + A_h D\right) \tag{4.8}$$

which essentially leads to Equation 4.1 and explains the observation that A_h is independent of the hole lifetime. Similar arguments also apply to A_e given that A_e is also independent of τ_{ho} and τ_{eo}.

The above interpretation needs $C_{xh} > C_{th}$. Cycled-up residual voltage measurements place the total integrated concentrations of deep hole and electron traps at most around 2×10^{13} cm^{-3}, which is below the ESR measurement of the upper limit of spin active defects of 10^{14} cm^{-3} in a-Se [54, 55]. Further, combined IFTOF, first xerographic residual and cycled-up residual voltage measurements have been used to show that the deep hole traps are *neutral* and have a capture radius of 0.2 – 0.3 nm [56]. This corresponds to a typical bond length in a-Se. Deep electron traps are also neutral because once an electron is trapped in one of these deep traps, its recombination cross section with a hole is very large (Langevin cross section) as measured in a sequence of negative bias and positive bias TOF and IFTOF experiments [57]. Thus, spin active neutral defects of the type Se_1^0 and Se_3^0, cannot be ruled out from experiments given the small deep trap concentration. Indeed, structural modeling studies point to Se_3^0 as being the most stable neutral defect in a-Se [58]. Further *intimate valence alternation pair* (IVAP) defects of the type $(Se_1^- Se_3^+)$, $(As_2^- Se_3^+)$, $(Se_1^- As_4^+)$, $(Cl_0^- Se_3^+)$ would appear neutral but would become negative if the center captures an electron and is converted to a single VAP center by the

irradiation. There may also be seemingly neutral IVAP pairs in the structure [59], that may act as a hole or electron trap. In addition, structural simulation results show that the a-Se structure has stable $Se_3^0 - Se_3^0$ defects that link two chains [60]. Such a defect complex can also act as an intrinsic hole trap and readily explain the observed results in this work, because the x-ray induced conversion of $Se_3^0 - Se_3^0$ neutral defect complex to Se_3^+ and Se_1^-, the latter is a negatively charged center with a large hole capture coefficient.

The reduction in the hole lifetime may be due to new defects generated as explained above, or it may be due to trapped x-ray photogenerated electrons as expressed in Equation 4.2. Both effects are needed to model the drop in the sensitivity of x-ray detectors with x-ray irradiation in which the detectors have been biased to operate at fields 5 V/μm and 10 V/μm [15]. Trapped electrons act as recombination centers for holes. Zhao et al have studied ghosting and x-ray sensitivity reduction at two fields, 5 V/μm and 10 V/μm and through the shape of the TOF photocurrents have proposed heavy electron trapping; trapped electrons are then available to recombine with x-ray generated holes [61]. The main difference between the present experiments and those in References [15] and [61] is that the applied field is zero during irradiation in this work. X-ray photogeneration under a zero field is highly suppressed so there is probably only a limited number of electrons generated that can manage to diffuse out from the electron primary tracks and then become trapped. It is likely that the concentration of latter trapped electrons is much less than the concentration of x-ray generated defects. Thus, the n_t term on the right of Equation 4.2 is probably smaller than the N_{xh} term. Indeed, the reduction in the hole lifetime with absorbed dose in the presence of an applied field is much larger [62].

Some of the above arguments could be modified to apply to x-ray generated electron capture centers. There is a distinct difference in the behavior of τ_{eo} and τ_{ho} in a-Se. While τ_{ho} is very sensitive to the substrate temperature τ_{eo} is not [63]. Both are sensitive to alloying and impurities. The new electron traps would have to be generated from intrinsic defects inasmuch as A_e does not depend on τ_{eo}. Again, the new defect maybe a valence alternation defect or a hypervalent center.

4.3.2 X-ray Sensitivity and Charge Collection Efficiency

The reduction in the carrier lifetimes with x-ray irradiation will have a direct effect on the x-ray sensitivity by virtue of the reduction in the charge collection efficiency (η_c). However, the

actual calculation of the x-ray sensitivity needs the solution of the set of continuity, rate and Poisson equations as well as the rate of defect generation as described in References [15, 16]. The trapped charges and net space charge is then calculated to find the modified electric field, which then modifies the ionization energy $W_{\pm}$. We can nonetheless evaluate the x-ray irradiation effect on the change in the charge collection efficiency (CCE) η_c alone when a-Se is pre-exposed to x-rays.

In a uniform field in the absence of any x-ray preirradiation, the CCE η_{co} is given by [8],

$$\eta_{co} = \frac{\mu_h \tau_{ho} F}{L}\left(1 - \frac{\left[\exp\left(-\frac{L}{\mu_h \tau_{ho} F}\right) - \exp\left(-\frac{L}{\delta}\right)\right]}{\left[1-\exp\left(-\frac{L}{\delta}\right)\right]\left[1-\frac{\delta}{\mu_h \tau_{ho} F}\right]}\right) + \frac{\mu_e \tau_{eo} F}{L}\left(1 - \frac{\left[1-\exp\left(-\frac{L}{\delta}-\frac{L}{\mu_e \tau_{eo} F}\right)\right]}{\left[1-\exp\left(-\frac{L}{\delta}\right)\right]\left[1+\frac{\delta}{\mu_e \tau_{eo} F}\right]}\right) \qquad (4.9)$$

in which F is the applied field (assumed uniform), δ is the x-ray attenuation depth, i.e. 1/ linear attenuation coefficient α, L is the sample thickness, μ_e and μ_h are the electron and hole drift mobilities, τ_{eo} and τ_{ho} are the equilibrium electron and hole lifetimes in the unirradiated sample, and $\mu_e \tau_{eo} F$ and $\mu_h \tau_{ho} F$ are the electron and hole schubwegs in the unirradiated sample at the operating field of F. In Equation 5.8, η_{co} depends on the attenuation depth (δ) and carrier ranges i.e. $\mu\tau$ products, but only τ depends on the x-ray dose absorbed since the drift mobilities remain unaffected. It is assumed that the radiation receiving electrode is positive as it is the case in a-Se mammographic detectors. While Equation 4.9 is valid under a uniform field, it can still be used under large injection [64]. The dose absorbed through the sample can be represented as $D = D(x) = D_o \exp(-ax)$ where D_o is the absorbed dose in a thin slice near the sample surface and α is the linear attenuation coefficient of a-Se. Thus, the carrier trapping rates (reciprocal lifetimes) will vary across the sample following Equation 4.1 and are given as

$$1/\tau_h(x) = (1/\tau_{ho})[1 + A_h D_o \exp(-\alpha x)] \qquad (4.10)$$

and

$$1/\tau_e(x) = (1/\tau_{eo})[1 + A_e D_o \exp(-\alpha x)] \qquad (4.11)$$

where A_h and A_e are the A-values for holes and electrons. The reciprocal lifetime in Equation 4.10 or in Equation 4.11 represents the probability per unit time that a carrier becomes captured by a deep trap. We can calculate the mean probability of trapping over the sample thickness, which would represent the reciprocal effective lifetime by averaging Equations 4.10 and 4.11 over the sample length L. For example, for hole transport, the reciprocal of the effective hole lifetime is:

$$\frac{1}{\tau_{h(\text{eff})}} = \frac{1}{\tau_{ho}} \left\{ \frac{1}{L} \int_0^L [1 + A_h D_o \exp(-\alpha x)] dx \right\}$$

or

$$\frac{1}{\tau_{h(\text{eff})}} = \frac{1}{\tau_{ho}} \left\{ 1 + \frac{A_h D_o}{\alpha L} [1 - \exp(-\alpha L)] \right\} \tag{4.12}$$

Consider now an a-Se detector for mammography for which we can take the mean photon energy as 20 keV. Typical values for electron and hole transport in high quality stabilized a-Se are μ_h = 0.12 cm^2 V^{-1} s^{-1}, μ_e = 0.003 cm^2 V^{-1} s^{-1}, τ_{ho} = 20-50 μs, and τ_{eo} = 200-500 μs. Taking the values at the lower end, at an operating field of F = 10 V/μm, Equation 4.9 predicts that η_c = 95.9%. If the detector is then pre-exposed to x-rays with a dose D_o = 10 Gy (absorbed near the surface of a-Se), both τ_{ho} and τ_{eo} will drop but τ_h much more than τ_e. Typically a mean photon energy of 20 keV is used in mammography, whereas the lowest mean photon energy in the present work was 31.9 keV. However, the A-values did not show any dependence on the x-ray energy, nor on the dose rate. We can therefore assume that the A-values in Table 4.1 can also be used for 200 μm a-Se layers in mammographic detectors in the mammographic energy range, because A_h and A_e do not seem to depend on the photon energy. Using Equation 4.1 and A_h and A_e from Table 4.1, the new effective lifetimes are $\tau_{h(\text{eff})} \approx 13.4$ μs, and $\tau_{e(\text{eff})} \approx 176$ μs. The drift mobilities remain unchanged. The corresponding new collection efficiency is 94.5%, a drop of 1.4%. The mean absorbed dose in the sample involves averaging $D_o \exp(-\alpha x)$ and is 2.4 Gy. Figure 4.6 shows the dependence of the CCE on the field F in an unexposed a-Se detector and one which has been preirradiated with an absorbed mean dose of 2.4 Gy (10 Gy near the surface of the sample) for two cases. The first case is for a sample A with τ_{ho} = 50 μs, and τ_{eo} = 500 μs (typical values) and the second case is for a sample B with τ_{ho} = 20 μs, and τ_{eo} = 200 μs (the lowest end of electronic quality a-Se). As expected, the drop in the sensitivity gets worse at lower fields as observed in the sensitivity of commercial detectors [15]. The inset shows the change in the CCE as a percentage for the two samples A and B, which is negative and becomes bigger in magnitude as the field decreases. Further, in higher quality samples with longer carrier ranges, the drop in CCE with dose is less significant; compare samples A and B in the inset of Figure 4.6.

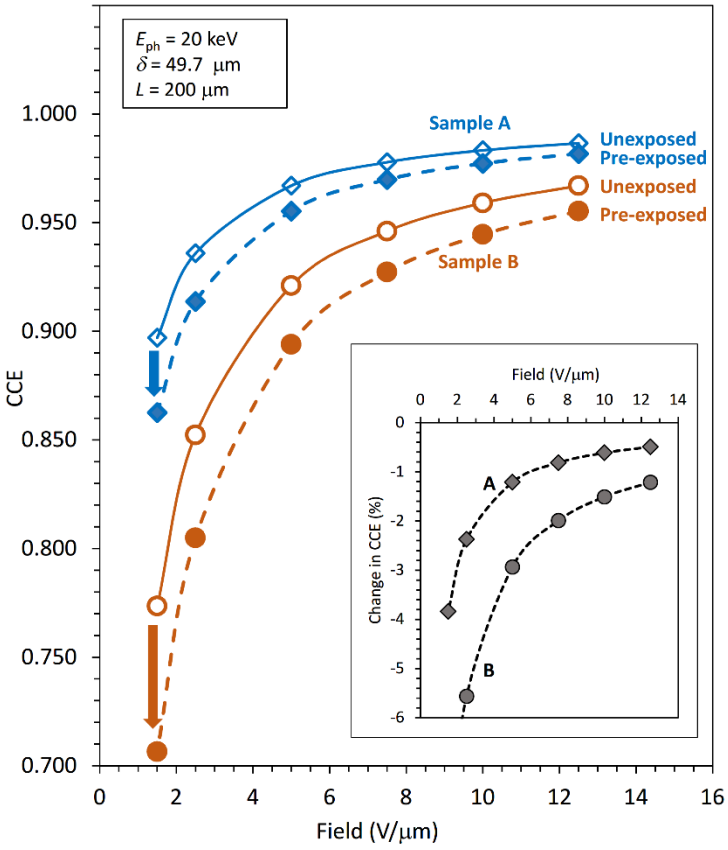

Figure 4.6: Charge collection efficiency (CCE) η_c as a function of applied field in an unexposed and preirradiated a-Se detector corresponding to pre-exposure equilibrium lifetimes of τ_{ho} = 50 µs and τ_{eo} = 500 µs for sample A (open and filled diamond points) and τ_{ho} = 20 µs and τ_{eo} = 200 µs (open and filled circles) for sample B. The inset shows the change in the CCE for the two samples as a function of the operating field. The dose absorbed in a thin surface region of a-Se is assumed to be 10 Gy (= D_o), and mean absorbed dose is 2.4 Gy. a-Se has a thickness of 200 µm, A_h = 0.203 Gy^{-1} and A_e = 0.062 Gy^{-1}. The x-ray photon energy is 20 keV and the linear attenuation coefficient α of a-Se is 201.4 cm^{-1}, and attenuation depth δ = 49.7 µm.

4.4 Conclusions

In this chapter the effects of high-dose x-ray irradiation on both electron and hole lifetimes, τ_e and τ_h, in stabilized a-Se photoconductive films in the absence of an applied electric field is examined. Within experimental errors, the hole and electron drift mobilities remain unaffected up to the highest doses delivered (~ 10 Gy). Thus, both electron and hole shallow

traps remain unaltered by x-ray irradiation. However, both τ_e and τ_h decrease with absorbed x-ray dose indicating an increase of deep charge-carrier traps due to x-ray irradiation. It was found that both τ_e and τ_h depend only on the total or accumulated absorbed dose D in a-Se, and not on the rate of dose delivery, dD/dt, over the range 0.15 Gy/s to 2.5 Gy/s and over x-ray photon energies from 50 keVp to 90 keVp (mean energies from 31.9 keV to 44.7 keV). Put differently, the x-ray induced effects on charge transport are independent of the x-ray intensity and photon energy, but are dependent on the total energy absorbed in a-Se. The latter finding allows the x-ray induced changes in the carrier lifetimes to be simply and conveniently modelled by $\tau_o/\tau = 1 + AD$, where τ_o is the charge-carrier lifetime before x-ray exposure (equilibrium lifetime), τ is the charge-carrier lifetime after exposure, D is the total absorbed dose and A is a constant, without further complications arising from the rate of dose delivery and photon energy. The constant A gauges the strength of the x-ray induced reduction in the lifetime per unit absorbed dose. It's found that at 23.5 °C, A = 0.203 (± 0.021) Gy^{-1} for the hole lifetime and 0.0620 (± 0.090) Gy^{-1} for the electron lifetime, so the x-ray induced effect on hole trapping is about a factor 3 larger than that for electron trapping.

As there is no x-ray induced change in the electron and hole drift mobilities, the hole and electron schubwegs follow the dose-dependence of the respective lifetimes, that is, $\tau_o/\tau = 1 + AD$. An effective lifetime was calculated based on suitably averaging the rate of carrier trapping (i.e. probability of trapping) across the a-Se device and thereby calculated the charge collection efficiency (CCE) in pre-exposed a-Se detectors. The results clearly show that there is a marked drop in the CCE efficiency under a high-dose x-ray irradiation and the drop is larger under lower operating fields. High field operation therefore suppresses the effects of x-ray induced changes in the carrier lifetimes involved in the CCE. Further, the electronic quality of the photoconductive material was shown to be also very important because those samples with longer electron and hole lifetimes (high quality electronic grade a-Se) exhibited less deterioration with x-ray exposure.

5. X-Ray Induced Effects in Stabilized a-Se in the Presence of an Applied Field

5.1 Introduction

The goal of this chapter is to report the experimental results on the x-ray induced effects on hole charge transport in stabilized amorphous selenium in the presence of an applied field. The results in this section were measured using the TOF and IFTOF experiments described in previous chapters. The TOF technique is used to measure the charge-carrier drift mobility, and the IFTOF technique is used to find the charge-carrier lifetime. The product of the hole mobility and lifetime gives the hole range, that is how far the hole can travel through a sample before trapping per unit field, which is important in determining the charge collection efficiency of an x-ray detector. The effect of x-ray irradiation of a-Se samples under an applied field on the hole drift mobility and lifetime are investigated. Samples were allowed to rest and TOF and IFTOF measurements were taken to get the pre-exposure drift mobility and lifetime of the sample. Then the sample is placed under an electrical bias and exposed to x-ray radiation, after which the hole drift mobility and lifetime are measured again. The effects of x-ray radiation is measured as a function of absorbed dose in the samples. This is repeated at different dose rates, at different x-ray photon energies, and different electrical fields.

5.2 Results

The results in the previous chapter show that the charge-carrier trapping lifetimes decrease as an a-Se sample is exposed to x-rays in the absence of an applied electric field. The reduction in the carrier lifetime, of holes and electrons, due to x-ray exposure does not depend on the dose rate, the x-ray photon energy, or the pre-exposure (resting) lifetimes, but only on the total dose absorbed by the sample. In this chapter the effects on the hole transport properties, drift mobility and trapping lifetime, due to x-ray exposure in the presence of an applied or nominal electric field are examined. The applied or nominal field is simply the applied bias voltage per unit sample thickness, V/L.

The time-of-flight (TOF) and interrupted-field time-of-flight (IFTOF) transient photoconductivity techniques, detailed in Chapters 2 and 3, are effective tools for measuring the charge transport properties in stabilized a-Se photoconductors. Both techniques measure the

transient response of charge-carriers photoinjected into a sample. The time width of the TOF I-mode pulse is related to the drift mobility of the charge-carriers. The IFTOF experiment interrupts the drift of the charge-carriers as they travel across the sample and the fractional recovered photocurrent is related to the charge-carrier lifetime.

The TOF and IFTOF measurements are used to obtain the pre-exposure drift mobility and trapping lifetime on a well rested a-Se sample at room temperature. The sample was found to have a hole mobility of 0.12 cm^2/Vs, a hole lifetime of 44 ± 3 μs, an electron drift mobility of 0.002 cm^2/Vs, and an electron lifetime of 431 ± 15 μs. In order to measure the effects of x-ray exposure on the hole lifetime in a-Se under an applied field, the procedure detailed in Section 3.7 is followed. The sample is placed under a high electric field, during which it receives a dose of x-ray exposure. The absorbed dose in the sample is calculated following the procedure detailed in Section 3.6.1. The electric field is then removed from the sample and a TOF or IFTOF experiment is performed to find the hole mobility or lifetime after exposure. This is repeated until the hole transport properties reach a saturated value or the accumulated dose becomes sufficiently high. Each successive exposure and TOF or IFTOF measurement is performed within a short enough interval that the sample does not begin to recover. Each TOF and IFTOF measurement is saved as raw data to be analyzed.

As in the case of no applied field, when the sample is placed under a high electric field during exposure there is no observed measureable changes in the hole transit time after x-ray exposure. Thus the hole drift mobility is unaffected by x-ray irradiation.

Analysis of the reduction of the hole lifetime due to absorbed dose in the sample is done on the inverted normalized lifetime, that is the normalized hole trapping rate, to attempt to generalize the effects of x-ray exposure in the presence of a high electric field. The hole lifetime is normalized to the pre-exposure hole trapping lifetime τ_{ho} and is inverted, resulting in τ_{ho}/τ_h where τ_h is the hole lifetime after exposure. The normalized reciprocal hole lifetime due to x-ray dose under high fields is shown in Figure 5.1, Figure 5.2, and Figure 5.3. In Figure 5.1 the sample is placed under an electric field of 5 V/μm, in Figure 5.2 the sample is placed under an electric field of 7.5 V/μm, and in Figure 5.3 the sample is placed under an electric field of 10 V/μm. In each figure the dose rate is varied as well as the peak photon energy of the x-ray beam.

The solid lines in Figure 5.1, Figure 5.2, and Figure 5.3 are the best curve fits based on representing the dependence of the hole lifetime on absorbed dose by an empirical formula:

$$\frac{\tau_{ho}}{\tau_h} = 1 + B(1 - \exp(-\frac{D}{C})) \quad (5.1)$$

where τ_{ho} is the hole lifetime before x-ray irradiation, τ_h is the hole lifetime after irradiation, D is the total accumulated dose absorbed in the sample (Gy), B is a constant (in this case measured to be 4.21), and C is a parameter that depends on the applied field and has the units of Grays (Gy).

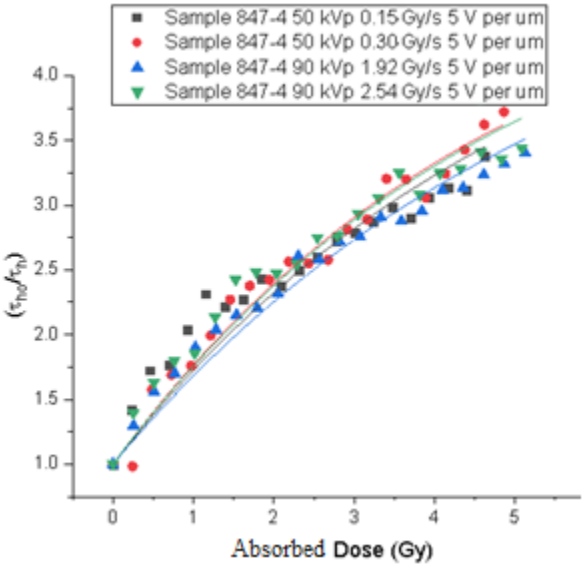

Figure 5.1: Normalized reciprocal hole lifetime reduction due to absorbed x-ray dose. The sample is placed under an electric field of 5 V/μm during exposure. Four different dose rates and two different peak photon energies are used. The solid lines are best curve fits of Equation 5.1 with B = 4.21 (obtained on Origin)

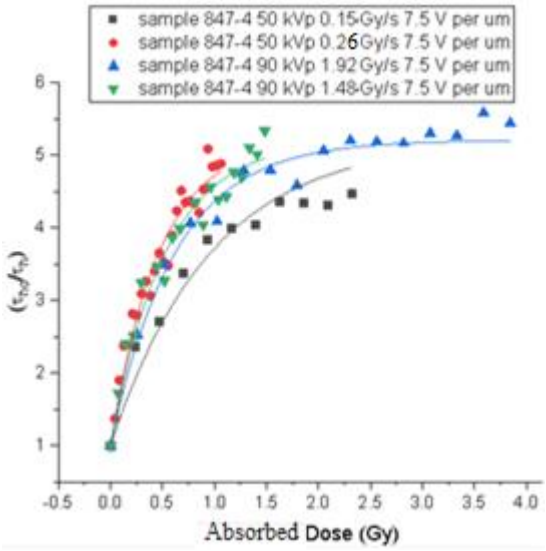

Figure 5.2: Normalized reciprocal hole lifetime reduction due to absorbed x-ray dose. The sample is placed under an electric field of 7.5 V/μm during exposure. Four different dose rates and two different peak photon energies are used. The solid lines are best curve fits of Equation 5.1 with B = 4.21 (obtained on Origin)

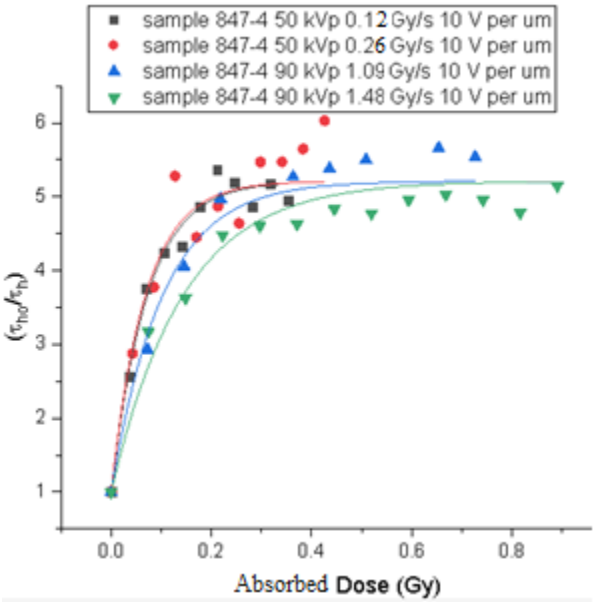

Figure 5.3: Normalized reciprocal hole lifetime reduction due to absorbed x-ray dose. The sample is placed under an electric field of 10 V/μm during exposure. Four different dose rates and two different peak photon energies are used. The solid lines are best curve fits of Equation 5.1 with B = 4.21 (obtained on Origin)

It is apparent from the plots in Figure 5.1, Figure 5.2, and Figure 5.3 that there is a reduction in the hole lifetime due to x-ray exposure, just as in the case where there is no applied field during exposure. The plots also show that Equation 5.1 can reasonably describe the hole lifetime dependence on the absorbed dose, which is discussed further below.

The parameters of the empirical relationship of the normalized inverted hole lifetime to the absorbed dose in Equation 5.1 for each plot in Figure 5.1, Figure 5.2, and Figure 5.3 are shown in Table 5.1, Table 5.2, and Table 5.3 respectively. Also shown in the tables are the adjusted R^2 values. The parameters and adjusted R^2 values are obtained with Origin.

Table 5.1: Parameters of the best curve fit of the empirical equation in Equation 5.1 for the plots in Figure 5.1. (obtained on Origin)

Plot	Sample 847-4 50 kVp 0.15 Gy/s 5 V per μm	Sample 847-4 50 kVp 0.30 Gy/s 5 V per μm	Sample 847-4 90 kVp 1.92 Gy/s 5 V per μm	Sample 847-4 90 kVp 2.54 Gy/s 5 V per μm
C (Gy)	5.31 ± 0.220	4.98 ± 0.12	5.66 ± 0.13	5.05 ± 0.15
B	4.21	4.21	4.21	4.21
Adj. R^2	0.876	0.975	0.968	0.948

Table 5.2: Parameters of the best curve fit of the empirical equation in Equation 5.1 for the plots in Figure 5.2. (obtained on Origin)

Plot	Sample 847-4 50 kVp 0.15 Gy/s 7.5 V per μm	Sample 847-4 50 kVp 0.26 Gy/s 7.5 V per μm	Sample 847-4 90 kVp 1.92 Gy/s 7.5 V per μm	Sample 847-4 90 kVp 1.48 Gy/s 7.5 V per μm
C (Gy)	0.963 ± 0.065	0.466 ± 0.015	0.623 ± 0.036	0.527 ± 0.025
B	4.21	4.21	4.21	4.21
Adj. R^2	0.938	0.964	0.976	0.961

Table 5.3: Parameters of the best curve fit of the empirical equation in Equation 5.1 for the plots in Figure 5.3. (obtained on Origin)

Plot	Sample 847-4 50 kVp 0.12 Gy/s 10 V per µm	Sample 847-4 50 kVp 0.26 Gy/s 10 V per µm	Sample 847-4 90 kVp 1.09 Gy/s 10 V per µm	Sample 847-4 90 kVp 1.48 Gy/s 10 V per µm
C (Gy)	0.0720 ± 0.0046	0.0684 ± 0.0117	0.103 ± 0.012	0.143 ± 0.012
B	4.21	4.21	4.21	4.21
Adj. R^2	0.979	0.905	0.968	0.952

The plots in the above figures each contain multiple experiments. Each run was done with a different dose rate *dD/dt*, over the range 0.12 Gy/s to 2.5 Gy/s and over x-ray photon energies from 50 keVp to 90 keVp (mean energies from 31.9 keV to 44.7 keV). Despite this, the reduction in the lifetime due to x-ray exposure follows the same trend, implying that there is no apparent dependence on the dose rate or the photon energy of the beam. To verify the latter argument, the parameter C from the empirical equation in Equation 5.1 is plotted against the absorbed dose rate and the average photon energy in the x-ray beam in Figure 5.4 (a) and (b) respectively. From these plots, it is apparent that there is no dependence of the parameter C on either the dose rate or the photon energy, within experimental errors, when the sample is under an applied field during exposure.

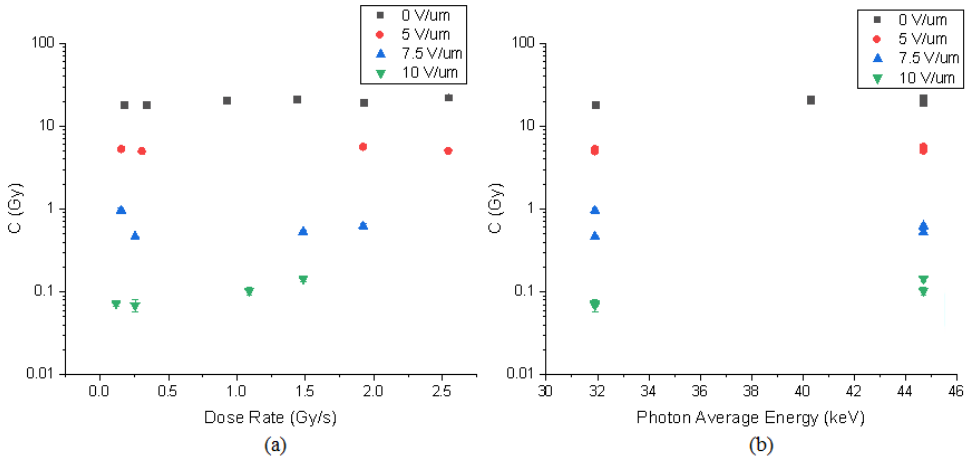

Figure 5.4: (a) Dependence of the parameter *C* in Equation 5.1 on the absorbed dose rate. The plot shows the different applied fields. (b) Dependence of the parameter *C* in Equation 5.1 on the average photon energy of exposure. The plot shows the different applied fields.

As the empirical equation in Equation 5.1 is a reasonably accurate description of the reduction in the hole lifetime due to absorbed dose, and the parameter C has essentially no dependence on the dose rate or photon energy, it can be inferred that the reduction in the hole lifetime due to absorbed dose in the sample does not depend on the dose rate or photon energy when the sample is under an applied electric field. This is the same as in the case of no applied field as shown in Chapter 4.

As the dose rate and photon energy do not have an effect on the reduction in the hole lifetime, the experiments were combined according to the applied field during exposure. Then, the reduction of the hole lifetime due to dose absorbed in the sample under different applied fields is examined. In Figure 5.5, the normalized reciprocal hole lifetime due to x-ray dose with the sample under electric fields 0 V/μm, 5 V/μm, 7.5 V/μm, and 10 V/μm are compared. The solid lines are the best curve fits based on Equation 5.1. It is apparent from this plot that there is a large dependence of the reduction in the hole lifetime due to absorbed dose on the applied electric field during exposure. This indicates that the best curve fit equation in Equation 5.1 also has a strong dependence on the applied electric field during exposure. The parameters of the empirical relationship of the normalized inverted hole lifetime to the absorbed dose in Equation 5.1 for the plot in Figure 5.5 is shown in Table 5.4 along with the adjusted R^2 values. The parameters and adjusted R^2 values are obtained with Origin.

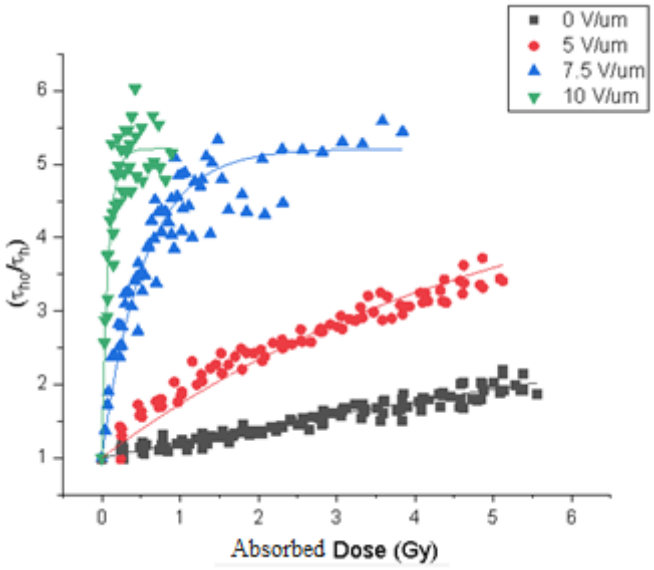

Figure 5.5: Comparison of the normalized reciprocal hole lifetime reduction due to x-ray absorbed dose under differing electric fields. The sample is placed under electric fields 0 V/μm, 5 V/μm, 7.5 V/μm, and 10 V/μm during exposure. The solid lines are best curve fits of Equation 5.1 with B = 4.21 (obtained on Origin)

Table 5.4: Parameters of the best curve fit of the empirical equation in Equation 5.1 for the plots in Figure 5.5. (obtained on Origin)

Plot	0 V/μm	5 V/μm	7.5 V/μm	10 V/μm
C (Gy)	19.9 ± 0.3	5.24 ± 0.08	0.540 ± 0.020	0.0844 ± 0.0059
B	4.21	4.21	4.21	4.21
Adj. R^2	0.930	0.941	0.918	0.920

The large dependence on the electric field of the reduction in the hole lifetime due to x-ray exposure comes from the parameter C. In Figure 5.6, the parameter C is plotted against the electric field applied during exposure. The solid line is the best curve fit representing the dependence of the parameter C on the electric field through an empirical exponential expression:

$$C = C_1 e^{-(F/C_2)^{\beta}} + C_3 \tag{5.2}$$

where F is the applied electric field during exposure, and C_1 (Gy), C_2 (V/μm), C_3 (Gy), and β are constants. Notice that Equation 5.2 has a stretched exponential term, which is not uncommon in

the area of amorphous semiconductors. The values for the constants are shown in Table 5.5 along with the adjusted R^2 value. The parameters and adjusted R^2 value are obtained on Origin.

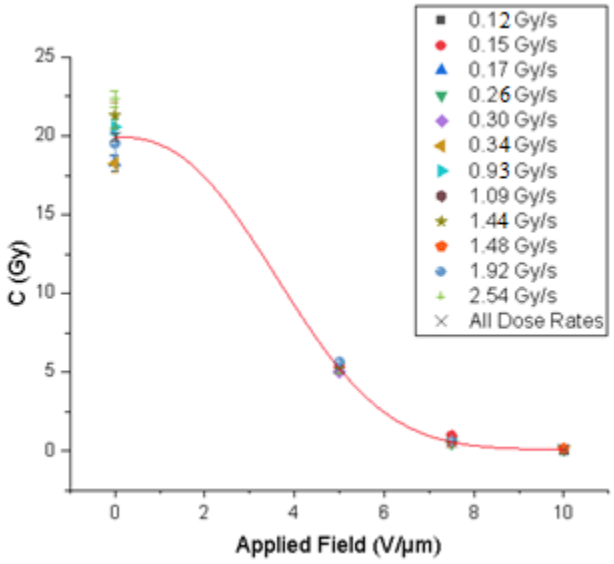

Figure 5.6: Dependence of the parameter C on the applied electric field during exposure. The plot shows the different absorbed dose rates used.

Table 5.5: Constants of the best curve fit of the empirical equation in Equation 5.2 for the plot in Figure 5.6. (obtained on Origin)

Constant	C_1 (Gy)	C_2 (V/µm)	C_3 (Gy)	β
Value	19.9 ± 0.7	4.44 ± 0.09	0.06	2.49 ± 0.12
Adj. R^2	0.998			

5.3 Discussion

5.3.1 Defect Generation

As there were no measureable changes in the hole drift mobility after x-ray exposure, and the transport of photoinjected holes is controlled by shallow traps, it is concluded that the concentration of shallow traps is unaffected by x-ray exposure in the presence of an applied electric field. There is however a large change in the hole lifetime, indicating large changes in deep traps due to x-ray exposure in the presence of an applied electric field.

The reduction in the hole lifetime may be due to the generation of new defects (as explained in Chapter 4, or due to recombination with trapped electrons. The probability of trapping holes per unit time after irradiation can be described by the capture of holes into intrinsic deep traps already present in the sample, capture by trapped electrons (effective recombination), and capture into x-ray generated defects. That is:

$$\frac{1}{\tau_h} = \theta_h C_{th} N_{th} + C_r n_t + \theta_h C_{xh} N_{xh} \tag{5.3}$$

where it is assumed that the hole drift is controlled by shallow traps, θ_h is the hole mobility reduction factor (= effective drift mobility / band mobility), $\theta_h C_{th} N_{th}$ is the reciprocal intrinsic hole lifetime ($1/\tau_{ho}$), i.e. the mean capture probability per unit time into intrinsic deep traps with a concentration N_{th} and a capture coefficient C_{th}, C_r is the recombination coefficient of drifting holes with trapped electrons whose concentration is n_t, and N_{xh} is the concentrations of one particular species of defects (hole traps) that has been generated (there may be more species) whose capture coefficient is C_{xh}. The trapped electron concentration n_t in Equation 5.3 would be due to the trapping of x-ray generated electrons. Normalizing Equation 5.3 and setting it equal to Equation 5.1 for comparison, we have,

$$\frac{\tau_{ho}}{\tau_h} = 1 + \frac{C_r n_t}{\theta_h C_{th} N_{th}} + \frac{C_{xh} N_{xh}}{C_{th} N_{th}} = 1 + B(1 - e^{-D/C}) \tag{5.4}$$

The trapped electron concentration n_t depends on three factors: how many electrons have been photogenerated, which is proportional to the absorbed dose D and is inversely proportional to the electron-hole creation energy $W_{\pm}$, how many traps are available to trap these electrons, which depends on the intrinsic trap concentration N_{te}, and the capture coefficient C_{te}. The electron-hole creation energy is inversely proportional to the applied field, thus as the applied field increases, the generated trapped electron concentration for a certain amount of absorbed dose should increase. Electron trapping has been proposed before in Reference [61] when studying the effect of ghosting and sensitivity reduction at high electric fields. Trapped electrons are able to recombine with photogenerated holes, which will shorten the hole lifetime. As the x-ray photogeneration of electron-hole pairs is suppressed at low fields, the n_t term on the right of Equation 5.3 is probably smaller than the N_{xh} term when the applied field during exposure is small. However, as the applied field during exposure increases, the n_t term probably begins to dominate over the N_{xh} term. In other words, the decrease in the observed hole lifetime is

dominated by x-ray generated traps at low electric fields during exposure, but begins to be dominated by the recombination of holes with trapped electrons as the applied field during exposure increases. The observed saturation of the normalized inverted hole lifetime may be due to all of the intrinsic electron traps being full.

In the low dose region or in the case of no applied field, where $B/C \ll 1$, the empirical equation in Equation 5.1 reduces to a linear approximation:

$$\frac{\tau_{ho}}{\tau_h} = 1 + \frac{B}{C}D \tag{5.5}$$

Comparing this with Equation 4.1 we get

$$\frac{B}{C} = A_h \tag{5.6}$$

In the case of no applied field, Equation 5.1, which represents the reduction of the hole lifetime in the presence of an applied field, reduces to Equation 4.1, which represents the reduction of the hole lifetime in the absence of an applied field. At zero field, C in Equation 5.2 equates to 19.93 Gy, and B/C becomes 0.21 which agrees within experimental errors with the value for A_h found in Table 4.1. In Figure 5.7 B/C is plotted against the applied field during exposure. The solid line is the best curve fit representing the dependence of B/C on the electric field through the empirical exponential expression:

$$\frac{B}{C} = A_h = A_{ho} + A_1 e^{-A_2 F} \tag{5.7}$$

where F is the applied electric field during exposure, and A_1 (Gy^{-1}), A_2 $(V/\mu m)^{-1}$, and A_{ho} (Gy^{-1}) are constants. The values for the constants are shown in Table 5.6 along with the adjusted R^2 value. The parameters and adjusted R^2 value were obtained on Origin.

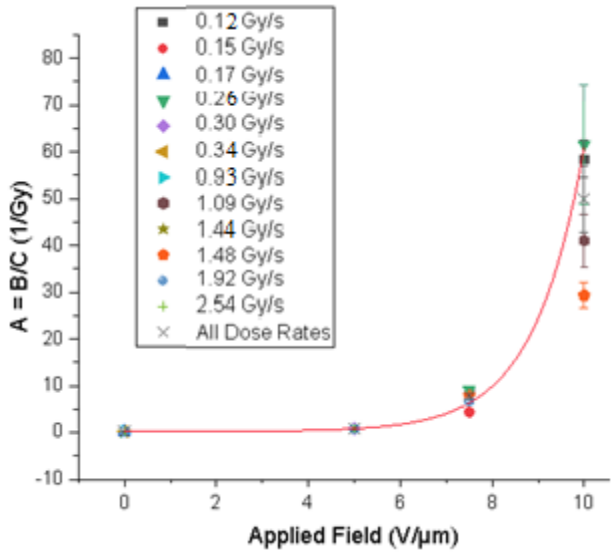

Figure 5.7: Dependence of *B*/*C* on the applied electric field during exposure. The plot shows the different absorbed dose rates used.

Table 5.6: Constants of the best curve fit of the empirical equation in Equation 5.7 for the plot in Figure 5.7. (obtained on Origin)

Constant	A_{ho} (Gy^{-1})	A_1 (Gy^{-1})	A_2 (V/µm)$^{-1}$
Value	0.205 ± 0.019	0.00618 ± 0.00268	0.920 ± 0.070
Adj. R^2	0.961		

From the plot in Figure 5.7 it is seen that the A-value has an exponential relationship with the applied electric field during exposure. The A-value represents the initial linear reduction of the hole lifetime due to absorbed dose in a sample.

5.3.2 X-ray Sensitivity and Charge Collection Efficiency

The reduction in the hole lifetimes with x-ray exposure has a direct effect on the x-ray sensitivity of a x-ray detector through the charge collection efficiency (CCE) η_c. In a uniform field in the absence of any x-ray preirradiation, the CCE η_{co} is given by [8],

$$\eta_{co} = \frac{\mu_h \tau_{ho} F}{L}\left(1 - \frac{\left[\exp\left(-\frac{L}{\mu_h \tau_{ho} F}\right) - \exp\left(-\frac{L}{\delta}\right)\right]}{\left[1-\exp\left(-\frac{L}{\delta}\right)\right]\left[1-\frac{\delta}{\mu_h \tau_{ho} F}\right]}\right) + \frac{\mu_e \tau_{eo} F}{L}\left(1 - \frac{\left[1-\exp\left(-\frac{L}{\delta}-\frac{L}{\mu_e \tau_{eo} F}\right)\right]}{\left[1-\exp\left(-\frac{L}{\delta}\right)\right]\left[1+\frac{\delta}{\mu_e \tau_{eo} F}\right]}\right) \quad (5.8)$$

in which F is the applied field (assumed uniform), δ is the x-ray attenuation depth, i.e. 1/ linear attenuation coefficient α, L is the sample thickness, μ_e and μ_h are the electron and hole drift mobilities, τ_{eo} and τ_{ho} are the equilibrium electron and hole lifetimes in the unirradiated sample, and $\mu_e\tau_{eo}F$ and $\mu_h\tau_{ho}F$ are the electron and hole schubwegs in the unirradiated sample at the operating field of F. In Equation 5.8, η_{co} depends on the attenuation depth (δ) and carrier ranges, i.e. $\mu\tau$ products, but only τ depends on the x-ray dose absorbed since the drift mobilities remain unaffected. It is assumed that the radiation receiving electrode is positive as it is the case in a-Se mammographic detectors. While Equation 5.8 assumes the detector is under a uniform field, it can still be used under large injection [64]. The first term in Equation 5.8 represents the collection efficiency of holes and the second term represents the collection efficiency of electrons. As only hole transport as a function of absorbed dose was studied in this chapter, only the CCE of holes will be considered. That is:

$$\eta_{ch} = \frac{\mu_h\tau_{ho}F}{L}\left(1 - \frac{\left[\exp\left(-\frac{L}{\mu_h\tau_{ho}F}\right) - \exp\left(-\frac{L}{\delta}\right)\right]}{\left[1-\exp\left(-\frac{L}{\delta}\right)\right]\left[1-\frac{\delta}{\mu_h\tau_{ho}F}\right]}\right) \tag{5.9}$$

To get an accurate depiction of the change in the hole CCE, the hole CCE will be normalized with respect to perfect hole collection. That is $\eta_{ch(\text{nomalized})} = \eta_{ch}/\eta_{ch\infty}$ where $\eta_{ch(\text{nomalized})}$ is the normalized hole CCE, and $\eta_{ch\infty}$ is the hole CCE with perfect hole transport (hole lifetime is infinite). The dose absorbed through the sample can be represented as $D = D(x) = D_o\exp(-ax)$ where D_o is the absorbed dose in a thin slice near the sample surface and α is the linear attenuation coefficient of a-Se. As the absorbed dose varies throughout the sample, the hole trapping rate (reciprocal lifetime) will vary across the sample following Equation 5.1 and is given as:

$$\frac{1}{\tau_h(x)} = \frac{1}{\tau_{ho}}\left[1 + B\left(1 - \exp\left(-\frac{D_o\exp(-\alpha x)}{C}\right)\right)\right] \tag{5.10}$$

where B is the constant shown in Table 5.4 and C is the parameter that depends on the applied electric field during exposure shown in Table 5.4. The reciprocal lifetime in Equation 5.10 represents the probability per unit time that a carrier becomes captured by a deep trap. We can calculate the mean probability of trapping over the sample thickness, which would represent the reciprocal effective lifetime by averaging Equation 5.10 over the sample length L. Thus the reciprocal of the effective hole lifetime is:

$$\frac{1}{\tau_{h(\text{eff})}} = \frac{1}{\tau_{ho}}\left\{\frac{1}{L}\int_0^L \left[1 + B(1 - \exp(-\frac{D_o \exp(-\alpha x)}{C}))\right] dx\right\} \quad (5.11)$$

Consider now an a-Se detector for mammography for which we can take the mean photon energy as 20 keV. Typical values for hole transport in high quality stabilized a-Se are μ_h = 0.12 cm^2 V^{-1} s^{-1}, and τ_{ho} = 20-500 μs. Although τ_{ho} = 500 μs may seem unrealistic, it has indeed been reported on high quality a-Se [65]. Taking the values at the lower end, and an operating field of F = 10 V/μm, Equation 5.9 predicts that η_{ch} = 74.4%. If the detector is then pre-exposed to x-rays with a dose D_o = 10 Gy (absorbed near the surface of a-Se) under an applied field of 10 V/μm, τ_{ho} will drop. Typically a mean photon energy of 20 keV is used in mammography, whereas the lowest mean photon energy in the present work was 31.9 keV. However, the parameter C did not show any dependence on the x-ray energy, nor on the dose rate. We can therefore assume that the C parameters for each applied field in Table 5.4 can also be used for 200 μm a-Se layers in mammographic detectors in the mammographic energy range. Using Equation 5.11 and C from Table 5.4, the new effective hole lifetime of the pre-exposed detector is $\tau_{h(\text{eff})} \approx 3.86$ μs. The drift mobility remains unchanged. The corresponding new hole collection efficiency is 64.8%, a drop of 12.9%. The mean dose in the sample involves averaging $D_o\exp(-\alpha x)$ and is 2.4 Gy. Figure 5.8 shows the dependence of the normalized CCE on the field F in an unexposed a-Se detector and one that which has been preirradiated with an absorbed mean dose of 2.4 Gy (10 Gy near the surface of the sample) for three cases. The CCE is normalized to a sample with infinite lifetime, where all the generated holes are collected. The first case is for a sample A with τ_{ho} = 500 μs (the highest end of electronic quality a-Se), the second case is for a sample B with τ_{ho} = 50 μs (typical value) and the third case if for a sample C with τ_{ho} = 20 μs (the lowest end of electronic quality a-Se). As expected, the drop in the sensitivity gets worse at lower operating fields as observed in the sensitivity of commercial detectors [15]. The inset shows the change in the CCE as a percentage for the three samples A, B and C, which is negative and becomes bigger in magnitude as the field decreases. Further, in higher quality samples with longer carrier ranges, the drop in CCE with dose is less significant; compare samples A, B and C in the inset of Figure 5.8.

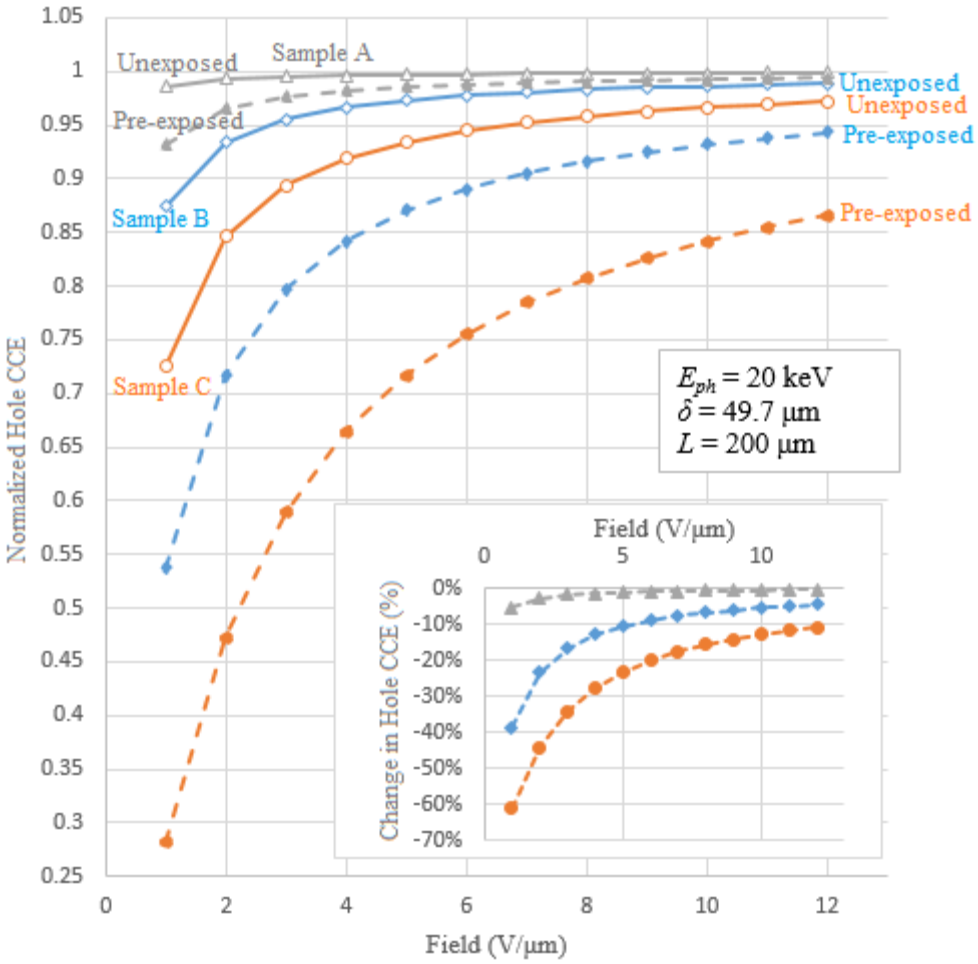

Figure 5.8: Normalized charge collection efficiency (CCE) of holes $\eta_{ch}/\eta_{ch\infty}$ as a function of applied field in an unexposed and preirradiated a-Se detector corresponding to pre-exposure equilibrium lifetimes of τ_{ho} = 500 µs for sample A (open and filled triangles), τ_{ho} = 50 µs for sample B (open and filled diamonds) and τ_{ho} = 20 µs for sample C (open and filled circles). The charge collection efficiency for each sample is normalized to a sample with perfect hole collection. The inset shows the change in the CCE for the three samples as a function of the applied field. The dose absorbed in a thin surface region of a-Se is assumed to be 10 Gy (= D_o), and mean absorbed dose is 2.4 Gy. The a-Se layer has a thickness of 200 µm and the parameter C = 0.07 Gy corresponding to exposure under an applied field of 10 V/µm. The x-ray photon energy is 20 keV and the linear attenuation coefficient α of a-Se is 201.4 cm^{-1}, and attenuation depth δ = 49.7 µm.

5.4 Conclusion

In this chapter the effects of x-ray radiation on the hole transport properties in stabilized amorphous selenium thin films in the presence of an applied field was examined. The hole mobility was found to have no change after x-ray exposure, but there was a reduction in the hole lifetime with absorbed x-ray dose in the sample. This reduction was found to not have any dependence on the rate of dose delivery, *dD/dt*, over the range 0.12 Gy/s to 2.5 Gy/s and over x-ray photon energies from 50 keVp to 90 keVp (mean energies from 31.9 keV to 44.7 keV), but only on the total x-ray dose and the applied field during exposure. Put differently, the x-ray induced effects on charge transport are independent of the x-ray intensity and photon energy, but dependent on the total energy absorbed in a-Se and the applied field during exposure. An empirical formula was found to model the changes in the hole lifetime with absorbed dose, $\tau_{ho}/\tau_h = 1 + B[1 - \exp(-D/C)]$ where τ_{ho} is the hole lifetime before x-ray exposure (equilibrium lifetime), τ_h is the hole lifetime after exposure, D is the total absorbed dose, B is a constant, and C is a parameter that depends on the applied field during exposure empirically as $C = C_1\exp[-(F/C_2)^{\beta}] + C_3$ where C_1, C_2, C_3, and β are constants. The constants were found experimentally to be; $B \approx 4.21$, $C_1 \approx 19.9$ Gy, $C_2 \approx 4.44$ V/μm, $C_3 \approx 0.06$ Gy, and $\beta \approx 2.49$. The empirical equation $\tau_{ho}/\tau_h = 1 + B[1 - \exp(-D/C)]$ reduces to $\tau_{ho}/\tau_h = 1 + B(D/C)=1+AD$ (where $A = B/C$ and is a constant) for sufficiently low doses. This is a linear approximation of the x-ray induced effects and matches the model found for the case with no applied field discussed in Chapter 4.

Within experimental errors, the hole drift mobility remained unaffected from absorbed dose. Thus the hole shallow traps remain unaltered by x-ray irradiation. The hole schubweg follows the dose-dependence of the hole lifetime. The effective hole lifetime is calculated by averaging the rate of hole trapping across a-Se detectors upon receiving x-ray dose. With this the hole charge collection efficiency (CCE) in the pre-exposed detector is calculated and compared to the hole CCE in the unexposed detector. The comparison shows a large drop in the hole CCE after x-ray dose is absorbed in the detectors, and this drop grows as the operating field decreases. The drop in the hole CCE can be reduced by increasing the operating field as well as by using higher quality electronic grade a-Se in the detector. That is samples with longer unexposed hole lifetimes show a smaller drop in the CCE due to x-ray exposure.

6. Summary and Conclusions

Radiography is an important diagnostic tool used in medical treatments. Modern x-ray imaging relies on digital radiography and in particular the direct conversion flat-panel x-ray image detectors for mammography. These detectors contain an x-ray sensitive photoconductive layer coated onto the surface of a large-area thin-film transistor (TFT) active-matrix-array (AMA). X-ray photons absorbed in the photoconductive layer are converted into electron-hole pairs through the photoelectric effect and the ionization of the medium by the primary electron. The electrons and holes are separated and collected under the influence of an applied electric field. This creates a spatial charge distribution on the TFT AMA which is proportional to the incident radiation image. These detectors are self-scanning through the TFTs, compact, and produce high quality digital x-ray images. Currently the best material for the photoconductive layer in the mammography modality is alloys of amorphous selenium (a-Se) due to their high absorption, good electron and hole transport properties, low dark currents, and simplicity in creating large uniform and homogeneous layers.

In order to investigate the charge-carrier transport properties of a-Se layers, a system capable of performing time-of-flight (TOF) and interrupted-field time-of-flight (IFTOF) measurements was used. The TOF technique measures the transient photocurrent induced from the drift of charge-carriers across a highly resistive sample to determine the charge-carrier drift mobility μ. The IFTOF technique interrupts the drift of the charge-carriers by removing the applied field, allowing the carriers to interact with deep traps in the sample. This causes a drop in the induced photocurrent from before to after the interruption, which can be used to calculate the charge-carrier lifetime τ. The charge-carrier drift mobility and lifetime are important properties of the a-Se layers because the product $\mu\tau F$, where F is the applied field, determines the charge-carrier schubweg, which in turn determines the charge-collection efficiency and the x-ray sensitivity of the x-ray detector.

The TOF and IFTOF experimental system used in this work is based on a grounded bridge network, which contains balanced resistors, a high voltage capacitor to match the sample capacitance, and twelve high-speed diodes in order to eliminate the high displacement currents

that are inherent in the IFTOF experiment. The transient photocurrent signal in either experiment is detected using a high-speed differential amplifier across the branches of the bridge network, and is recorded with an oscilloscope.

Using the TOF and IFTOF experiments the effects of x-ray radiation on the charge-carrier transport properties was examined. In particular the dependence of the reduction in the charge-carrier lifetime due to x-ray radiation on the dose rate, x-ray photon energy and applied electric field during exposure is examined. The x-ray induced effects are measured in terms of the absorbed dose in the sample. The dose is calculated from the x-ray exposure measured using a dosimeter. The results are examined as the normalized inverted lifetime after exposure to x-ray radiation, that is, τ_o/τ where τ is the lifetime after x-ray exposure and τ_o is the lifetime before exposure.

6.1 X-ray Induced Effects in a-Se in the Absence of an Applied Field

The first goal in this investigation was to examine the dependence of x-ray induced effects on the transport properties in a-Se on the x-ray photon energy of exposure. When an a-Se sample, under no applied electric field, is exposed to x-ray radiation there is no change in the charge-carrier drift mobilities. However there is a large change in the charge-carrier lifetimes. As the amount of absorbed dose increases the charge-carrier lifetimes decrease. Plotting the normalized inverted lifetime against the absorbed dose gave a linear plot that fit the equation $\tau_o/\tau = 1 + AD$ where D is the absorbed dose and A is a constant. The x-ray absorbed dose rate was varied over a range of 0.15 Gy/s to 2.5 Gy/s, and the peak x-ray photon energy was varied over a range of 50 keVp to 90 keVp (mean energies from 31.9 keV to 44.7 keV). Also, this was performed on many different samples that had differing initial electron and hole lifetimes. It was found that the reduction of the charge-carrier lifetimes did not depend on the initial charge-carrier lifetimes, the x-ray intensity, nor the x-ray photon energy, but only on the total energy deposited into the sample. The A constant for holes was found to be $A_h = 0.203 \pm 0.021$ Gy^{-1} and the A constant for electrons was found to be $A_e = 0.062 \pm 0.009$ Gy^{-1}.

As there was no observed change in the charge-carrier drift mobilities, and drift mobility is shallow trap controlled, there is no change in the concentration of shallow electron or hole traps due to x-ray radiation. However there is a large change in the charge-carrier lifetimes,

which are dependent on the concentration of deep traps, showing a large change in the concentration of deep traps due to x-ray exposure. This change in the charge-carrier lifetimes could be due to the addition of x-ray induced traps or due to trapped x-ray generated charge-carriers in the intrinsic traps. However x-ray photogeneration is suppressed in the zero field case and it is likely the deep trap concentration is increased by the addition of x-ray induced traps. The effect of the change in the charge-carrier lifetimes on the x-ray sensitivity was examined through the charge collection efficiency. It was found that there is a drop in the charge collection efficiency after high-dose x-ray irradiation, but the drop was lower at a higher operating field and for samples with longer initial charge-carrier lifetimes. Therefore the x-ray induced effects on detectors that use high quality electronic grade a-Se and are operated at high fields are negligible.

6.2 X-ray Induced Effects in a-Se in the Presence of an Applied Field

The second goal of this investigation was to determine the dependence of x-ray induced effects on the transport properties in a-Se on the applied electric field during exposure. The application of x-ray exposure on the sample placed under an electric field resulted in no observable change in the hole drift mobility. However there was a large reduction in the hole lifetime due to x-ray exposure for the sample under an applied field during exposure. Plotting the normalized inverted lifetime against the absorbed dose gave an empirical equation $\tau_{ho}/\tau_h = 1 + B[1-\exp(-D/C)]$ where τ_{ho} is the initial (pre-exposure) hole lifetime of the sample, τ_h is the hole lifetime after exposure, D is the absorbed dose, B is a constant, and C is a parameter that depends on the applied field during exposure empirically as $C = C_1\exp(-(F/C_2)^{\beta}) + C_3$ where F is the applied electric field during exposure, and C_1, C_2, C_3, and β are constants. The constants were found experimentally to be; $B \approx 4.21$, $C_1 \approx 19.9$ Gy, $C_2 \approx 4.44$ V/μm, $C_3 \approx 0.06$ Gy, and $\beta \approx 2.49$. The absorbed dose rate was varied over a range of 0.12 Gy/s to 2.5 Gy/s, and the peak x-ray photon energy was varied over a range of 50 keVp to 90 keVp (mean energies from 31.9 keV to 44.7 keV). Also the applied electric field was varied from 0 V/μm to 10 V/μm. It was found that the reduction in the hole lifetime was independent of the dose rate and photon energy. However, there was a large dependence on the applied field during exposure. Put differently, the reduction in the hole lifetime due to x-ray exposure does not depend on the x-ray intensity or x-ray photon energy, but only on the energy deposited in the sample and the applied field over the sample.

As there was no observed change in the hole drift mobility, and drift mobility is shallow trap controlled, there is no change in the concentration of shallow hole traps due to x-ray radiation in the presence of an applied field. However there is a large change in the hole lifetime, which is dependent on the concentration of deep traps, showing a large change in the concentration of deep traps due to x-ray exposure in the presence of an applied field. Further, when the sample was placed under a larger electric field during exposure, the reduction in the hole lifetime increased. This change in the hole lifetime could be due to the addition of x-ray induced traps or due to trapped x-ray generated charge-carriers in the intrinsic traps. The larger reduction in the hole lifetime under applied field can be understood by the electron-hole pair creation energy. At a zero applied electric field x-ray photogeneration is suppressed, it is likely the deep trap concentration is mostly changed by the addition of x-ray induced traps. At larger fields however, the electron-hole pair creation energy gets lower and the x-ray photogeneration increases. Thus the larger reduction in the hole lifetime in the presence of a large applied field is likely mostly due to trapped electrons in the intrinsic deep traps. The effect of the change in the charge-carrier lifetimes on the x-ray sensitivity was examined through the hole charge collection efficiency. It was found that there is a considerable drop in the charge collection efficiency after high-dose x-ray irradiation, but the drop was lower at a higher operating field and for samples with longer initial charge-carrier lifetimes. Therefore the x-ray induced effects are minimized if detectors that use high quality electronic grade a-Se are used and are operated at high fields.

6.3 Suggestions for Future Work

Before this investigation, there has been a large amount of research performed on the electrical properties of a-Se. However there has not been extensive research into the effect the applied electric field has on the x-ray induced changes in charge-carrier transport properties. In this work the x-ray induced changes in the hole transport properties were investigated in the absence and in the presence of an applied field. The case in which the sample is under an applied field during x-ray exposure could be expanded by including more variation in the electric field strength. With more data the empirical equations derived could be made more accurate. Also an investigation into the x-ray induced effects on the electron transport properties in the presence of an applied field would be of interest. This work could also be expanded to include the effect the presence of an applied field has on the recovery of the carrier lifetimes.

References

[1] M. Körner, C. H. Weber, S. Wirth, K. J. Pfeifer, M. F. Reiser, and M. Treitl "Advances in digital radiography: Physical principles and system overview," *Radiographics*, Vol. 27, no. 3, pp 675-686, May 2007. https://doi.org/10.1148/rg.273065075

[2] M. Kallergi, "Computer-aided diagnosis of mammographic microcalcification clusters," *Medical physics*, Vol. 31, pp 314-326, Jan. 2004. https://doi.org/10.1118/1.1637972

[3] S. O. Kasap, J. B. Frey, G. Belev, O. Tousignant, H. Mani, J. Greenspan, L. Laperriere, O. Bubon, A. Reznik, G. DeCrescenzo, K. S. Karim, and J. A. Rowlands, "Amorphous and Polycrystalline Photoconductors for Direct Conversion Flat Panel X-Ray Image Sensors," *Sensors*, Vol. 11, pp 5112-5157, May 2011. Doi: 10.3390/s110505112

[4] S. O. Kasap, and J. A. Rowlands, "Review: X-ray photoconductors and stabilized a-Se for direct conversion digital flat-panel X-ray image-detectors," *Journal of Materials Science: Materials in Electronics*, Vol. 11, pp 179-198, 2000.

[5] J.M. Boone, "Chapter 1: X-ray production, interaction, and detection in diagnostic imaging," in *Handbook of Medical Imaging: Volume 1. Physics and Psychophysics*, J. Beutell, H. L. Kundel, and R. L. VanMetter, Eds, SPIE Press, Bellington, 2000, pp. 1-78.

[6] S. O. Kasap, and J. A. Rowlands, "Direct-conversion flat-panel x-ray image sensors for digital radiography," *Proceedings of the IEEE*, Vol. 90, no. 4, pp 591-604, April 2002.

[7] J. A. Rowlands, and J. Yorkston, "Chapter 4: Flat panel detectors for digital radiography," in *Handbook of Medical Imaging: Volume 1. Physics and Psychophysics*, J. Beutell, H. L. Kundel, and R. L. VanMetter, Eds, SPIE Press, Bellington, 2000, pp. 225-313.

[8] S. O. Kasap, "X-ray sensitivity of photoconductors: application to stabilized a-Se," *Journal of Physics D: Applied Physics*, vol. 33, pp. 2853-2865, May 2000, https://doi.org/10.1088/0022-3727/33/21/326

[9] M. J. Yaffe, "Basic physics of digital mammography," in *Digital Mammography: Medical Radiology*, U. Bick, F. Diekmann. Eds, Springer, Berlin, Heidelberg, 2010

[10] C. C. Scott, A. Parsafar, A. El-Falou, P. M. Levine, and K. S. Karim, “High Dose Efficiency, Ultra-high Resolution Amorphous Selenium/CMOS Hybrid Digital X-ray Imager,” *2015 IEEE International Electron Devices Meeting (IEDM)*, Washington, DC, pp. 30.6.1-30.6.4, 2015.

[11] A. Camlica, A. El-Falou, R. Mohammadi, P. M. Levine and K. S. Karim, "CMOS-Integrated Single-Photon-Counting X-Ray Detector using an Amorphous-Selenium Photoconductor with 11 × 11-μm^2 Pixels," *2018 IEEE International Electron Devices Meeting (IEDM)*, San Francisco, CA, pp. 32.5.1-32.5.4, 2018.

[12] A. Parsafar, C. C. Scott, A. El-Falou, P. M. Levine and K. S. Karim, "Direct-Conversion CMOS X-Ray Imager With 5.6 μm × 6.25 μm Pixels," in *IEEE Electron Device Letters*, vol. 36, no. 5, pp. 481-483, May 2015.

[13]

[13] S. O. Kasap, J. B. Frey, G. Belev, O. Tousignant, H. Mani, L. Laperriere, A. Reznik, J. A. Rowlands, “Amorphous selenium and its alloys from early xeroradiography to high resolution X-ray image detectors and ultrasensitive imaging tubes,” *Physica Status Solidi B*, Vol. 246, pp. 1794-1805, July 2009. https://doi.org/10.1002/pssb.200982007

[14] W. Que, and J. A. Rowlands, “X-ray photogeneration in amorphous selenium: Geminate versus columnar recombination,” *Physical Review B*, Vol. 51, no. 16, pp. 10500-10507, April 1995. https://doi-org.cyber.usask.ca/10.1103/PhysRevB.51.10500

[15] F. Manouchehri, M. Z. Kabir, O. Tousignant, H. Mani, and V. K. Devabhaktuni, “Time and exposure dependent x-ray sensitivity in multilayer amorphous selenium detectors,” *Journal of Physics D: Applied Physics*, Vol. 41, no. 23, 235106, Nov. 2008. https://doi.org/10.1088/0022-3727/41/23/235106

[16] S. A. Mahmood, M. Z. Kabir, O. Tousignant and J. Greenspan, "Investigation of Ghosting Recovery Mechanisms in Selenium X-ray Detector Structures for Mammography," *IEEE Transactions on Nuclear Science*, vol. 59, no. 3, pp. 597-604, June 2012. Doi: 10.1109/TNS.2012.2193899

[17] M. Z. Kabir and S. O. Kasap, "Charge collection and absorption limited sensitivity of x-ray photoconductors: Applications to a-Se and HgI_2," *Applied Physics Letters*, Vol. 80, no. 9, pp. 1664-1666 , Feb. 2002. https://doi.org/10.1063/1.1454213

[18] K. Hecht, "For the mechanism of the photoelectric primary current in insulating crystals," *Zeitschrift für Physik*, Vol. 77, pp. 235-245, 1932. https://doi.org/10.1007/BF01338917

[19] B. Fogal, "Electronic Transport Properties of Stabilized Amorphous Selenium X-ray Photoconductors," M.Sc. Thesis, Dept. Elect. Eng., University of Saskatchewan, Saskatoon, Canada, 2005.

[20] M. Walornyj, "Electron Lifetime and its Dependence on Temperature and Dose in a-Se Photoconductors," M. Sc. Thesis, Dept. Elect. Comp. Eng., University of Saskatchewan, Saskatoon, Canada, 2013.

[21] J. Yang, "X-ray Induced Changes in Electronic Properties of Stabilized Amorphous Selenium Based Photoconductors," M. Sc. Thesis, Div. Biomed. Eng., University of Saskatchewan, Saskatoon, Canada, 2016.

[22] W. E. Spear, "Drift mobility techniques for the study of electrical transport properties in insulating solids", *Journal of Non-Crystalline Solids*, Vol. 1, pp. 197-214, April 1969. https://doi.org/10.1016/0022-3093(69)90001-5

[23] B. Polischuk, "Interrupted Field Time-of-Flight Transient Photoconductivity Technique and its Applications to Amorphous Semiconductors," Ph. D. Thesis, University of Saskatchewan, Saskatoon, Canada, 1994.

[24] A. C. Papadakis, "Theory of transient space-charge perturbed currents in insulators", *Journal of Physics and Chemistry of Solids*, Vol. 28, pp. 641-647, April 1967. https://doi.org/10.1016/0022-3697(67)90095-9

[25] S. O. Kasap, *Optoelectronics and Photonics: Principles and Practices*, Prentice Hall, Upper Saddle River, New Jersey, 2001.

[26] K. R. Zanio, W. M. Akutagawa, and R. Kikuchi, "Transient currents in semi-insulating CdTe characteristic of deep traps", *Journal of Applied Physics*, Vol. 39, no. 6, pp. 2818-2828, Jan. 1968. https://doi-org.cyber.usask.ca/10.1063/1.1656679

[27] W. Akutagawa and K. Zanio, "The Possibilities of Using CdTe as a Gamma Spectrometer," in *IEEE Transactions on Nuclear Science*, vol. 15, no. 3, pp. 266-274, June 1968. **DOI:** 10.1109/TNS.1968.4324947

[28] M. T. A. Nesdoly, "X-ray Sensitivity and X-ray Induced Charge Transport Changes in Stabilized a-Se Films," Ph. D. Thesis, University of Saskatchewan, Saskatoon, Canada, 2000.

[29] M. Martini, J. W. Mayer, and K. R. Zanio, "Drift velocity and trapping in semiconductors – transient charge technique", *Applied Solid State Science*, Vol. 3, pp 181-261, 1972. https://doi.org/10.1016/B978-0-12-002903-7.50010-2

[30] R.M. Blakney and H. P. Grunwald, "Small-signal current transients in insulators with traps", *Physical Review*, Vol. 159, pp. 658-664, July 1967. https://doi.org/10.1103/PhysRev.159.658

[31] R. M. Blakney and H. P. Grunwald, "Trapping processes in amorphous selenium", *Physical Review*, Vol. 159, pp. 664-671, July 1967. https://doi.org/10.1103/PhysRev.159.664

[32] S. O. Kasap, R. P. S. Thakur, and D. Dodds, "Method and apparatus for interrupted transit time transient photoconductivity measurements", *Journal of Physics E: Scientific Instrumentation*, Vol. 21, no. 12, pp. 1195-1202, Dec. 1988. https://doi.org/10.1088/0022-3735/21/12/017

[33] F. W. Schmidlin, "Theory of trap-controlled transient photoconduction," *Physical Review B*, Vol. 16, pp. 2362-2385, Sept. 1977. https://doi-org.cyber.usask.ca/10.1103/PhysRevB.16.2362

[34] J. Noolandi, "Multiple-trapping model of anomalous transit-time dispersion in a-Se," *Physical Review B*, Vol. 16, pp. 4466-4473, Nov. 1977. https://doi.org/10.1103/PhysRevB.16.4466

[35] F. W. Schmidlin, "Theory of multiple trapping," *Solid State Communications*, Vol. 22, pp. 451-453, May 1977. https://doi.org/10.1016/0038-1098(77)90123-5

[36] A. I. Rudenko, “Theory of trap-controlled transient current injection,” *Journal of Non-Crystalline Solids*, Vol. 22, no. 1, pp. 215-218, 1976.

[37] B. Polischuk, S. O. Kasap, and A. Baillie, “Study of photogenerated charge carrier dispersion in chlorinated a-Se: 0.3% As by the interrupted field time-of-flight technique,” *Applied Physics Letters*, Vol. 63, pp 183-185, April 1993. https://doi.org/10.1063/1.110393

[38] C. S. Allen, “Relaxation in the Electrical Properties of Amorphous Selenium Base Photoconductors,” M. Sc. Thesis, Dept. Elect. Eng., University of Saskatchewan, Saskatoon, Canada, 2009.

[39] J. Hirsh, H. Jahankhani, “The carrier yield in a-Se under electron bombardment”, *Journal of Physics: Condensed Matter*, Vol. 1, no. 45, pp. 8789-8798, 1989. https://doi.org/10.1088/0953-8984/1/45/004

[40] W. E. Spear, “Transit time measurements of charge carriers in amorphous selenium films,” *Proceedings from the Physical Society of London, Section B*, Vol. 70, no. 7, pp. 669-675, 1957. https://doi.org/10.1088/0370-1301/70/7/304

[41] R. G. Kepler, “Charge carrier production and mobility in anthracine crystals,” *Physical Review*, Vol. 119, pp. 1226-1229, Aug. 1960. https://doi.org/10.1103/PhysRev.119.1226

[42] Leblanc O.H., “Hole and electron drift mobilities in anthracine,” *Journal of Chemical Physics*, Vol. 35, pp. 626, April 1960. https://doi.org/10.1063/1.1731216

[43] F. C. Brown, “Temperature dependence of electron mobility in AgCl,” *Physical Review*, Vol. 97, pp. 355-362, Jan. 1955.

[44] S. O. Kasap, and C. Juhasz, “Transient photoconductivity probing of negative bulk space charge evolution in halogenated amorphous selenium films,” *Solid State Communications*, Vol. 63, pp. 553-556, Aug. 1987. https://doi.org/10.1016/0038-1098(87)90290-0

[45] S. O. Kasap, B. Polischuk, and D Dodds, “An interrupted field time-of-flight (IFTOF) technique in transient photoconductivity measurements,” *Review of Scientific Instruments*, Vol. 61, pp. 2080-2087, Feb 1990. https://doi.org/10.1063/1.1141421

[46] W. Hefrich, and P. Mark, “Space charge limited currents in anthracine as a means of determining the hole drift mobility,” *Zeitschrift Fur Physik*, Vol. 166, pp 370-385, 1962.

[47] B. Polischuk, and S. O. Kasap, “A high-voltage interrupted-field time-of-flight transient photoconductivity apparatus,” *Measurement Science & Technology*, Vol. 2, no. 1, pp. 75-80, 1991. https://doi.org/10.1088/0957-0233/2/1/012

[48] Gendex Corp, *GX-1000 intra oral x-ray system installation/maintenance manual.* Gendex Corp, Milwaukee, WI, USA

[49] J. Punnoose, J. Xu, A. Sisniega, W. Zbijewski, and J. H. Siewerdsen, “Technical Note: SPEKTR 3.0—A computational tool for x-ray spectrum modeling and analysis,” *Med. Phys.*, Vol. 43, pp. 4711-4717, 2016. Doi:10.1118/1.4955438

[50] M. J. Yaffe, (2010) “Detectors for Digital Mammography,” in *Digital Mammography. Medical Radiology*, U. Bick, F. Diekman, Eds, Springer, Berlin, Heidelberg, 2010, pp 13-31. https://doi.org/10.1007/978-3-540-78450-0_2

[51] J. H. Hubbel, S. M. Seltzer, “Tables of x-ray mass attenuation coefficients and mass energy-absorption coefficients from 1 keV to 20 MeV for elements Z = 1 to 92 and 48 additional substances of dosimetric interest,” *National Institute of Standards and Technology*, Dec. 2019. [Online]. Available: http: //www.nist.gov/pml/data/xraycoef/

[52] Reproduced from S.O. Kasap, J. Yang, B. Simonson, E. Adeagbo, M. Walornyj, G. Belev, M.P. Bradley, and R.E. Johanson, “Effects of x-ray irradiation on charge transport and charge collection efficiency in stabilized a-Se photoconductors,” *Journal of Applied Physics*, vol. 127, 084502, Feb 2020, with the permission of AIP Publishing

[53] B. Polischuk, S. O. Kasap, V. Aiyah, and A. Baillie, “The interrupted field time-of-flight transient photoconductivity technique for studying charge transport and trapping in high resistivity semiconductors” *International Journal of* Electronics, Vol. 76, pp. 1029-1041, 1994, https://doi.org/10.1080/00207219408926014

[54] B. Polischuk, S. O. Kasap, V. Aiyah, A. Baillie, and M. A. Abkowitz, “Measurement of mobility-lifetime products in amorphous semiconductors,” *Canadian Journal of* Physics, vol. 69, pp. 361-369, 1991, https://doi.org/10.1139/p91-061

[55] M. Abkowitz and R. C. Enck, “Xerographic spectroscopy of gap states in amorphous semiconductors,” *Physical Review* B, vol. 25, pp. 2567, Aug. 1982, https://doi.org/10.1103/PhysRevB.25.2567

[56] S. O. Kasap, V. Aiyah, B. Polischuk, and M. A. Abkowitz, “Determination of the deep-hole capture cross-section in a-Se via xerographic and interrupted-field time-of-flight techniques,” *Philosophical Magazine Letters*, vol. 62, pp. 377-382, Aug. 1990, https://doi.org/10.1080/09500839008215159

[57] B. Fogal, M. Z. Kabir, K. O’Leary, R. E. Johanson, and S. O. Kasap, “X-ray-induced recombination effects in a-Se-based x-ray photoconductors used in direct conversion x-ray sensors,” *Journal of Vacuum Science & Technology A*, vol. 22, pp 1005, May 2004, https://doi.org/10.1116/1.1701856

[58] X. Zhang and D. A. Drabold, “Direct molecular dynamic simulation of light-induced structural change in amorphous selenium,” *Physical Review Letters*, vol. 83, 5042, June 1999. https://doi.org/10.1103/PhysRevLett.83.5042

[59] J. Berashevich, A. Mishchenko, and A. Reznik, “Two-step photoexcitation mechanism in amorphous Se,” *Physical Review Applied*, vol. 1, 034008, April 2014, https://doi.org/10.1103/PhysRevApplied.1.034008

[60] D. Hohl and R. O. Jones, “First-principles molecular-dynamics simulation of liquid and amorphous selenium,” *Physical Review B*, vol. 43, 3856, Feb. 1991. https://doi.org/10.1103/PhysRevB.43.3856

[61] W. Zhao, G. DeCrescenzo, S. O. Kasap, and J. A. Rowlands, “Ghosting caused by bulk charge trapping in direct conversion flat-panel detectors using amorphous selenium,” *Medical Physics*, vol. 32, pp. 488-500, Jan 2005, https://doi.org/10.1118/1.1843353

[62] B. Fogal, R. E. Johanson, G. Belev, S. O’Leary, and S. O. Kasap, ‘X-ray induced effects in stabilized a-Se x-ray photoconductors,” *Journal of Non-Crystalline Solids*, vol. 299-302, pp. 993-997, April 2002. https://doi.org/10.1016/S0022-3093(01)01065-1

[63] G. Belev and S. O. Kasap, “Amorphous selenium as an x-ray photoconductor,” *Journal of Non-Crystalline Solids*, vol. 345-346, pp. 484-488, Oct. 2004. https://doi.org/10.1016/j.jnoncrysol.2004.08.070

[64] K. Ramaswami, R. Johanson, and S. Kasap, “Charge collection efficiency in photoconductive detectors under small to large signals,” *Journal of Applied Physics,* vol. 125, 244503 June 2019, https://doi.org/10.1063/1.5096900

[65] C. Haugen, S. O. Kasap, J. Rowlands, “Charge transport and electron-hole-pair creation energy in stabilized a-Se x-ray photoconductors,” *Journal of Physics D: Applied Physics*, vol. 32, no. 3, pp. 200-207, Oct. 1998. Doi: 10.1088/0022-3727/32/3/004

Appendix: Dose Calculation

The following custom excel sheet was created and used in order to calculate the absorbed dose in a sample. The excel sheet follows the procedure described in Section 3.5.1. The top section is uses the simulated x-ray fluence spectrum obtained on SPEKTR 3.1 [49] in order to calculate the theoretical dose deposited into the ion chamber. From here, the user inserts the actual dose measured with the ion chamber. The bottom half then uses the dose measured and the theoretical dose deposited into the chamber to find the scaling factor *K*. Scaling the simulated x-ray spectrum gives the actual x-ray spectrum at the surface of the a-Se sample. The bottom half of the excel sheet uses the actual x-ray fluence spectrum to calculate the absorbed dose at a specified region in the a-Se sample. To use the excel sheet, the user must insert the simulated x-ray fluence spectrum corresponding to the peak x-ray photon energy used into the area indicated with a yellow shade. Then the user must insert the actual dose measured by the ion chamber in the area indicated with a blue shade. Finally the user must indicate the depth into the a-Se sample of interest using the brown shaded area. The excel sheet will then automatically give the absorbed dose in the green shaded area.

	ρ(air)
g/cm^3	0.001205
kg/cm^3	0.000001205

A (cm^2)	D (cm)
12.3163	1.22

Energy (keV)	*mass attenuation coefficient* μ/ρ *air* (cm^2/g)	*Mass energy absorption coefficient* μ_{en}/ρ *air* (cm^2/g)
10	5.12	4.742
11	3.9031324	3.519178428
12	3.04664388	2.680641078
13	2.425755495	2.086905578
14	1.964313464	1.655118566
15	1.614	1.334
16	1.370156342	1.088618121
17	1.174819036	0.899333916
18	1.016227775	0.751119967
19	0.885966238	0.633471992
20	0.7779	0.5389
21	0.707575995	0.463454715
22	0.646421647	0.401326676
23	0.592930846	0.349758178
24	0.545869637	0.306605698

photon energy (keV)	$\Phi_{ideal}(E)$ (photons /(mm^2 keV))	$\Phi_{ideal}(E)$ (photons / (cm^2 keV))	
10	9.77E-07	9.7729E-05	1.44741E-18
11	2.58E-04	0.02576765	6.68607E-17
12	1.41E-02	1.407166	1.14755E-15
13	2.76E-01	27.58615	1.0264E-14
14	2.74E+00	273.9576	5.48273E-14
15	1.58E+01	1576.696	1.9843E-13
16	6.06E+01	6061.82	5.36227E-13
17	1.73E+02	17329.6	1.15888E-12
18	3.96E+02	39625.02	2.10619E-12
19	7.64E+02	76380.57	3.34275E-12
20	1.29E+03	128949.8	4.78343E-12
21	1.97E+03	196691.7	6.30464E-12
22	2.76E+03	276400.1	7.74374E-12
23	3.62E+03	361503.7	9.07035E-12
24	4.56E+03	456127.1	1.02471E-11

25	0.504243341	0.270226176	25	5.51E+03	550743.1	1.11584E-11
26	0.467242877	0.23934605	26	6.40E+03	640460.4	1.17776E-11
27	0.434204652	0.212967982	27	7.21E+03	721383.5	1.2141E-11
28	0.404580206	0.190303534	28	7.95E+03	795033.9	1.23079E-11
29	0.377913018	0.170723929	29	8.61E+03	861072.2	1.22535E-11
30	0.3538	0.1537	30	9.11E+03	910557.1	1.2064E-11
31	0.339781196	0.140125487	31	9.51E+03	951264.5	1.18105E-11
32	0.326787886	0.12813363	32	9.81E+03	981254.1	1.1422E-11
33	0.314668788	0.11749106	33	9.97E+03	996566.1	1.09102E-11
34	0.303341185	0.108011703	34	9.99E+03	999322.6	1.04049E-11
35	0.292732318	0.099539604	35	1.01E+04	1008901	9.92779E-12
36	0.282777946	0.091943374	36	1.01E+04	1009201	9.40086E-12
37	0.273421146	0.085111768	37	1.00E+04	1000591	8.84938E-12
38	0.26461131	0.078950167	38	9.86E+03	986489.1	8.28912E-12
39	0.256303297	0.073377734	39	9.66E+03	965882.8	7.73352E-12
40	0.2485	0.06833	40	9.42E+03	942446.4	7.23476E-12
41	0.243626193	0.064569639	41	9.14E+03	913999.2	6.78179E-12
42	0.238990088	0.06110123	42	8.82E+03	881871.2	6.34417E-12
43	0.234548224	0.057894299	43	8.51E+03	850586	5.91277E-12
44	0.230288223	0.054923721	44	8.13E+03	813197.7	5.50034E-12
45	0.226198755	0.052167283	45	7.81E+03	780695.3	5.10699E-12
46	0.222269427	0.049605289	46	7.42E+03	742205.1	4.72599E-12
47	0.218490685	0.047220232	47	7.07E+03	707244.4	4.39288E-12
48	0.214853736	0.044996507	48	6.78E+03	677634.7	4.07648E-12
49	0.211350468	0.042920174	49	6.42E+03	642459.1	3.73538E-12
50	0.208	0.04098	50	5.99E+03	599340.5	3.41991E-12
51	0.205670088	0.039671825	51	5.60E+03	560143.5	3.16083E-12
52	0.203409775	0.03843119	52	5.25E+03	524994.7	2.90908E-12
53	0.201216655	0.037251891	53	4.86E+03	485975.9	2.68079E-12
54	0.199087518	0.036129823	54	4.57E+03	456957.9	2.47457E-12
55	0.197019365	0.035061224	55	4.24E+03	423721.4	2.26294E-12
56	0.195009386	0.034042641	56	3.91E+03	391004.7	2.06492E-12
57	0.19305495	0.033070904	57	3.61E+03	360924.3	1.89564E-12
58	0.191153586	0.032143089	58	3.37E+03	337137.1	1.74162E-12
59	0.189302976	0.031256507	59	3.11E+03	311261	1.54422E-12
60	0.1875	0.03041	60	2.70E+03	269771.3	1.3483E-12
61	0.186172563	0.030005589	61	2.40E+03	239699.8	1.21817E-12
62	0.18490785	0.029611675	62	2.19E+03	219165.3	1.10268E-12
63	0.18367176	0.029229113	63	1.95E+03	194953.3	9.7076E-13
64	0.182463206	0.028857403	64	1.69E+03	168545	8.39894E-13
65	0.181281158	0.028496073	65	1.45E+03	145032.1	7.06641E-13
66	0.180124641	0.028144682	66	1.18E+03	118045.2	6.02094E-13
67	0.178992728	0.027802811	67	1.05E+03	105459.3	5.24666E-13
68	0.177884542	0.027470067	68	8.88E+02	88766.9	4.16802E-13
69	0.176799245	0.027146075	69	6.51E+02	65118.81	3.12742E-13
70	0.175736045	0.026830485	70	5.00E+02	50030.32	2.31128E-13

71	0.174694184	0.026522963	71	3.48E+02	34846.83	1.63928E-13
72	0.173672943	0.026223194	72	2.52E+02	25192.17	1.09377E-13
73	0.172671635	0.025930878	73	1.48E+02	14768.5	5.18325E-14
74	0.171689608	0.025645731	74	4.13E+01	4126.989	1.13434E-14
75	0.170726235	0.025367485	75	0	0	0
76	0.169780922	0.025095884	76	0	0	0
77	0.168853098	0.024830685	77	0	0	0
78	0.167942219	0.024571656	78	0	0	0
79	0.167047765	0.024318578	79	0	0	0
80	0.1662	0.02407	80	0	0	0
81	0.165457691	0.024023689	81	0	0	0
82	0.164771294	0.023977945	82	0	0	0
83	0.164096012	0.023932841	83	0	0	0
84	0.163431536	0.023888361	84	0	0	0
85	0.162777567	0.023844489	85	0	0	0
86	0.162133818	0.023801208	86	0	0	0
87	0.161500013	0.023758505	87	0	0	0
88	0.160875887	0.023716366	88	0	0	0
89	0.160261185	0.023674776	89	0	0	0
90	0.159655661	0.023633723	90	0	0	0

$E_{deposited\ (Ion\ Chamber)}$ (J)	2.92585E-10
$D_{deposited\ (Ion\ Chamber)}$ (Gy)	1.61594E-05
$D_{measured}$ (Gy)	0.004725276
K	292.4165031

	ρ(Se)
g/cm^3	4.28
kg/cm^3	0.00428

A_{Se} (cm^2)	x2 (μm)	x1 (μm)
1	31.5	30.5

K	292.416503

Energy (keV)	*mass attenuation coefficient* (μ/ρ) *Se* (cm^2/g)	*Mass energy absorption coefficient* (μ_{en}/ρ) *Se* (cm^2/g)	photon energy (keV)	$\Phi_{ideal}(E)$ (photons /(mm^2 keV))	$\Phi_{measured}(E)$ (photons / (cm^2 keV))	
12.658	162.0582272	100.6564639	12	1.41E-02	411.478561	4.76418E-14
13	150.7771892	93.99329322	13	2.76E-01	8066.64552	6.26231E-13
14	123.3907237	77.70745607	14	2.74E+00	80109.7234	4.54312E-12
15	102.385389	65.09267443	15	1.58E+01	461051.931	2.10778E-11
16	85.98563308	55.15290186	16	6.06E+01	1772576.21	6.99872E-11
17	72.98126381	47.20291482	17	1.73E+02	5067461.03	1.7985E-10
18	62.52713799	40.76000854	18	3.96E+02	11587009.8	3.78718E-10

19	54.0202864	35.47697261	19	7.64E+02	22334939.2	6.82061E-10
20	47.02228073	31.09939277	20	1.29E+03	37707049.6	1.08713E-09
21	41.20888595	27.437743	21	1.97E+03	57515899.1	1.57218E-09
22	36.33663908	24.34872306	22	2.76E+03	80823950.7	2.09469E-09
23	32.22019551	21.72251992	23	3.62E+03	105709648	2.63752E-09
24	28.71668178	19.47395042	24	4.56E+03	133379092	3.17686E-09
25	25.71470147	17.53619842	25	5.51E+03	161046371	3.66377E-09
26	23.12648933	15.85631819	26	6.40E+03	187281191	4.07256E-09
27	20.88223183	14.39196051	27	7.21E+03	210944440	4.40042E-09
28	18.92590166	13.10895817	28	7.95E+03	232481033	4.65657E-09
29	17.21216567	11.97952404	29	8.61E+03	251791722	4.82204E-09
30	15.70406385	10.98089153	30	9.11E+03	266261923	4.90144E-09
31	14.37124895	10.0942783	31	9.51E+03	278165439	4.91853E-09
32	13.18863839	9.304088952	32	9.81E+03	286934893	4.86539E-09
33	12.13537267	8.59729606	33	9.97E+03	291412374	4.74489E-09
34	11.19400373	7.962955774	34	9.99E+03	292218420	4.6131E-09
35	10.34985763	7.391825728	35	1.01E+04	295019302	4.48045E-09
36	9.590530221	6.876061501	36	1.01E+04	295107027	4.31328E-09
37	8.905485462	6.408973806	37	1.00E+04	292589321	4.12332E-09
38	8.285733299	5.984833034	38	9.86E+03	288465693	3.91836E-09
39	7.723569754	5.598710928	39	9.66E+03	282440071	3.70543E-09
40	7.212366005	5.246351632	40	9.42E+03	275586881	3.48883E-09
41	6.746396261	4.924066064	41	9.14E+03	267268450	3.26775E-09
42	6.320696561	4.628644966	42	8.82E+03	257873693	3.05332E-09
43	5.930948372	4.35728697	43	8.51E+03	248725384	2.84153E-09
44	5.573382157	4.107538817	44	8.13E+03	237792428	2.63876E-09
45	5.244697146	3.877245441	45	7.81E+03	228288190	2.44529E-09
46	4.941994288	3.664508137	46	7.42E+03	217033020	2.25801E-09
47	4.662719996	3.467649333	47	7.07E+03	206809934	2.09399E-09
48	4.404618752	3.285182844	48	6.78E+03	198151569	1.93841E-09
49	4.165693043	3.115788627	49	6.42E+03	187865643	1.77162E-09
50	3.944169356	2.958291305	50	5.99E+03	175257053	1.60764E-09
51	3.738469225	2.811641831	51	5.60E+03	163795204	1.46281E-09
52	3.547184503	2.674901772	52	5.25E+03	153517114	1.3257E-09
53	3.369056158	2.547229806	53	4.86E+03	142107373	1.20305E-09
54	3.202956059	2.42787009	54	4.57E+03	133622031	1.09389E-09
55	3.047871267	2.316142192	55	4.24E+03	123903130	9.85518E-10
56	2.902890451	2.211432378	56	3.91E+03	114336227	8.86085E-10
57	2.767192122	2.113186031	57	3.61E+03	105540222	8.01619E-10
58	2.640034397	2.020901051	58	3.37E+03	98584451.9	7.25966E-10
59	2.520746084	1.934122082	59	3.11E+03	91017853.2	6.34699E-10
60	2.408718899	1.852435468	60	2.70E+03	78885580.2	5.42868E-10
61	2.303400647	1.775464822	61	2.40E+03	70092177.3	4.77098E-10
62	2.204289239	1.702867122	62	2.19E+03	64087550.6	4.20424E-10
63	2.110927434	1.634329284	63	1.95E+03	57007562.3	3.60453E-10
64	2.022898203	1.569565124	64	1.69E+03	49285339.5	3.03775E-10
65	1.939820637	1.508312673	65	1.45E+03	42409779.5	2.49123E-10

66	1.861346322	1.450331797	66	1.18E+03	34518364.6	2.06779E-10
67	1.787156133	1.395402084	67	1.05E+03	30838039.7	1.75761E-10
68	1.716957381	1.343320956	68	8.88E+02	25956906.5	1.36305E-10
69	1.650481275	1.293901996	69	6.51E+02	19041814.7	9.97616E-11
70	1.587480662	1.246973446	70	5.00E+02	14629691.2	7.20005E-11
71	1.527728008	1.202376869	71	3.48E+02	10189788.2	4.9846E-11
72	1.471013593	1.159965944	72	2.52E+02	7366606.26	3.25189E-11
73	1.417143895	1.119605388	73	1.48E+02	4318553.13	1.51068E-11
74	1.365940137	1.081169991	74	4.13E+01	1206799.69	3.24656E-12
75	1.317236988	1.044543737	75	0	0	0
76	1.270881383	1.009619023	76	0	0	0
77	1.226731476	0.976295947	77	0	0	0
78	1.18465568	0.944481663	78	0	0	0
79	1.144531805	0.914089807	79	0	0	0
80	1.106246285	0.885039964	80	0	0	0
81	1.069693466	0.857257192	81	0	0	0
82	1.034774968	0.83067159	82	0	0	0
83	1.001399103	0.805217901	83	0	0	0
84	0.969480346	0.780835152	84	0	0	0
85	0.938938856	0.757466327	85	0	0	0
86	0.909700035	0.735058069	86	0	0	0
87	0.881694127	0.713560403	87	0	0	0
88	0.854855855	0.692926487	88	0	0	0
89	0.829124087	0.673112384	89	0	0	0
90	0.804441529	0.654076853	90	0	0	0

$E_{deposited\ (Se\ Sample)}$ (J)	1.17774E-07
$D_{deposited\ (Se\ Sample)}$ (Gy)	0.275173866